ACCELERATED MOLECULAR DYNAMICS SIMULATIONS OF ATOMIC FORCE MICROSCOPE EXPERIMENTS

by

Woo Kyun Kim

A dissertation submitted in partial fulfillment
of the requirements for the degree of
Doctor of Philosophy
(Mechanical Engineering)
in The University of Michigan
2009

Doctoral Committee:

Associate Professor Michael L. Falk, Co-Chair
Associate Professor Krishnakumar R. Garikipati, Co-Chair
Professor John Kieffer
Associate Professor Katsuo Kurabayashi

ACKNOWLEDGEMENTS

This research project would not have been possible without the support of many people. First, I would like to thank my advisor, Prof. Dr. Falk. His thoughtful advice, insightful guidance, and patient encouragement aided the writing of this dissertation in innumerable ways. My deep appreciation is extended to my committee members, Prof. Dr. Garikipati, Prof. Dr. Kieffer, and Prof. Dr. Kurabayashi for their valuable suggestions.

It has truly been my pleasure working with everyone in our group. Dr. Shi gave me valuable advice about the research, and Brian has showed warmest hospitality to me and my wife Hyun Ji who just started new lives in this country. We miss the days with him in Ann Arbor. I am also deeply indebted to new members in Baltimore, Pavan, Rongguang, Shou, and Tonghu. I would also like to thank my Korean friends in Ann Arbor, Heesuk, Daekyun, Sunmin, Taesung, Hongsuk, Naesung, and Kwangjae. Without their friendship this study would not have been possible.

Finally, I wish to express my love and gratitude to my parents, and my brother and sisters. A special thank goes to my beloved wife and life partner, Hyun Ji Kim, for her endless love and understanding throughout my entire life since day I met her. Without her, my life would be much different.

TABLE OF CONTENTS

LIST OF FIGURES

ABSTRACT

We apply an accelerated molecular dynamics (MD) methodology to simulate Atomic Force Microscope (AFM) experiments. New methods using hyperdynamics and a parallel algorithm make it possible to extend the simulation time scale and to model an AFM tip with a sliding velocity close to the actual experimental values. MD simulations of AFM models with simple geometry validate these methodologies. We model AFM experiments by which researchers observed ultralow friction forces between incommensurate surfaces, a phenomena called superlubricity. The simulation results reveal that superlubricity breaks down with softer tips and at higher normal loads, and that several metastable states exist during the stick phase with softer tips. Additional simulations with a silicon tip and a silicon surface with oxidized layers model recent AFM experiments regarding variations in the relationship between friction force and sliding velocity with respect to changes in temperature. The simulations utilize a modified Stillinger-Weber potential, which can treat both pure silicon and silica simultaneously, and the bond-boost method for hyperdynamics simulation. We compare the simulation results with the experimental data to elucidate the atomic level processes that occur during sliding. The simulation results indicate that the deviation from the Tomlinson model predictions at higher temperatures and lower sliding velocities may arise from the bond breaking and formation mechanism at the interface.

CHAPTER I

Introduction

1.1 Nanotribology

Friction has presented a significant challenge since man's earliest technological feats. As shown in Fig. 1.1, thousands years ago the ancient Egyptians made use of lubricant to reduce friction enabling the transport of heavy artifacts [1]. However, in spite of its long history, friction remains poorly understood. Although familiar macroscopic friction laws, such as Coulomb's observation that the frictional force is linearly proportional to the applied force normal to the contact surface and independent of both the apparent contact area and the sliding velocity, hold in many instances, there is no fundamental understanding of the origin of these laws and many exceptions exist. Moreover, estimates indicate that addressing wear and friction issues can save 1.3% to 1.6% of GNP in the U.K. alone [2]. Furthermore, it is conjectured that the first 20% of the economic savings can be obtained without making any significant investment.

In recent years, friction on a micro or nano scale has been a growing concern as nanotechnology, particularly micro/nano electro-mechanical systems (MEMS/NEMS), advances. In MEMS/NEMS development, preventing wear and adhesion is one of the most critical issues affecting the performance and fabrication of MEMS/NEMS devices due to their large surface-to-volume ratios. The problems arising from adhesion and wear have prevented MEMS/NEMS devices with sliding interfaces in rotary and linear motion from being marketed [3]. For this reason and others, significant effort has been focused on understanding the origins of adhesion, friction, and wear on a micro/nano scale. This research is commonly termed nanotribology.

At present, nanotribology is intensively studied by experimental tools newly invented in the 1970's and 1980's. These devices include the Surface Forces Apparatus (SFA) [4] and the Atomic Force Microscope (AFM) [5]. Moreover, the Quartz-Crystal Microbalance (QCM), originally used to measure the mass of adsorbed films, has a new application measuring the viscosity of the film-substrate interface [6]. Unlike its precursor, the Scanning Tunneling Microscope (STM), AFM can be used with both conductors and insulators and in less ideal environments like ambient air. This has greatly broadened the range of applications. Moreover, AFM has provided an opportunity to investigate friction with a single-asperity contact and the measurement of atomic scale forces. The radii of typical AFM tips range from 10 nm to 100 nm [7]. Due to these advantages, AFM is most widely used in the study of nanotribology. AFM experimental results will be presented in the next section.

To explain the experimental results and understand the physical origin of atomic scale friction, several theories have been proposed [8-11] based on the Tomlinson model [12], and have succeeded in explaining some fundamental aspects of atomic scale friction such as the stick-slip behavior and the logarithmic dependence of the frictional force on the sliding velocity [8]. However, these theories are too simple to explain more complicated triobological behaviors such atomic mixing, and bond breaking and formation during atomic scale sliding. Less reductive theories are needed to elucidate the experiments that give limited insight into the detailed atomic process in the absence of theoretical interpretation.

In this sense, computer simulation can play an important role in the research of triobological properties of nano scale materials, bridging the gap between the simplistic Tomlinson model and real experiments. Computer simulations can yield a solution to a problem in statistical mechanics which is intractable with analytical methods, and the simulation results can be compared with experimental results. If the mathematical model solved using computers can capture important physical features of a real process, then the results of the simulation will show substantial agreement with experimental observations and provide meaningful insight [13]. Moreover, in a computer simulation of a working model, we can directly observe what is taking place on an atomic scale, which is currently impossible in real experiments.

The methodologies of atomic scale computer simulations used in materials science primarily derive from the molecular dynamics (MD) method and the Monte Carlo (MC) method. MC samples the points in the phase space according to the ensemble distribution of a given system and is, therefore, applicable to equilibrium systems only, but MD calculates trajectories of the atoms using classical mechanics and can simulate both equilibrium systems and non-equilibrium systems. Recently, another dynamics method called Kinetic Monte Carlo (KMC) has been used for the transient systems. The differences between MD and KMC will be discussed in detail in the next chapter.

In this study, molecular dynamics has been used. We model AFM experiments and attempt to directly observe and explain the fundamental processes of atomic scale friction. MD simulation has been widely used for the investigation of nano scale physics, and has been applied to the study of friction in various cases, which will be reviewed in Sec. 1.3. It has not been possible, however, to directly compare simulation results with experimental data because of the limited time scales accessible using standard MD techniques, sub-micro seconds. Thus, the sliding speed required to scan a reasonable length scale (> 10 nm) must be larger in MD simulations than in the actual experiments by several orders of magnitude. In specific cases several methodologies that circumvent direct dynamics of particles have been proposed to address the time-scale problems [14, 15]. Performing direct simulation on longer time scales has been a long-term goal of MD simulators.

A majority of the research presented here focuses on extending the simulation time scale in order to model an AFM tip with a sliding velocity close to the actual experimental values. The methodologies used for this goal will be presented in the subsequent chapters. The next section reviews some interesting AFM experiments motivating this study. Sec. 1.3 will describe the MD method, several simulation results, and the time-scale problem.

1.2 AFM experiment

AFM was first invented by Binnig, Quate, and Gerber in 1986 [5] to image the morphology of a surface. Nowadays, it has become a major tool in the investigation of nanotribology and is widely used to measure the frictional force acting on a sharp tip scanning a flat sample surface. For this application, AFM is also called the Lateral Force Microscope (LFM) or the Friction Force Microscope (FFM).

As shown in Fig. 1.2, an AFM consists of a tip and a cantilever. The tip is attached to the end of the cantilever and scans a sample surface while the other end of the cantilever moves at a constant speed. As the tip scans a surface, it experiences a frictional force, and due to this force, the cantilever deforms by bending and twisting. This curves the path of a laser beam reflected by the cantilever to be modified and, in turn, creates a voltage difference in a photo detector receiving the laser beam. Finally, through proper calibration the quantitative value of friction can be obtained.

A typical AFM tip is sharp enough to guarantee a single asperity contact with a sample surface (the radii of the tips range from 10 to 100 nm) as seen in Fig. 1.3 [7], but the contact area usually consists of multiple atoms. Macro scale friction can be understood as an accumulation of the processes occurring at the individual asperities comprising the contact surface. Thus, the investigation of single-asperity friction using AFM is of fundamental importance.

Typical data from an AFM experiment is shown in Fig. 1.4 [16], where the lateral force is measured as a function of the tip position. This saw-tooth shape is typical in an AFM experiment and is an artifact of the so-called “stick-slip” motion. In the stick-stage, the atoms at the interface are arranged in a local equilibrium configuration, and the tip and the cantilever deforms elastically as the other end of the cantilever moves in the sliding direction. As a result, the lateral force, measured by the deformation of the cantilever, increases almost linearly. When the force exerted on the tip due to the elastic deformation exceeds the maximum force which the interface can withstand (the static friction), the tip disengages from the surface and suddenly moves in the sliding direction, sticking to the surface again in a new equilibrium configuration. During the slip phase, the deformation of the cantilever is relieved, the elastic energy is transformed into kinetic energy, and the measured lateral force drops suddenly. The kinetic energy is dissipated into atomic vibration (phonon) or the excitation of electrons, and this is the source of the kinetic friction.

At a finite temperature, the slip from one local equilibrium configuration to another can occur before the lateral force reaches the maximum frictional force of a given interface due to thermal activation. Thus, friction on the nano scale exhibits strong dependence on temperature and sliding rate. However, precise measurements of the relationships between friction and such external parameters have only recently been performed. Nevertheless, several recent achievements both in experiments and in theories have broadened our understanding of atomic scale friction. In the remaining of this section, we will review several experimental results, and the theories for atomic scale friction will be presented in Chap. III.

As an earliest attempt to study friction using AFM, Mate *et. al.* conducted an experiment with a tungsten tip scanning a graphite surface in ambient air and observed that the frictional force exhibits the stick-slip behavior with a periodicity corresponding to the surface structure of graphite [17]. They also reported that the frictional force has little dependence on the sliding speed over the range of 4 nm/s to 400 nm/s.

Tsukruk *et. al*. conducted experiments with mono-layers of a classic boundary lubricant, stearic acid (STA) and its cadmium salt (STCd) by varying the sliding velocities (20 nm/s ~ 1000 μm/s) [18] and found that in the solid state the frictional force reduces logarithmically as the velocity decreases while the fluid-state mono-layers displayed non-monotonic behaviors with the peaks around 0.2 μm/s. The logarithmic dependence of the frictional force on the sliding velocity was also observed by Gauthier *et.al.* [19]. They studied silane molecules (mono- and trichlorosilanes and mono- and triethoxysilanes) grafted on the silica surface by AFM and used the characteristic velocity dependencies to distinguish the surfaces obtained by different grafting processes. Later, Bouhacina *et. al.* showed the logarithmic dependence again with a polymer grafted on a silanized silica surface [20] and also constructed a model to explain this behavior using a thermally activated Eyring model [21].

The velocity dependence was also studied by Zwörner *et. al* [22]. They measured the frictional force of three different carbon compounds (diamond, highly oriented pyrolytic graphite (HOPG), and amorphous carbon) with a silicon tip in ambient air, but observed constant frictional force over a wide range of velocities (100 nm/s ~ 24.4 μm/s).

A decade ago, Gnecco *et. al*. reported a logarithmic dependence of the frictional force on velocity in the AFM experiments conducted in UHV (< 10^{-10} mbar) and at room temperature [8]. They varied the velocity from 5nm/s to 1 μm/s and observed the frictional force decreases logarithmically as the velocity decreases. More interestingly, they constructed a simple but very successful model considering the finite temperature effect based on the Tomlinson model [12] and were able to explain the logarithmic dependence. The detailed discussion of Gnecco's theory and several improved theories will be revisited in Chap. III.

Although a good deal of experimental data regarding the velocity dependence of atomic scale friction has been accumulated, the results are still puzzling; often logarithmic dependence is observed [8, 18-20], but in other cases the frictional force appears independent of the sliding rate [17, 22]. Moreover, the influence of temperature has been rarely reported until recently although a few interesting results have been reported [23-25]. Liang *et. al.* observed the frictional force of C_{60} molecules abruptly increases below ~260K where a first-order phase transition occurs from face-centered cubic (fcc) to simple cubic (sc) [23]. It is hypothesized that in the latter structure the free rotations of the C_{60} molecules are hindered. Sills and Overney varied both temperature (300 K ~ 365 K) and sliding velocity (30 nm/s ~ 2 μm/s) in the experiment with a silicon tip and an amorphous glassy polymer (the glass transition temperature is 373 K) [24] and observed the logarithmic dependence. Moreover, in an AFM experiment with a silicon tip and a silica substrate in humid air, a gas-liquid phase diagram of water at the interface of the tip and the substrate was constructed by varying the sample temperature (12 ^{o}C ~ 60 ^{o}C) with the environment temperature fixed at 20 ^{o}C [25].

A systematic measurement of the relationship between the frictional force and the sliding velocity over a wide range of temperatures was first performed by Schirmeisen *et. al.* [26]. They used a silicon tip scanning a silicon surface in [111] direction with natural oxide layers unremoved. The sliding velocity ranged from 100 nm/s to 16 μm/s, and they varied the temperature between 55 K and 255K and the experiment was conducted in

UHV (5×10^{-10} mbar). The frictional force displayed a varying relationship with the sliding velocity depending on temperature. For the temperatures below approximately 150 K, the frictional force showed the typical logarithmic dependence, but above 150 K the frictional force had no dependence on the sliding velocity. Moreover, they observed the friction coefficient and the jump-off force as temperature decreases, and instead of a monotonic increase, the results showed a peak of around 100 K and a subsequent drop. Zhao *et. al.* [27] also conducted an AFM experiment with a silicon nitride (Si_3N_4) tip and a graphite (HOPG) surface with a wide range of temperatures (140 K ~ 300 K) in UHV ($< 2 \times 10^{-10}$ torr), and reported an exponential increase in the frictional force as temperature decreases.

It is not likely that these observations of the dependence of atomic scale friction on sliding rate and temperature can be explained by a simple model like the Tomlinson model. This will require a realistic model that can consider the multi-atom nature of the contact, the atomic mixing between a tip and a substrate during the sliding, and the details of bond breaking and formation.

1.3 Molecular Dynamics Simulation

Molecular dynamics applies the laws of classical mechanics to deduce the properties of a system from the positions and momenta of the atoms comprising the system. The motions of the atoms are determined by a Hamiltonian, *H*, which is a function of all the particle positions, $\vec{r}_i$, and velocities, $\vec{v}_i$, as expressed in

$$H(\vec{r}_1, \cdots \vec{r}_N, \vec{v}_1, \cdots \vec{v}_N) = V(\vec{r}_1, \cdots \vec{r}_N) + K(\vec{v}_1, \cdots \vec{v}_N) \ , \qquad (1\text{-}1)$$

where *V* is the potential energy, *K* is the kinetic energy, and *N* is the total number of atoms.

The potential energy, $V(\vec{r}_1, \cdots \vec{r}_N)$, can be modeled by empirical potentials fit to experimental results or, when a higher accuracy is required, from quantum mechanical calculations. The system evolves in time according to Newton's equations of motion,

$$\begin{aligned} \dot{\vec{r}}_k &= \vec{v}_k \\ \dot{\vec{v}}_k &= -\frac{1}{m_k}\frac{\partial V(\vec{r})}{\partial \vec{r}_k} \qquad (k = 1, \cdots, N) \end{aligned} \ , \qquad (1\text{-}2)$$

where m_k is the mass of *k*th atom.

As the total energy of a system is conserved on the trajectory obtained from Eq. (1-2), the dynamics corresponds to sampling the points in the phase space according to the microcanonical ensemble (NVE) distribution. When the simulated system is not isolated such as the canonical ensemble (NVT), a different set of equations of motion must be employed to reproduce the corresponding probability distribution in phase space. To simulate the canonical ensemble in which the number of atoms (*N*), the volume (*V*), and the temperature (*T*) are constant, we can use the Nose-Hoover thermostat [28-31] with the equations of motion

$$\begin{aligned}
\dot{\vec{r}}_k &= \vec{v}_k \\
\dot{\vec{v}}_k &= -\frac{1}{m_k}\frac{\partial V}{\partial \vec{r}_k} - \eta \vec{v}_k \\
\dot{s} &= \eta \\
\dot{\eta} &= \frac{1}{Q}\left[\sum_{k=1}^{N} m_k \vec{v}_k \cdot \vec{v}_k - 3Nk_B T\right] \qquad (k = 1, 2, \cdots, N)
\end{aligned} \quad , \tag{1-3}$$

where η and s are the thermostat variables, Q is the thermostat mass, and k_B is the Boltzmann constant. It can be proven that the trajectory obtained from Eq. (1-2) generates the canonical ensemble [32].

When a system is in a transient state, where one of the external parameters like the volume changes, the Monte Carlo method cannot be used because it can only model systems in equilibrium. However, the MD method can still be applied to these systems as it is a direct simulation of the system dynamics. The accuracy of the MD simulation, however, depends on the ability of the potential energy function to describe the system as it evolves.

In many cases, MD simulations have been used to help explain the physical origins of experimental results. For example, in 1991, Krim *et. al.* reported QCM experimental results with Kr monolayers adsorbed on smooth and rough Au and Ag surfaces [33]. The magnitude of energy dissipation was quantified by simultaneously measuring the shift in the resonance frequency and the broadening of vibration resonance of quartz crystals with adsorbed monolayers. In this way, they observed that fluid films exhibited larger friction than solid films on a smooth Au surface, which was opposite to intuition. Three years later, Cieplak *et. al.* could explain the physical origin of the experimental results using MD simulations and perturbation theory [34]. They verified that solid monolayers comprising incommensurate interfaces can slide more easily than fluid monolayers. Moreover, recently, Wu *et. al.* conducted a pin-on-disk experiment of diamond-like carbon (DLC) with nanocomposite coatings [35] and also performed MD simulations to verify the triobological mechanism dominating the process. They found that the formation of lubricious layers at the interface by mixing of the materials can explain the low friction of WCS (DLS/WC/WS_2) coatings.

MD simulations were also used to investigate the fundamentals of friction. He *et. al.* [36] performed MD simulations to explain the discrepancy between the experimental results of two clean crystalline surfaces in UHV exhibited vanishing static friction in most cases while the real macroscale surfaces exhibited a nonzero static friction. These simulations employed a bead-spring model, representing hydrocarbons (common third bodies in the real interfaces) confined between two surfaces modeled by the Lennard-Jones potential. They showed that even incommensurate surfaces exhibit nonzero static friction in the presence of adsorbed molecules, so-called “the third bodies”. The normal force dependence of the frictional force agreed well with the Amontons’ macroscopic frictional law.

As nanotechnology advances and new experimental tools on a nano scale are invented and widely used, it has become possible to model some of experiments directly using MD. Three years after the AFM was first invented, Landman *et. al.* [37, 38] attempted to simulate the AFM experiment with a model consisting of a silicon tip and a silicon substrate. They used both sharp and larger tips and the larger tips had an ordered or disordered configuration. The silicon interactions were modeled by the Stillinger-Weber potential [39], and the simulation was performed at room temperature. They observed the stick-slip behavior and the transient and permanent changes in the local structure of the substrate depending on tip-substrate separation distance. Another attempt to model an AFM experiment of a copper tip and a copper substrate was made by Sørensen *et. al*. [40]. They simulated the system at the temperatures of 12 K and 300 K and at the sliding velocities of 1 m/s, 2m/s, and 10 m/s, and observed that the stick-slip motion depending on the tip and the substrate crystalline orientations and wear during the sliding. As one of the most recent examples, a realistic modeling of AFM tips using MD simulations was performed by Chandross *et. al*. [41]. They simulated AFM tips scanning amorphous silica substrates with alkylsilane self-assembled monolayers (SAMs). The tips were also made of amorphous silica and they realized amorphous structure by the melting of crystalline silica and the subsequent quenching. They found that the standard theories of contact mechanics based on the JKR (Johnson-Kendall-Roberts) [42] and DMT (Derjaguin-Muller-Toporov) [43] models cannot properly predict the relations between the applied load and the contact area mainly due to the intermediate layers. In the sliding simulation, they also observed that the frictional force does not depend on the chain length of the adsorbed monolayers. However, the sliding velocity used in the simulation was still large, 2 m/s.

Attempts to study the temperature and the sliding rate dependence of the frictional force using MD simulations have rarely been made. One notable exceptional study was conducted by Brukman *et.al.* [44]. AFM experiments with crystalline diamond tips and substrates at the temperatures ranging from 24 K and 225K exhibited a modest increase in shear strength with decreasing temperature. This dependence was also reproduced in the MD simulation.

One of the main problems of the previous studies using MD simulations is that the sliding rate is much higher than the actual AFM experimental values by several orders of magnitude. Thus, while the experiments have been performed at sliding velocities ranging from nm/s to μm/s, the simulations employed the sliding velocity of m/s. These simulation results obtained with the much larger sliding speed may not correctly reproduce the triobological behaviors of the system at the lower sliding rates. In the next three chapters, we will discuss these problems further and describe possible solutions.

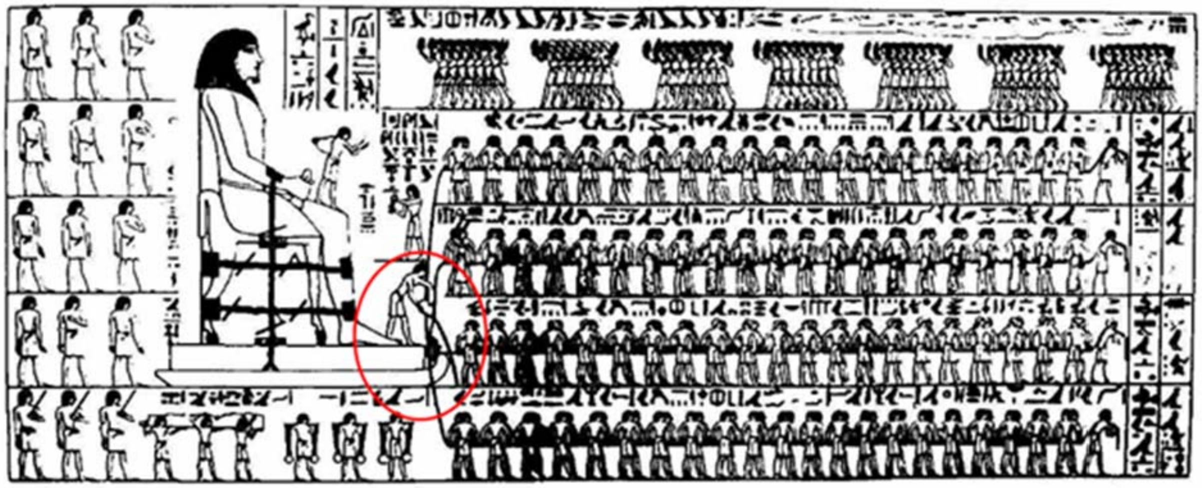

Figure 1.1 An ancient Egyptian picture that describes the transportation of a colossus on a sled. A person in the red circle is pouring an unknown liquid in front of the sled to facilitate the sliding [1].

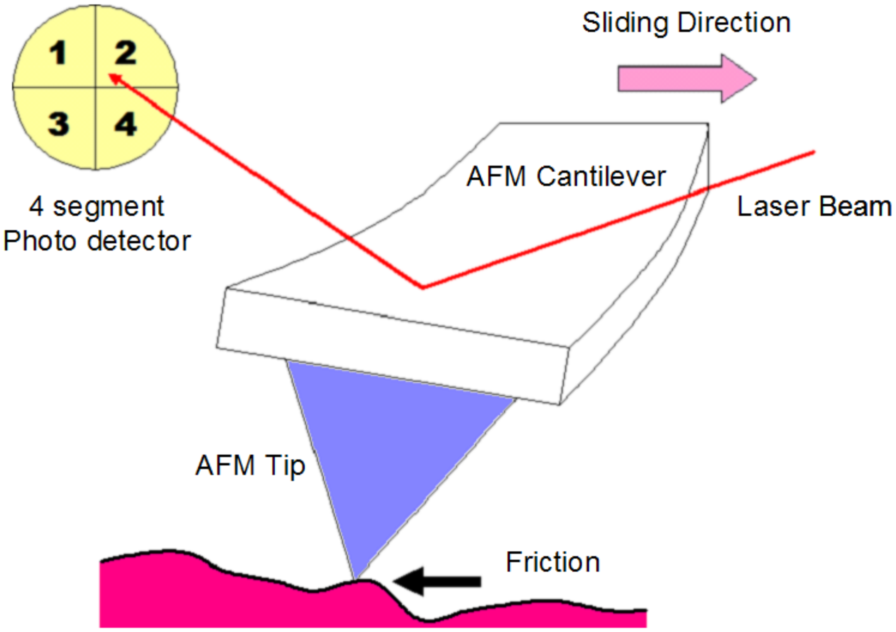

Figure 1.2 A schematic diagram of AFM in process.

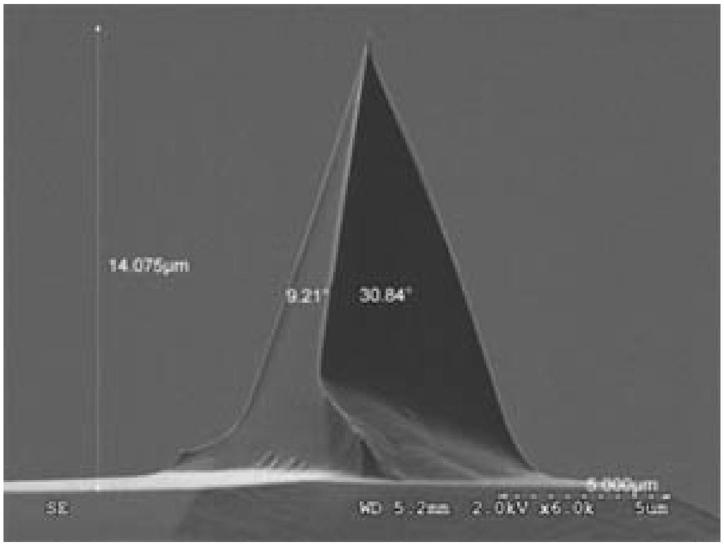

Figure 1.3 SEM micrograph of an AFM tip
(http://www.nanoscience.com)

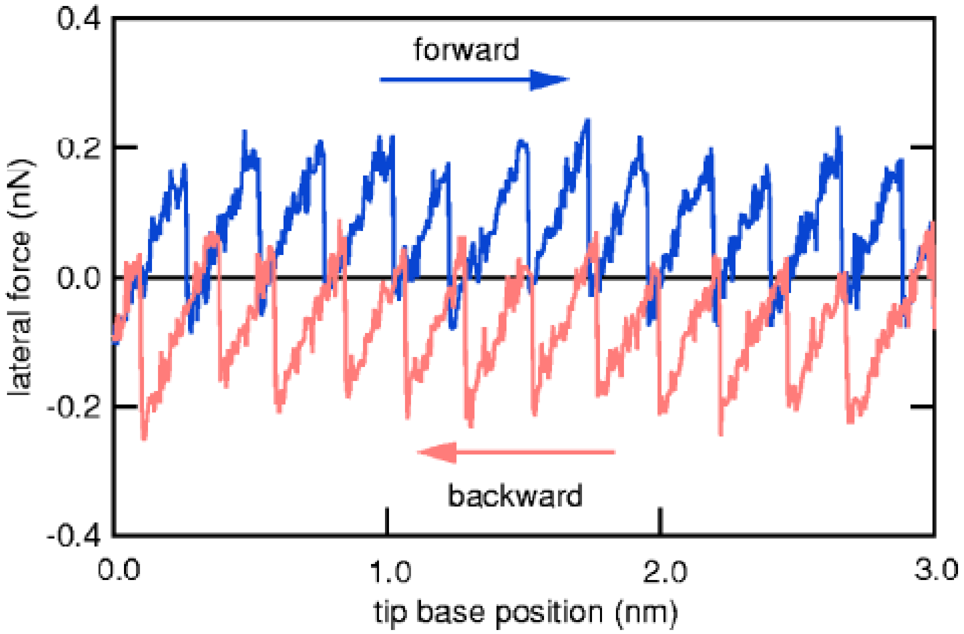

Figure 1.4 A typical AFM experimental result showing stick-slip behavior [16].

References

[1] D. Dowson, *History of Tribology* (1979).

[2] H. P. Jost, "*Tribology – Origin and Future*", Wear, 136, 1 (1990).

[3] M. P. de Boer and T. M. Mayer, "*Tribology of MEMS*", MRS Bull., 26, 302 (2001).

[4] J. N. Israelachvili and D. Tabor, "*Measurement of van-der-Waals Dispersion Forces in Range 1.4 to 130nm*", Nature, 236, 106 (1972).

[5] G. Binnig, C. F. Quate, and Ch. Gerber, "*Atomic Force Microscope*", Phys. Rev. Lett., 56, 930 (1986).

[6] J. Krim and A. Widom, "*Damping of a Crystal Oscillator by an Adsorbed Monolayer and its Relation to Interfacial Viscosity*", Phys. Rev. B, 38, 12184 (1988).

[7] R. W. Carpick, and M. Salmeron, "*Scratching the Surface: Fundamental Investigations of Tribology with Atomic Force Microscopy*", Chem. Rev., 97, 1163 (1997).

[8] E. Gnecco, R. Bennewitz, T. Gyalog, Ch. Loppacher, M. Bammerlin, E. Meyer, and H.-J. Güntherodt, "*Velocity Dependence of Atomic Friction*", Phys. Rev. Lett., 84, 1172 (2000).

[9] Y. Sang, M. Dube, and M. Grant, "*Thermal Effects on Atomic Friction*", Phys. Rev. Lett., 87, 174301 (2001).

[10] E. Riedo, E. Gnecco, R. Bennewitz, E. Meyer, and H. Brune, "*Interaction Potential and Hopping Dynamics Governing Sliding Friction*", Phys. Rev. Lett., 91, 084502 (2003).

[11] S. Y. Krylov, K. B. Jinesh, H. Valk, M. Dienwiebel, and J. W. M. Frenken, "*Thermally Induced Suppression of Friction at the Atomic Scale*", Phys. Rev. E, 71, 065101 (2005).

[12] G. A. Tomlinson, "*A Molecular Theory of Friction*", Philos. Mag., 7, 905 (1929).

[13] M. P. Allen and D. J. Tildesley, *Computer Simulation of Liquids* (1987).

[14] K. A. Fichthorn and W. H. Weinberg, "*Theoretical Foundations of Dynamical Monte Carlo Simulations*", J. Chem. Phys., 95, 1090 (1991).

[15] E. Martinez, J. Marian, M. H. Kalos, and J. M. Perlado, "*Synchronous Parallel Kinetic Monte Carlo for Continuum Diffusion-Reaction*", J. Compt. Phys., 227, 3804 (2008).

[16] A. Schirmeisen, L. Jansen, and H. Fuchs, "*Tip-Jump Statistics of Stick-Slip Friction*", Phys. Rev. B, 71, 245403 (2005).

[17] C. M. Mate, G. M. McClelland, R. Erlandsson, and S. Chiang, "Atomic-Scale *Friction of a Tungsten Tip on a Graphite Surface*", 59, 1942 (1987).

[18] V. V. Tsukruk, V. N. Bliznyuk, J. Hazel, and D. Visser, "*Organic Molecular Films under Shear Forces: Fluid and Solid Langmuir Monolayers*", Langmuir, 12, 4840 (1996).

[19] S. Gauthier, J. P. Aime, T. Bouhacina, A. J. Attias, and B. Desbat, "*Study of Grafted Silane Molecules on Silica Surface with an Atomic Force Microscope*", Langmuir, 12, 5126 (1996).

[20] T. Bouhacina, J. P. Aime, S. Gauthier, D. Michel, and V. Herguez, "*Tribologocal Behavior of a Polymer Grafted on Silanized Probed with a Nano tip*", Phys. Rev. B, 56, 7694 (1997).

[21] H. J. Eyring, "*The Activated Complex in Chemical Reactions*", J. Chem. Phys., 3, 107 (1935).

[22] O. Zwörner, H. Hölscher, U. D. Schwarz, and R. Wiesendanger, "*The Velocity Dependence of Frictional Forces in Point-Contact Friction*", Appl. Phys. A, 66, S263 (1998).

[23] Q. Liang, O. K. C. Tsui, Y. Xu, H. Li, and X. Xiao, "*Effect of C_{60} Molecular Rotation on Nanotribology*", Phys. Rev. Lett., 90, 146102, (2003).

[24] S. Sills and R. M. Overney, "*Creeping Friction Dynamics and Molecular Dissipation Mechanism in Glassy Polymers*", Phys. Rev. Lett., 91, 095501, (2003).

[25] R. Szoszkiewicz and E. Riedo, "*Nanoscopic Friction as a Probe of Local Phase Transitions*", Appl. Phys. Lett., 87, 033105 (2005).

[26] A. Schirmeisen, L. Jansen, H. Hölscher, and H. Fuchs, "*Temperature Dependence of Point Contact Friction on Silicon*", Appl. Phys. Lett., 88, 123108 (2006).

[27] X. Zhao, M. Hamilton, W. G. Sawyer, and S. S. Perry, "*Thermally Activated Friction*", Tribol. Lett., 27, 113 (2007).

[28] S. Nose, "*A Molecular Dynamics Method for Simulations in the Canonical Ensemble*", Molecular Physics, 52, 255 (1984).

[29] S. Nose, "A *Unified Formulation of the Constant Temperature Molecular Dynamics Methods*", J. Chem. Phys., 81, 511 (1984).

[30] W. G. Hoover, "*Canonical Dynamics: Equilibrium Phase-Space Distributions*", Phys. Rev. A, 31, 1695 (1985).

[31] G. J. Martyna, M. L. Klein, and M. Tuckerman, "*Nose-Hoover Chains: The Canonical Ensemble via Continuous Dynamics*", J. Chem. Phys., 97, 2635 (1992).

[32] M. E. Tuckerman, Y. Liu, G. Ciccotti, and G. J. Martyna, "*Non-Hamiltonian Molecular Dynamics: Generalizing Hamiltonian Phase Space Principles to Non-Hamiltonian Systems*", J. Chem. Phys., 115, 1678 (2001).

[33] J. Krim, D. H. Solina, and R. Chiarello, "*Nanotribology of a Kr Monolayer: A Quartz-Crystal Microbalance Study of Atomic-Scale Friction*", Phys. Rev. Lett., 66, 181 (1991).

[34] M. Cieplak, E. D. Smith, and M. O. Robbins, "*Molecular Origins of Friction: The Force on Adsorbed Layers*", Science, 265, 1209 (1994).

[35] J.-H. Wu, S. Karthikeyan, M. L. Falk, and D. A. Rigney, "*Tribological Characteristics of Diamond-like Carbon (DLC) based Nanocomposite Coatings*", Wear, 259, 744 (2005).

[36] G. He, M. M. Müser, and M. O. Robbins, "*Adsorbed Layers and the Origin of Static Friction*", Science, 284, 1650 (1999).

[37] U. Landman, W. D. Luedtke, and M. W. Ribarsky, "*Structural and Dynamical Consequences of Interactions in Interfacial Systems*", J. Vac. Sci. Technol., A7, 2829 (1989).

[38] U. Landman, W. D. Luedtke, and A. Nitzan, "*Dynamics of Tip-Substrate Interactions in Atomic Force Microscopy*", Surf. Sci., 210, L177 (1989).

[39] F. H. Stillinger and T. A. Weber, "*Computer Simulation of Local Order in Condensed Phases of Silicon*", Phys. Rev. B, 31, 5262 (1985).

[40] M. R. Sørensen, K. W. Jacobsen, and P. Stoltze, "*Simulations of Atomic-scale Sliding Friction*", Phys. Rev. B, 53, 2101 (1996).

[41] M. Chandross, C. D. Lorenz, M. J. Stevens, and G. S. Grest, "*Simulations of Nanotribology with Realistic Probe Tip Models*", Langmuir, 24, 1240 (2008).

[42] K. L. Johnson, K. Kendall, and A. D. Roberts, "*Surface Energy and the Contact of Elastic Solid*", P. Roy. Soc. Lond. A Mat., 324, 301 (1971).

[43] B. V. Derjaguin, V. M. Muller, and Y. P. Toporov, "*Effect of Contact Deformations on Adhesion of Particles*", J. Colloid Interf. Sci., 53, 314 (1975).

[44] M. J. Brukman, G. Gao, R. J. Nemanich, and J. A. Harrison, "*Temperature Dependence of Single-Asperity Diamond-Diamond Friction Elucidated Using AFM and MD Simulations*", J. Phys. Chem. C, 112, 9358 (2008).

CHAPTER II

Transition State Theory

2.1 Introduction

Most of the transient phenomena macroscopically observed in solid materials such as diffusion and creep are related to thermally activated changes in configuration of the atoms comprising the material. Atoms make transitions from one meta-stable potential energy basin to another when they gain enough energy to overcome the energy barrier due to thermal fluctuations. In these dynamical systems, the information about the waiting times at each state and the transition mechanisms leading to other states as well as their relative probabilities is essential to understand the underlying physics of the phenomena.

In many cases, before hopping to other states, the system stays in the neighborhood of a potential energy minimum for a very long time compared to the typical atomic vibration periods and a transition itself occurs in a relatively short time. In these situations, the transition rate is an equilibrium property that is independent of specific trajectories of the system. If we were able to enumerate all transitions and the rates, this would allow us to advance the system from one state to another, without following detailed trajectory in the configuration space. This is the fundamental assumption of Kinetic Monte Carlo (KMC) [1], which advances a system from one state to another according to known transition probabilities. Moreover, transition state theory (TST) can provide an analytical expression for the transition rates in an infrequently hopping system if a proper dividing surface that the system crosses in transitions can be constructed.

However, determining all transition mechanisms becomes more and more intractable as system complexity increases. For example, a replacement mechanism for surface diffusion, which was not recognized until 1990, later turned out to be a dominant mechanism in some metallic systems [2]. Direct simulation methods like MD do not assume any prior knowledge about how a system will evolve in time, and can be used to simulate unknown transition mechanisms. However, the limitation of time scales accessible with MD makes it difficult to use the methodology for infrequent event problems. Due to the short atomic vibration period, which is on the order of picoseconds, the overall time scale reachable by conventional MD technique is sub-microseconds.

The subsequent sections present preliminary information before we discuss a novel method to extend time scales accessible to direct simulations. In Sec. 2.2, the fundamental concepts of infrequent events are described. Sec. 2.3 reviews transition state theory and the concept of dividing surfaces. Finally, a comparison of the KMC method and the MD method is presented in detail in Sec. 2.4.

2.2 Infrequent Events

In infrequent events, the waiting times between successive transitions are much longer than the transition times so that we can assume that the system loses memory between transitions and the escape events from each state are uncorrelated with one another. This memoryless transition can be mathematically expressed as

$$p(t_A > t_1 + t_2) = p(t_A > t_1) \times p(t_A > t_2) \ , \tag{2-1}$$

where $p(t_A > t)$ is the probability that the waiting time at a state labeled by A, t_A, is longer than *t*. The probability density distribution satisfying the condition Eq. (2-1) is a Poisson distribution expressed as

$$p(t_A > t) = \exp(-R_A t) \ , \tag{2-2}$$

$$p(t_A = t) = -\frac{d\, p(t_A > t)}{d\, t} = R_A \exp(-R_A t) \ , \tag{2-3}$$

where R_A is a rate constant that characterizes the transition. The rate constant can also be expressed as

$$R_A = \frac{\upsilon_A}{p_A} \ , \tag{2-4}$$

where υ_A is the mean frequency of escape events from the state A, and p_A is the equilibrium population density in the state A, defined by

$$\upsilon_A = \lim_{\tau \to \infty} \frac{N_A}{\tau} \ , \tag{2-5}$$

and

$$p_A = \lim_{\tau \to \infty} \frac{\tau_A}{\tau} \ , \tag{2-6}$$

where τ is the total time elapsed by the system; N_A is the total number of escape events from A in this time interval; τ_A is the total time the system stays in A. If we further assume that the system stays at each state longer than the thermal equilibration time scale τ_{th}, then the system will sample the state A according to the equilibrium probability distribution. Thus, all measurables the system exhibits on a macroscopic time scale, including the transition rate, become equilibrium properties defined by the local state A.

In the same way, we can define the rate constant for each transition from A to one of its adjacent states (e.g., $R_{A\to B}$ for the transition from A to B), using the mean frequency of the corresponding events such that

$$R_{A\to B} = \frac{\upsilon_{A\to B}}{p_A} \quad , \tag{2-7}$$

and

$$\upsilon_{A\to B} = \lim_{\tau\to\infty} \frac{N_{A\to B}}{\tau} \quad , \tag{2-8}$$

where $N_{A\to B}$ is the total number of transitions from A to B in the time interval $[0, \tau]$. Then, the total rate constant is given by the sum of all the individual rate constants corresponding to a transition from A to one of its neighboring state,

$$R_A = R_{A\to B} + R_{A\to C} + R_{A\to D} + \cdots \ , \tag{2-9}$$

as $N_A = N_{A\to B} + N_{A\to C} + N_{A\to D} + \cdots$. The relative probabilities of the transitions to different states are given by

$$\frac{p_{A\to C}}{p_{A\to B}} = \lim_{\tau\to\infty}\left(\frac{N_{A\to C}}{N_{A\to B}}\right) = \frac{\upsilon_{A\to C}}{\upsilon_{A\to B}} = \frac{R_{A\to C}}{R_{A\to B}} \quad , \tag{2-10}$$

where $p_{A\to B}$ refers to the relative probability to the transition from A to B such that

$$p_{A\to B} + p_{A\to C} + p_{A\to D} + \cdots = 1 \quad . \tag{2-11}$$

Therefore, all the information needed to understand a dynamical system undergoing infrequent events can be obtained from the rate constants or equivalently the mean transition frequencies.

2.3 Transition State Theory

To obtain the frequency of transitions in Eq. (2-5), we need to observe a statistical number of escapes from the state in question so that we can count the total number of escapes to each neighbor and measure the escape time. Practically it is hard to observe even a single transition if we use a conventional dynamics scheme. Another approach would be to obtain the mean frequency using an ensemble average. This approach is called transition state theory (TST) and it was proposed as early as the 1930's [3]. In TST, a dividing surface separating a potential energy basin from others is defined. Then, the mean frequency of escape from the state A in Eq. (2-5) is replaced by the mean frequency of crossing the dividing surface and the population density of the state A in Eq. (2-6) can be approximated by the population density of a volume in the configuration space surrounded by the surface. It can be shown that these quantities are equivalent to the integrals,

$$\upsilon_A^{TST} = \frac{1}{2}\frac{\int d\vec{r}\int d\vec{v}\,|v_n|\,\delta_S(\vec{r})\exp[-(V+K)/k_BT]}{\int d\vec{r}\int d\vec{v}\exp[-(V+K)/k_BT]} , \tag{2-12}$$

and

$$p_A^{TST} = \frac{\int_A \exp[-V/k_BT]\,d\vec{r}}{\int \exp[-V/k_BT]\,d\vec{r}} , \tag{2-13}$$

where $\vec{r}$ is the 3*N*-dimensional position vector in the configuration space (*N* is the total number of particles); $\vec{v}$ is the 3*N*-dimensional velocity vector; v_n is the velocity normal to a dividing surface *S*; $\delta_S(\vec{r})$ is a Dirac-delta function located at the surface; k_B is the

Boltzmann constant, and *T* is the temperature. Note that it is assumed that the dynamics is ergodic.

Then, the TST rate constant, R_A^{TST} , is expressed as

$$R_A^{TST} = \frac{1}{2} \frac{\int d\vec{r} \int d\vec{v}\, |v_n|\, \delta_S(\vec{r}) \exp[-(V+K)/k_B T]}{\int_A d\vec{r} \int d\vec{v} \exp[-(V+K)/k_B T]} \quad . \tag{2-14}$$

Using the relation $\int \delta_S(\vec{r})\; f(\vec{r})\; d\vec{r} = \int_S f(\vec{r})\; dS$, an alternative expression can be obtained.

$$R_A^{TST} = \frac{1}{2} \frac{\int_S dS \int d\vec{v}\, |v_n| \exp[-(V+K)/k_B T]}{\int_A d\vec{r} \int d\vec{v} \exp[-(V+K)/k_B T]} \quad . \tag{2-15}$$

Eq. (2-15) can be regarded as the flux of the probability density in phase space, $\rho(\vec{r}, \vec{v}) = e^{-(V+K)/k_B T}$, exiting the surface *S*. Note that different dividing surfaces have different rates. The expression in Eq. (2-15) can be more simplified by formally integrating out velocity in specific cases:

$$R_A^{TST} = \sqrt{\frac{k_B T}{2\pi\mu}} \frac{\int_S dS \exp[-V/k_B T]}{\int_A d\vec{r} \exp[-V/k_B T]} \quad , \tag{2-16}$$

where μ is the effective mass. One trivial example is the case where all the atoms have the same mass *m*. In this case, $\mu = m$. If a hyperplane is used for a dividing surface, the effective mass is given by

$$\mu = \sum_{i=1}^{N} m_i\, (\vec{n}_i \cdot \vec{n}_i) \quad , \tag{2-17}$$

where $\vec{n}_i$ is a vector with three components of *i*th particle in the unit vector normal to the hyperplane such that $\sum_{i=1}^{N}(\vec{n}_i \cdot \vec{n}_i) = 1$ [4].

Because the TST rate constant is related to the mean frequency for crossing a given dividing surface, if a crossing of the surface exactly corresponds to an actual transition event, i.e. there is no recrossing of the surface, then the TST rate is identical to the actual rate. Otherwise, the TST rate always overestimates the actual rate, and

$$R_A^{TST} \geq R_A \quad . \tag{2-18}$$

Therefore, it is possible that a TST rate can be a poor approximation for the actual rate depending on which dividing surface is used; the choice of a proper dividing surface is critical for the success of TST.

One natural choice for a dividing surface is looking for a surface minimizing $R_A^{TST}(S)$, or equivalently minimizing the integral

$$I(S) = \int_S e^{-V(\vec{r})/k_B T}\, dS \quad , \tag{2-19}$$

because the smallest TST rate achievable is closest to the actual rate we can achieve with TST. This approach is referred to as variational TST and we can also derive a differential equation for such a surface by taking variation on Eq. (2-19) [5, 6]. However, in most cases it is too difficult to find such a surface, and it is more common to construct the dividing surface using a simple form like a plane [4, 6].

Further improvement can be achieved by introducing a dynamical correction factor f_d (< 1) which accounts for recrossing events [7-9]. f_d can be calculated by constructing trajectories initiated at the dividing surface. Once we compute the dynamical correction factor, the corrected rate is given by

$$(R_A^{TST})_{corrected} = f_d \, R_A^{TST} \quad . \tag{2-20}$$

One method for constructing a TST dividing surface uses the steepest ascent/descent path described by

$$\frac{d\vec{r}}{ds} = \pm \frac{\nabla V}{|\nabla V|} \quad , \tag{2-21}$$

where $ds \, (= |d\vec{r}|)$ is the arc length of the *3N*-dimensional curve in the configuration space [10]. All the points which can be led to a minimum by the steepest descent path comprise the state defined by the minimum, and the points on the boundary, which converge to one of the first-order saddle points instead of the minimum points, define the TST dividing surface. In this case minimization can be used to verify whether or not a system crosses the dividing surface on the fly, by following the path described by Eq. (2-21) and checking if the current position converges to the original minimum. However, it is not practical to construct such a surface because we would need to identify all the first-order saddle points. Moreover, at a finite temperature, there is no guarantee that the TST dividing surface defined by the steepest ascent/descent path is equivalent to the variational TST dividing surface.

When a certain first-order saddle point is identified, an approximate expression for the TST rate constant corresponding to a transition via the saddle point can be obtained by an approach known as the harmonic TST [11]. First, to calculate the integral in the denominator of Eq. (2-16), the potential energy is expanded using Taylor series around the minimum,

$$V(\vec{r}) = V_M + \frac{1}{2}\vec{r} \cdot (\underline{\underline{H}}\,\vec{r}) + O(r^3) \quad , \tag{2-22}$$

where V_M is the potential energy at the minimum, and $\underline{\underline{H}}$ is the Hessian matrix ($H_{ij} = \partial^2 V / \partial r_i \partial r_j$). Note that the coordinates are centered at the minimum. Then, the integral is given by

$$\int_A e^{-V/k_B T}\, d\,\vec{r} \approx \int_A e^{-V_M/k_B T - \frac{1}{2}\vec{r} \cdot (\underline{\underline{H}}\,\vec{r})/k_B T}\, d\,\vec{r} \tag{2-23-a}$$

$$\approx \int e^{-V_M/k_B T - \frac{1}{2}\vec{r} \cdot (\underline{\underline{H}}\,\vec{r})/k_B T}\, d\,\vec{r} \tag{2-23-b}$$

$$= e^{-V_M/k_B T} \int e^{-\frac{1}{2}\sum_{i=1}^{3N} k_M^i (q^i)^2 / k_B T}\, dq^1\, dq^2 \cdots dq^{3N} \tag{2-23-c}$$

$$= e^{-V_M/k_B T} \prod_{i=1}^{i=3N} \sqrt{\frac{2\pi\, k_B T}{k_M^i}} \quad , \tag{2-23-d}$$

where k_M^i is the *i*th eigenvalue of the Hessian matrix at the minimum. Note that the local integral in Eq. (2-23-a) is approximated by the global integral in Eq. (2-23-b) because the expanded potential energy is dominant around the minimum, and in Eq. (2-23-c) the coordinates are transformed into a new coordinates system defined by the eigenvectors (q^i is a component along the *i*th eigenvector).

For the surface integral in the numerator of Eq. (2-16), the dividing surface is approximated as a hyperplane normal to the eigenvector corresponding to the lowest eigenvalue of the Hessian at the saddle point and passing through the saddle point. Then, the potential energy on the plane can be expanded around the saddle point with a new coordinates system defined by the 3*N*-1 eigenvectors,

$$V(\vec{r}) \approx V_S + \frac{1}{2}\sum_{i=1}^{3N-1} k_S^i (q^i)^2 \quad , \tag{2-24}$$

where k_S^i is the ith eigenvalue of the Hessian matrix at the saddle point and the indices are relabeled excluding the lowest one. Then, the integral is given by

$$\int_S e^{-V/k_BT}\, dS \approx e^{-V_S/k_BT} \int e^{-\frac{1}{2}\sum_{i=1}^{3N-1} k_S^i (q^i)^2/k_BT}\, dq^1\, dq^2 \cdots dq^{3N-1} \tag{2-25-a}$$

$$= e^{-V_S/k_BT} \prod_{i=1}^{i=3N-1} \sqrt{\frac{2\pi k_BT}{k_S^i}} \quad . \tag{2-25-a}$$

Finally, the harmonic TST rate constant when the two states are labeled by A and B is given by

$$R_{A\to B}^{HTST} = \sqrt{\frac{k_BT}{2\pi m}} \frac{e^{-V_S/k_BT} \prod_{i=1}^{i=3N-1} \sqrt{\frac{2\pi k_BT}{k_S^i}}}{e^{-V_M/k_BT} \prod_{i=1}^{i=3N} \sqrt{\frac{2\pi k_BT}{k_M^i}}} \quad , \tag{2-26-a}$$

$$= \upsilon_O \exp[-\Delta V / k_BT] \quad . \tag{2-26-b}$$

where υ_O is the attempt frequency and ΔV is the energy barrier, which are defined by

$$\upsilon_O = \frac{\prod_{i=1}^{i=f} \upsilon_M^i}{\prod_{i=1}^{i=f-1} \upsilon_S^i} \quad , \tag{2-27}$$

$$\Delta V = V_S - V_M \quad , \tag{2-28}$$

$$\upsilon_S^i = \frac{1}{2\pi}\sqrt{\frac{k_S^i}{m}} \quad , \tag{2-29}$$

$$\upsilon_M^i = \frac{1}{2\pi}\sqrt{\frac{k_M^i}{m}} \quad . \tag{2-30}$$

For simplicity, it is assumed that all the particles have the same mass *m*.

From these observations, it is worth noting that the TST dividing surface depends on the global properties of a given potential energy surface. Thus, we cannot, in general, determine whether or not a system crosses the surface just by looking at the neighborhood of the position. Ideally we must solve the variational TST dividing surface problem or, alternatively, all the first-order saddle points must be identified. In most cases either presents a formidable task.

There are several ways which have been proposed to approximate a dividing surface using local properties. One of those methods was proposed by Sevick *et. al.* [10]. In their approach, they noticed that at a saddle point, which provides the dominant contribution to the numerator of Eq. (2-15) or Eq. (2-16), the lowest eigenvalue ε_1 of the Hessian matrix is negative and the corresponding eigenvector $\vec{C}_1$ is perpendicular to the dividing surface based on the steepest ascent/descent method. Thus, they constructed a surface satisfy the following conditions

$$\vec{C}_1 \cdot \nabla V = 0 \quad \text{and} \quad \varepsilon_1 < 0 \ . \tag{2-31}$$

Fig. 2-1 shows various dividing surfaces and the dividing surface constructed by Eq. (2-31) can be a good approximation near the saddle point.

2.4 Kinetic Monte Carlo and Molecular Dynamics

Suppose a system evolving via infrequent transition events among various potential energy wells. Molecular dynamics simulations compute the positions and momenta of the system following a trajectory of the particles as time passes. Thus, it corresponds to simulating real dynamics. After initially setting the system in progress, we monitor the system for a time period as in real experiments. We do not need to know *a priori* which pathways the system will follow when making transitions.

Unlike the Monte Carlo Method, the Kinetic Monte Carlo method treats dynamical systems evolving in time. However, its approach is different from the MD method. In KMC, we assume that all the transition mechanisms and their transition rates are known. These are inputs for KMC simulations. Then, KMC can advance the system according to these transition rates. For example, suppose that we have three transition modes, labeled by 1, 2, and 3, and their transition rates are known and expressed as R_1, R_2, and R_3. Then, their relative transition probabilities are $R_1 : R_2 : R_3$ as seen in Eq. (2-10), and we can choose one transition mode to advance the system according to these probabilities, e.g., by generating a random number. Moreover, we can estimate the escape time corresponding to this transition. Recall that the escape time does not have a determined value, but has a probability distribution as in Eq. (2-3). Then, it can be shown that a variable *t* calculated by

$$t = -\frac{\ln(r)}{R} \quad , \tag{2-32}$$

where r is a random number uniformly distributed in [0,1] and R is the total rate ($= R_1 + R_2 + R_3$), has the Poisson distribution $R e^{-Rt}$.

Surprisingly, we can advance the system from one state to another just by generating two random numbers. If we performed a MD simulation, we would have to continually trace a trajectory until the system undergoes a transition. Thus, KMC has significant advantages over MD in rare events problems.

The weak point of KMC is the assumption that all the major transition modes are identified and their rates are known. In complicated systems this is an intractable condition. In chapter IV, we will introduce a novel method to extend MD time-scales using TST.

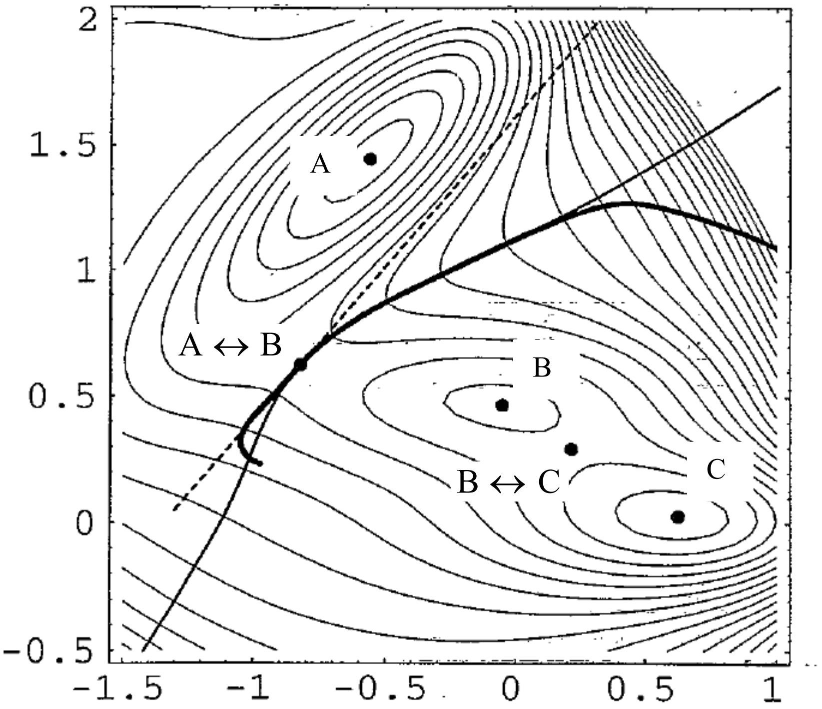

Figure 2.1 Contours and dividing surfaces of the two-dimensional Muller potential energy surface. The surface has three minima, labeled A, B, and C, and two saddle points, labeled $\mathrm{A} \leftrightarrow \mathrm{B}$ and $\mathrm{B} \leftrightarrow \mathrm{C}$. The thin solid curve is obtained from the steepest ascent/descent method, the dashed straight line is the hyper-surface perpendicular to the eigenvector for the lowest eigenvalue at the saddle point, and the thick solid line represents the dividing surface based on Eq. (2-21) [10].

References

[1] K. A. Fichthorn and W. H. Weinberg, "*Theoretical Foundations of Dynamical Monte Carlo Simulations*", J. Chem. Phys., 95. 1090 (1991).

[2] P. J. Feibelman, "*Diffusion Path for an Al Adatom on Al (001)*", Phys. Rev. Lett., 65, 729 (1990).

[3] H. Eyring, "*The activated complex in chemical reactions*", J. Chem. Phys., 3, 107 (1935).

[4] G. H. Johannesson and H. Jonsson, "*Optimization of Hyperplanar Transition States*", J. Chem. Phys., 115, 9644 (2001).

[5] J. Horiuti, "*On the Statistical Mechanical Treatment of the Absolute Rate of Chemical Reaction*", Bull. Chem. Soc. Jpn., 13, 210 (1938).

[6] E. Vanden-Eijden and F. A. Tal, "*Transition State Theory: Variational Formulation, Dynamical Corrections, and Error Estimates*", J. Chem. Phys., 123, 184103 (2005).

[7] J. Keck, "*Statistical Investigation of Dissociation Cross-Sections for Diatoms*", Discuss. Faraday Soc., 33, 173 (1962).

[8] D. Chandler, "*Statistical Mechanics of Isomerization Dynamics in Liquids and the Transition State Approximation*", J. Chem. Phys., 68, 2959 (1978).

[9] A. F. Voter and J. D. Doll, "*Dynamical Corrections to Transition State Theory for Multistate Systems: Surface Self-Diffusion in the Rare-Event Regime*", J. Chem. Phys., 82, 80 (1985).

[10] E. M. Sevick, A. T. Bell, and D. N. Theodorou, "*A Chain of States Method for Investigating Infrequent Event Processes Occurring in Multistate, Multidimensional Systems*", J. Chem. Phys., 98, 3196 (1993).

[11] G. H. Vineyard, "*Frequency Factors and Isotope Effects in Solid State Rate Processes*", J. Phys. Chem. Solids, 3, 121 (1957).

CHAPTER III

Theories of Atomic-scale Friction

3.1 Introduction

In an AFM experiment, only a small number of atoms at the end of a tip are in contact with the atoms in the substrate. They are initially equilibrated at a local potential energy minimum, but as the slider moves and the cantilever deforms, the initial minimum configuration becomes unstable and the atoms rearrange into a more stable new minimum releasing the elastic energy stored in the cantilever. This process: equilibration at a local minimum, escape from the minimum and establishment of a new local minimum, is repeated as the slider advances.

To quantitatively explain the characteristics of atomic-scale friction observed in the AFM experiment, several theories, based on the Tomlinson model [1], have been proposed [2-5]. Although they cannot explain every detail of the various phenomena that accompany frictional sliding, these theories give us insight into the underlying physics, and exhibit a velocity and temperature dependent friction force and stick-and-slip motion. In this chapter, we will present the Tomlinson model and then consider theories arising from the model that take into account thermally activated transitions. Other models considering the vibrational coupling between atoms (the Frenkel-Kontorova model [6, 7]) and the coupling between atoms and the sliding body (the Frenkel-Kontorova-Tomlinson model [8]) are discussed in Sec. 3.4. Finally, Sec. 3.5 will discuss the contact mechanics.

3.2 Tomlinson Model

Let us consider a simple system consisting of one atom which interacts with a crystalline surface and is attached to a spring as seen in Fig. 3.1 (a). The crystalline surface is modeled by a sinusoidal function, which has a periodicity of a, and the other end of the spring is a slider moving at a constant speed, υ_S. We can regard this system as an AFM experiment with an extremely sharp tip having a single-atom contact and scanning a crystalline surface. The spring models the combined stiffness of the tip and the cantilever.

The total potential energy of the system, U, is the sum of the surface interaction potential, E_i, and the harmonic potential due to the spring, E_h, expressed as

$$U(x, x_S) = E_i(x) + E_h(x, x_S) \quad , \tag{3-1}$$

$$E_i(x) = \frac{E_O}{2}\left[1 - \cos\left(\frac{2\pi x}{a}\right)\right] \quad , \tag{3-2}$$

$$E_h(x, x_S) = \frac{k}{2}(x_S - x)^2 \quad , \tag{3-3}$$

$$x_S = v_S\, t \quad , \tag{3-4}$$

where E_O is the energy barrier of the surface interaction and k is the spring constant.

Fig. 3.1 (a) shows the potential energy curves when the spring is unstretched. In this configuration, the atom is at the initial minimum indicated by the green triangle in the figure. As the slider moves to the right (the sliding direction) and stretches the spring, the location of the harmonic potential and the shape of the total potential change and, in turn, the location of the initial minimum moves continuously. The energy barrier to the right side (state B) of the initial minimum (state A), $\Delta E_{A\rightarrow B}$, also reduces as successively shown in Fig. 3.1 (b) ~ (f). At a finite temperature, the atom will vibrate around this instantaneous minimum, but for the present let us assume that the atom is always located at the minimum. When the slider reaches a critical point (x_S^+), where the energy barrier completely vanishes as shown in Fig. 3.1 (f), the atom can hop from the initial minimum, x_1, to the next one, x_2, and the friction force drops abruptly as the tip slips to a new stable configuration. A typical tip motion and a friction force graph are illustrated as functions of the slider position in Fig. 3.2. When the atom hops to a new local minimum, the stored elastic energy due to the spring is released and transforms into kinetic energy. In a real material, this kinetic energy gain is dissipated via phonons and the electronic excitations, and this mechanism is the source of kinetic friction. In the present model, we will simply assume kinetic energy is fully dissipated as heat and the atom at the tip is always at the minimum.

Now let us derive several analytical expressions that will be important for our discussion in the subsequent section. The energy barrier is a function of the slider position given by

$$\Delta E_{A\rightarrow B}(x_S) = U(x_{sad}(x_S), x_S) - U(x_{\min}(x_S), x_S) \quad , \tag{3-5}$$

where x_{sad} and $x_{\min}$ refer to the saddle point and the initial minimum and are also functions of the slider position. x_{sad} and $x_{\min}$ can be obtained by solving the following equations,

$$\frac{\partial E_i(x)}{\partial x}+\frac{\partial E_h(x, x_S)}{\partial x}=0 \quad , \tag{3-6}$$

$$\frac{\partial E_i(x)}{\partial x}=\frac{\pi \Delta E}{a}\sin\left(\frac{2\pi x}{a}\right) \quad , \tag{3-7}$$

and

$$\frac{\partial E_h(x, x_S)}{\partial x}=k\,(x-x_S) \quad . \tag{3-8}$$

As illustrated in Fig. 3.3 (a), x_{sad} and $x_{\min}$ correspond to the crossing points of the two curves corresponding to Eq. (3-7) and Eq. (3-8), and the energy barrier is the area between two curves bounded by x_{sad} and $x_{\min}$. We can also show that the following relationship holds,

$$\frac{d\,(\Delta E_{A\to B})}{d\,x_S}=k\,(x_{\min}-x_{sad}) \quad . \tag{3-9}$$

Note that Eq. (3-9) is always negative. Moreover, the dependence of x_{sad} and $x_{\min}$ on the slider position can be shown as

$$\frac{d\,x_{\min}}{d\,x_S}=\frac{k}{k+\left.\frac{d^2\,E_i}{d\,x^2}\right|_{x_{\min}}} \quad , \tag{3-10}$$

$$\frac{d\,x_{sad}}{d\,x_S}=\frac{k}{k+\left.\frac{d^2\,E_i}{d\,x^2}\right|_{x_{sad}}} \quad . \tag{3-11}$$

Note that $\frac{d^2E_i}{d\,x^2} < -k \quad at \;\; x=x_{sad}$.

The lateral force, *F*, is defined as

$$F = k\,(x_S - x_{\min})\ , \qquad (3\text{-}12)$$

and we define the upper critical lateral force, F_C^+, as the lateral force when the energy barrier completely vanishes ($x_C = x_{sad} = x_{\min}$ and x_S becomes x_S^+). x_C and x_S^+ can also be expressed as

$$x_C = \frac{a}{2\pi}\cos^{-1}\left(-\frac{k\,a^2}{2\pi^2 E_O}\right) , \qquad (3\text{-}13)$$

$$x_S^+ = x_C + \frac{\pi E_O}{k\,a}\sin\left(\frac{2\pi\, x_C}{a}\right) . \qquad (3\text{-}14)$$

In the derivations above, we assumed that there is more than one local minimum, *i.e.* there are always saddle points, but the number of wells depends on the spring stiffness. As shown in Fig. 3.3 (b), when the stiffness is larger than k_{cr1}, initially there exists only one well and as the slider advances additional wells appear. If $k > k_{cr2}$, regardless of the slider position there is only one local minimum. The critical stiffnesses, k_{cr1} and k_{cr2}, can be expressed as

$$k_{cr1} = -\frac{2\pi^2 E_O}{a^2}\cos(s_1) \quad , \qquad (3\text{-}14)$$

and

$$k_{cr2} = \frac{2\pi^2 E_O}{a^2} \quad , \qquad (3\text{-}15)$$

where $s_1 \cong 4.493$ is one of the roots of the equation $\tan(s) = s$. When $k > k_{cr2}$ there is no stick-slip motion and no energy dissipation in the model because there is no transition. This is the regime exhibiting so-called superlubricity, almost vanishing friction force which will be discussed in detail in Sec. 3.4 [9].

The upper critical lateral force can be expressed in terms of k_{cr2}, as

$$F_C^+ = \frac{\pi E_O}{a}\sqrt{1-\left(\frac{k}{k_{cr2}}\right)^2} \quad . \tag{3-16}$$

If $k < k_{cr1}$, there are multiple wells when the spring is not stretched and the atom has a probability to make a transition to neighboring states.

3.3 Thermally Activated Transition

Temperature affects transitions between states and alters the frictional behavior. The positions of atoms comprising a material in the solid state fluctuate in a way characterized by the temperature. As a result of these fluctuations, even though there is a non-vanishing energy barrier, the system can overcome the barrier and make a transition to one of the neighboring minima due to the thermal energy. In general, with a given energy barrier, the transition is more probable at a higher temperature. Thus, we can expect that in the sliding system, the tip can make a transition at earlier slider positions as the temperature becomes higher, resulting in a smaller friction force.

To analyze the thermally activated transition in a systematic way, let us consider transitions between two wells (or states) illustrated in Fig. 3.4, where two states are labeled by A and B, respectively. Assuming the potential energy is not changing and the system is initially at A, the probabilities that the system will be at A and B at the time t, $p_A(t)$ and $p_B(t)$, can be given by the following rate equations

$$\frac{d\,p_A(t)}{dt} = -R_{A\to B}\; p_A + R_{B\to A}\; p_B \quad , \tag{3-17}$$

$$\frac{d\,p_B(t)}{dt} = +R_{A\to B}\;p_A - R_{B\to A}\;p_B \quad , \tag{3-18}$$

with $p_A(0)=1$ and $p_B(0)=0$, where $R_{A\to B}$ and $R_{B\to A}$ are the transition rates from A to B and from B to A, respectively. If we further assume that the transition from B to A is much less probable compared to the transition from A to B ($\Delta E_{A\to B} << \Delta E_{B\to A}$), the rate equations can be simplified as

$$\frac{d\,p_A(t)}{dt} \cong -R_{A\to B}\;p_A \quad . \tag{3-19}$$

The rate $R_{A\to B}$ can be estimated by transition state theory. In this one-dimensional case Eq. (2-16) gives

$$R^{TST}_{A\to B} = \sqrt{\frac{k_B T}{2\pi m}}\;\frac{e^{-E(x_{sad})/k_B T}}{\int_{-\infty}^{x_{sad}} e^{-E(x)/k_B T}\,d\,x} \quad . \tag{3-20}$$

If we use the harmonic approximation, a simpler expression can be used to estimate the rate constant $R_{A\to B}$ as

$$R^{HTST}_{A\to B} = \sqrt{\frac{k_m}{2\pi m}}\,\exp\left(-\frac{\Delta E_A}{k_B T}\right), \tag{3-21}$$

$$= f_O \exp\left(-\frac{\Delta E_A}{k_B T}\right) \quad , \tag{3-22}$$

where k_m is the curvature at the minimum and f_O is the attempt frequency. Moreover, the probability that the system hops from A to B at time *t*, $g_A(t)$, is given by

$$g_A(t) = -\frac{d\,p_A(t)}{dt} = +R_{A\to B}\;p_A(t) \quad . \tag{3-23}$$

In the Tomlinson model, the energy barrier is not fixed, but changes as a function of the slider position x_S. If we assume that the slider moves so slowly that the system is at near equilibrium at any slider position, although ΔE_A changes in time, Eq. (3-19) is still valid with the transition rates given by Eq. (3-20) or Eq. (3-21). Then, with Eq. (3-4), we can rewrite these equations in terms of the slider position as,

$$\frac{d\,p_A(x_S)}{d\,x_S} = -\frac{R_{A\to B}(x_S)}{v_S}\,p_A(x_S) \ , \tag{3-24}$$

$$R_{A\to B}(x_S) = f_O \exp\left(-\frac{\Delta E_A(x_S)}{k_B T}\right) , \tag{3-25}$$

and

$$g_A(x_S) = R_{A\to B}(x_S)\,p_A(x_S) \ . \tag{3-26}$$

The solutions under these assumptions are

$$p_A(x_S) = \exp\left[-\frac{1}{v_S}\int_0^{x_S} R_{A\to B}(x_S)\,d\,x_S\right] \ , \tag{3-27}$$

and

$$g_A(x_S) = R_{A\to B}(x_S)\exp\left[-\frac{1}{v_S}\int_0^{x_S} R_{A\to B}(x_S)\,d\,x_S\right] . \tag{3-28}$$

The most probable slider position for the transition, $\tilde{x}_S$, can be found by the condition,

$$\left.\frac{d\,g_A}{d\,x_S}\right|_{\tilde{x}_S} = 0 \ . \tag{3-29}$$

Using Eq. (3-26) and Eq. (3-28), this condition becomes

$$\frac{R_{A\to B}^2}{v_S} = \frac{d\,R_{A\to B}}{d\,x_S} \ , \tag{3-30}$$

and from (3-25) and assuming f_O is constant , we can obtain a general relation that holds in the harmonic limit,

$$f_O \exp\left(-\frac{\Delta E_A(\tilde{x}_S)}{k_B T} \right) = -\frac{v_S}{k_B T} \frac{d\,\Delta E_A}{d\,x_S}\bigg|_{\tilde{x}_S} \quad . \tag{3-31}$$

Now let us express these relations in terms of the lateral force defined in Eq. (3-12). If the contact stiffness, $k_C \left(= \frac{d^2 E_i}{d\,x^2} \right)$, is constant, Eq. (3-12) can be rewritten as

$$F = k_{eff}\ x_S \ , \tag{3-32}$$

where $k_{eff} = k_C\, k/(k_C + k)$ is the effective stiffness. Then, we can show that the probability that the system hops from A to B at force *F*, $g_A(F)$, is

$$g_A(F) = R_{A\to B}(F) \exp\left[-\frac{1}{k_{eff}\, v_S} \int_0^F R_{A\to B}(F)\, d\,F \right] \quad , \tag{3-33}$$

where $R_{A\to B}(F) = f_O \exp\left(-\frac{\Delta E_A(F)}{k_B T} \right)$. From the position dependence of the energy barrier and the lateral force, we can obtain $g_A(F)$ by solving Eq. (3-33). In this way we can demonstrate that the average lateral force at the transition is given by

$$\overline{F} = \int_0^{F_C^+} F\ g_A(F)\, d\,F \quad . \tag{3-34}$$

Gnecco *et. al*. first derived a relation of this sort by assuming the energy barrier reduces linearly as the slider moves [2],

$$\Delta E_A = \lambda\, (F_C^+ - F) \ , \tag{3-35}$$

where λ is a constant and ΔE_A becomes zero as F approached to F_C^+. Then, the most probable lateral force for the transition, $\widetilde{F}$, becomes

$$\widetilde{F} = F_C^+ + \frac{k_B T}{\lambda} \ln\left[\frac{\lambda k_{eff} v_S}{f_O k_B T} \right] \quad . \tag{3-36}$$

Note that the lateral force is logarithmically proportional to the sliding velocity.

In subsequent work, Sang *et. al*. [3] showed that when the lateral force is close to the critical force, the correct relation of ΔE_A is

$$\Delta E_A = \gamma (F_C^+ - F)^{3/2} \quad , \tag{3-37}$$

which is the same relation Maloney and Lacks derived based on Catastrophe theory [10]. From this assumption they derive an expression for the transition probability near the critical force,

$$g_A(f) = \frac{3}{2} \frac{f^{1/2}}{v^*} \exp[- f^{3/2} - (e^{-f^{3/2}})/v^*] \quad , \tag{3-38}$$

where $f = C_1(F_C^+ - F)$ and $v^* = C_2 v_S$ (C_1 and C_2 are constants). A typical distribution is shown in Fig. 3.5 (a). They also obtained the relationship between the average force Eq. (3-34) and the sliding velocity in this limit,

$$\overline{F} = A - B(\ln v_S)^{2/3} \quad , \tag{3-39}$$

where *A* and *B* are constants.

Later, Riedo *et. al.* derived a formula for the most probable transition force and the velocity relation using Sang's equation and assuming f_O is constant [4],

$$\frac{\gamma}{k_B T}(F_C^+ - \widetilde{F})^{3/2} = \ln\left[\frac{2 k_B T f_O}{3 \gamma k_{eff} \sqrt{F_C^+} v_S} \right] - \frac{1}{2} \ln\left[1 - \frac{\widetilde{F}}{F_C^+} \right] . \tag{3-40}$$

Note that in Eq. (3-40), $\widetilde{F}$ approaches F_C^+ asymptotically as the sliding velocity increases and there is a plateau region at the higher velocity region as shown in Fig. 3.5 (b).

In the above derivations, we considered a unidirectional transition from A to B and ignored other possibilities. Recently, Krylov *et. al.* [5] proposed another mechanism for superlubricity, called thermolubricity, by studying all the possible transitions in the Tomlinson model. They solved a set of rate equations including all the minima of the model,

$$\frac{d\,p_i(t)}{dt} = -(R_i^+ + R_i^-)\;p_i + R_{i-1}^+ p_{i-1} + R_{i+1}^- p_{i+1} \quad , \qquad (i = 1, \cdots, N_w) \tag{3-41}$$

$$R_i^\pm = f_O \exp\left[-\frac{\Delta E_i^\pm}{k_B T}\right] \ , \tag{3-42}$$

$$R_1^- = R_{N_w}^+ = 0 \ , \tag{3-43}$$

where N_w is the total number of wells, R_i^+ is the transition rate from the *i*th well to the right, R_i^- is the transition rate from the *i*th well to the left, and $\Delta E_i^\pm$ are corresponding energy barriers. Moreover, they introduced a non-dimensional parameter β given by

$$\beta = \frac{\tau_1}{\tau_2} \quad , \tag{3-44}$$

$$\tau_1 = \frac{1}{f_O} \exp\left[\frac{E_O}{k_B T}\right] \ , \tag{3-45}$$

$$\tau_2 = \frac{a}{v_S} \quad . \tag{3-46}$$

When $\beta << 1$ ($\tau_1 << \tau_2$), called *the thermal drift regime*, the tip can exhibits many back-and-forth transitions among adjacent wells before the slider substantially moves. In this regime, the stick-slip breaks down and a significant reduction of friction force could be obtained. This can be confirmed by the analytical solution in this regime.

$$\overline{F} \sim v_S \left(\frac{k}{f_O}\right)\left(\frac{E_O}{k_B T}\right)\exp\left[\frac{E_O}{k_B T}\right] \; . \tag{3-47}$$

Eq. (3-47) implies that the friction force becomes zero at zero velocity limit and increases exponentially as temperature decreases. While the criterion for superlubricity, $k > k_{cr2}$, considers only mechanical properties of the system, the superlubricity observed in the thermal drift regime is mainly due to thermally effects and called thermolubricity.

3.4 Frenkel-Kontorova-Tomlinson Model

In Sec. 3.2 and Sec. 3.3 we discussed the Tomlinson model and the theories based on this model and considering thermally activated transitions. However, since the model assumes that one single atom of the tip is in contact with the substrate, it cannot explain the frictional behavior of sliding systems where multiple tip atoms are in contact with the surface.

One extension of the Tomlinson model is to consider a chain of atoms interacting with each other as well as the substrate as shown in Fig. 3.7 (a). This model is called the Frenkel-Kontorova (FK) model [6] and can be regarded as a model for a single layer of adsorbed atoms. In case the atoms contacting the substrate are constrained by the atoms of the upper layer such as two bulk bodies in contact, we can modify FK model by coupling the atoms in contact to a sliding body as illustrated in Fig. 3.7 (b). The resulting model is known as the Frenkel-Kontorova-Tomlinson (FKT) model [8]. Because FK model can be regarded as a special case of FKT model, we present the main ideas of FKT model below.

In the FKT model, the interaction between the atoms and the interaction between the atoms and the upper body are modeled by harmonic potentials. The interaction between the atoms and the lower body is modeled by a sinusoidal function. The lengths are non-dimensionalized with the lattice parameter of the lower body and the stiffnesses are non-dimensionalized with the stiffness between the atoms.

The resulting potential energy of FKT model is given by

$$\begin{aligned} V(\xi_1,\cdots,\xi_N,x_B) = \frac{1}{2}\sum_{j=1}^{N}(\xi_j-\xi_{j-1})^2 + \frac{\kappa}{2}\sum_{j=1}^{N}\xi_j{}^2 + \frac{b}{2\pi}\sum_{j=1}^{N}\cos[2\pi(x_B + c\,j + \xi_j)] \\ - F\,x_B \quad , \end{aligned} \tag{3-48}$$

where c is the lattice parameter of the upper body; N is the number of lattice points in the upper body; x_B is a reference position of the upper body; ξ_j is the distance of jth atom from the jth lattice point of the upper body; κ is the stiffness of the interaction between the atoms and the upper body; F is a driving force applied to the upper body, and b is the energy barrier of the interaction potential between the atoms and the lower body. Note that when $\kappa = 0$, the FKT model becomes the FK model.

Because the periodic boundary condition ($\xi_{N+1} = \xi_1$) is used, $c \times N$, the number of the wells in the lower interaction potential must be an integer. Thus, if c is a rational number, the system has commensurate surfaces with a periodicity of cN. If c is an irrational number, the periodicity of the model must be infinite and the resulting surfaces are incommensurate.

The model exhibits strong dependence on the commensurability of the surfaces and the magnitude of *b*. For *b*, there are three critical values labeled by b_c^S , b_c^K , and b_c^m which denote the following transitions.

(1) $b < b_c^S$: Static friction is zero.

(2) $b < b_c^K$: Kinetic friction becomes zero as velocity approaches zero. $b > b_c^K$: Finite kinetic friction.

(3) $b < b_c^m$: There is only one stable state. $b > b_c^m$: Metastable states exist depending on the magnitude of *b*.

Moreover, for commensurate surfaces,

$$0 = b_c^S < b_c^K < b_c^m \ , \tag{3-49}$$

and for the incommensurate surfaces,

$$0 < b_c^S = b_c^K = b_c^m \ . \tag{3-50}$$

A simulation study with a finite area of incommensurate interfaces is discussed in Chap. VI.

3.5 Contact Mechanics

In recent AFM experiments performed in the low normal load regime, it is believed that a tip forms a single asperity contact with a surface and the deformation of the tip and the surface is completely elastic [11]. In the single asperity contact, the real contact area is important because we can expect that, according to Bowden and Tabor's theory [12], the following relation holds.

$$F = \tau_S \, A_{real} \ , \tag{3-51}$$

where τ_S is the shear stress at the contact and A_{real} is the real contact area. Using the principles of contact mechanics we can calculate the relationship between the real contact area and the normal load.

When two smooth and non-adhesive spheres are in elastic contact as shown in Fig. 3.8, the Hertzian contact theory gives the radius of the contact area, a, as a function of the applied normal load, F_L,

$$a^3 = \frac{R F_L}{K} \quad , \tag{3-52}$$

$$R = \frac{R_1 R_2}{R_1 + R_2} \quad , \tag{3-53}$$

and

$$K = \frac{4}{3\pi(k_1 + k_2)} \quad , \tag{3-54}$$

where $k_1 = \dfrac{1-v_1^2}{\pi E_1}$ and $k_2 = \dfrac{1-v_2^2}{\pi E_2}$; v is the Poisson's ratio and E is the Young's modulus of each material. Note that the stress inside the contact area is purely compressive and the contact radius a becomes zero when the applied normal load is zero. When a sphere contacts a semi-infinite plane, Eq. (3-52) can still be used with R as the radius of the sphere. Moreover, because there is no adhesion between the two spheres, there is no surface energy and no mechanical work is needed to remove the contact surface.

Now let us consider the contact of adhesive surfaces. Due to the adhesive forces, a contact surface is created by sacrificing the free surfaces of the spheres and the spheres are deformed until the stored elastic energy and the reduced surface energy balance out. In this case, the stress around the edge of the contact area becomes tensile and the stress around the center becomes compressive. Moreover, some mechanical work will be needed to separate the two spheres and remove the contact surface.

If we assume that the adhesive forces act only inside the contact area, the analytical expression for the relationship between the contact radius and the normal force is given by the Johnson-Kendall-Roberts (FKR) theory [13],

$$a^3 = \frac{R}{K}(F_L + 3\gamma\pi R + \sqrt{6\gamma\pi R F_L + (3\gamma\pi R)^2}\ ) \ , \tag{3-55}$$

where γ is the surface energy per unit area.

On the contrary, the Derjaguin-Muller-Toporov (DMT) theory [14] assumes that the adhesive forces are dominant outside the contact area and the Hertzian deformed contact profile is not changed inside the contact area. In this theory, the contact radius is given by

$$a^3 = \frac{R}{K}(F_L + 2\gamma\pi R) \ . \tag{3-56}$$

In the modeling of AFM systems using molecular dynamics, we cannot deal with a surface with an infinite depth. Thus, we need to determine the deformation range inside a surface pressed by an AFM tip to determine a proper depth of the simulated surface. The penetration depth can give an estimate to this. Using the JKR theory, the penetration depth of a sphere from the original height of a semi-infinite surface, δ, is given by

$$\delta = \frac{a^2}{R} - \left(\frac{8\pi\gamma a}{3K}\right)^{1/2} \ . \tag{3-57}$$

Therefore, we can expect that substrates in MD simulations should have depths of at least $2 \sim 3\,\delta$.

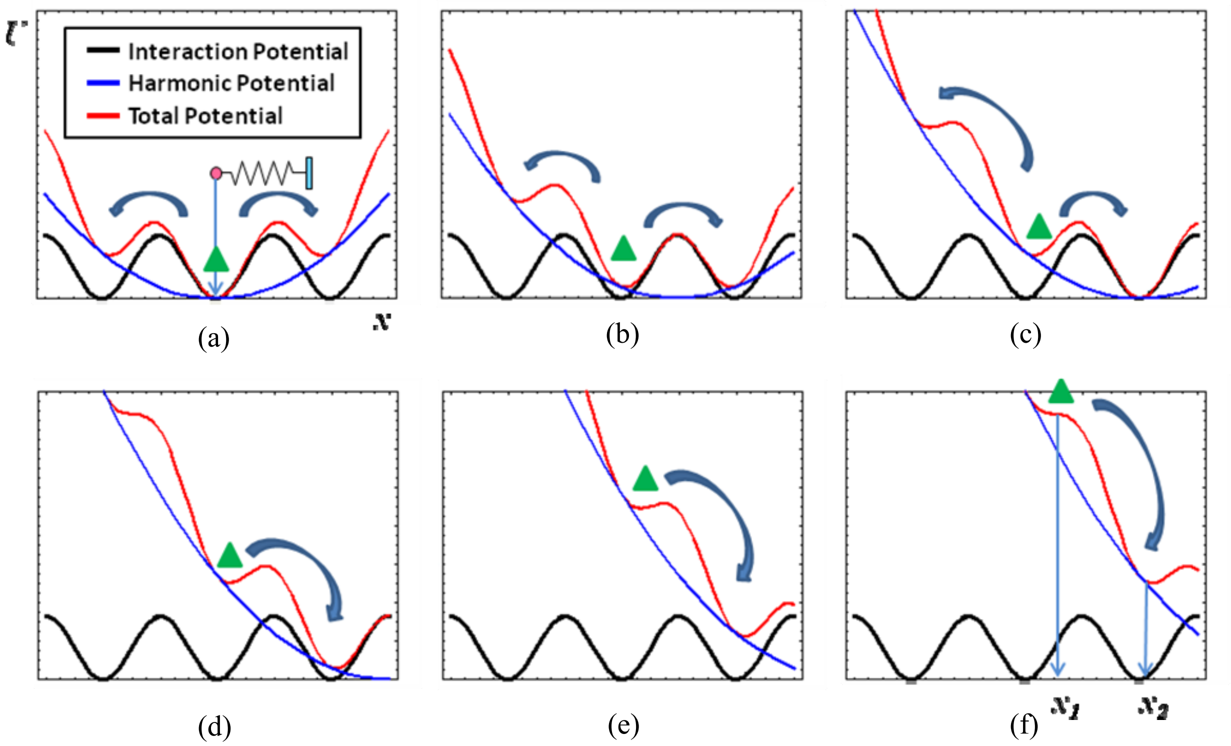

(a) (b) (c)

(d) (e) (f)

Figure 3.1 Potential energy curves at different slider positions, illustrating the Tomlinson model. As the slider advances to the right, the harmonic potential (blue) shifts and the total potential (red) changes. The green triangles indicate the initial minimum.

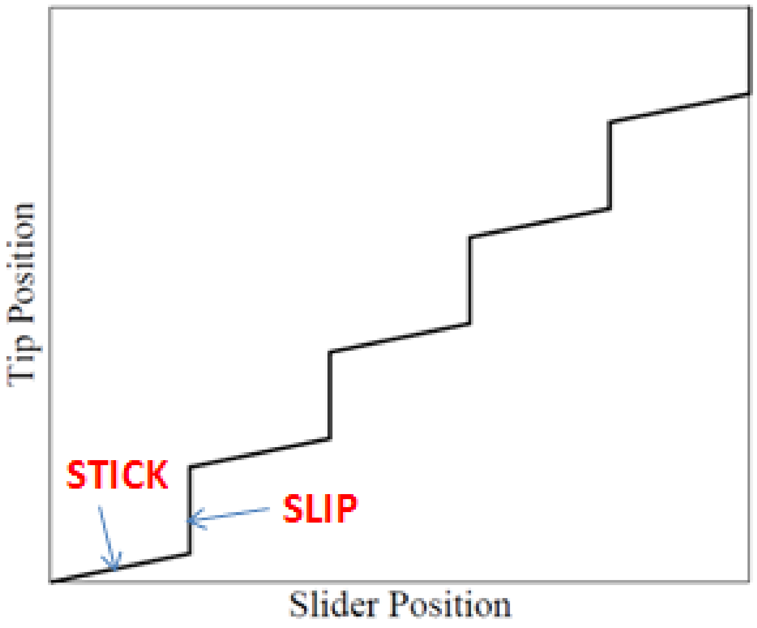

(a)

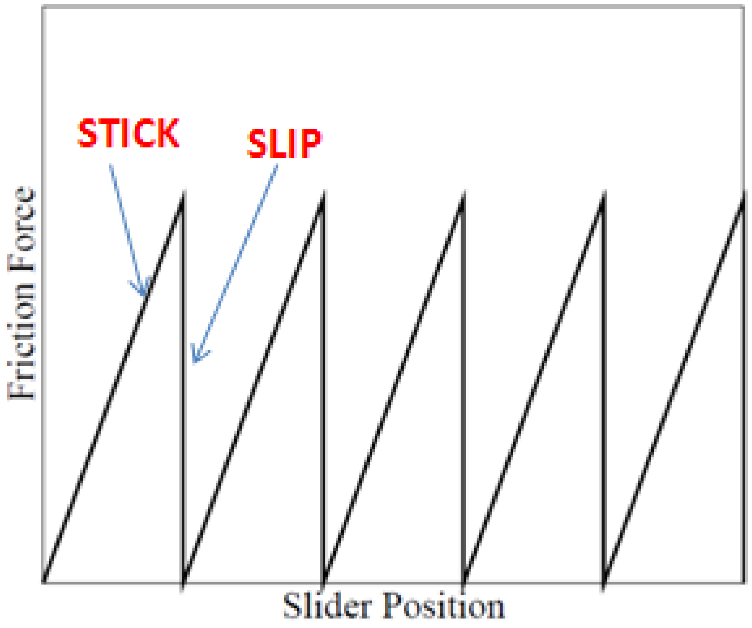

(b)

Figure 3.2 Typical behaviors in the stick-slip motion. (a) Tip position vs. slider position; (b) Friction Force vs. slider position.

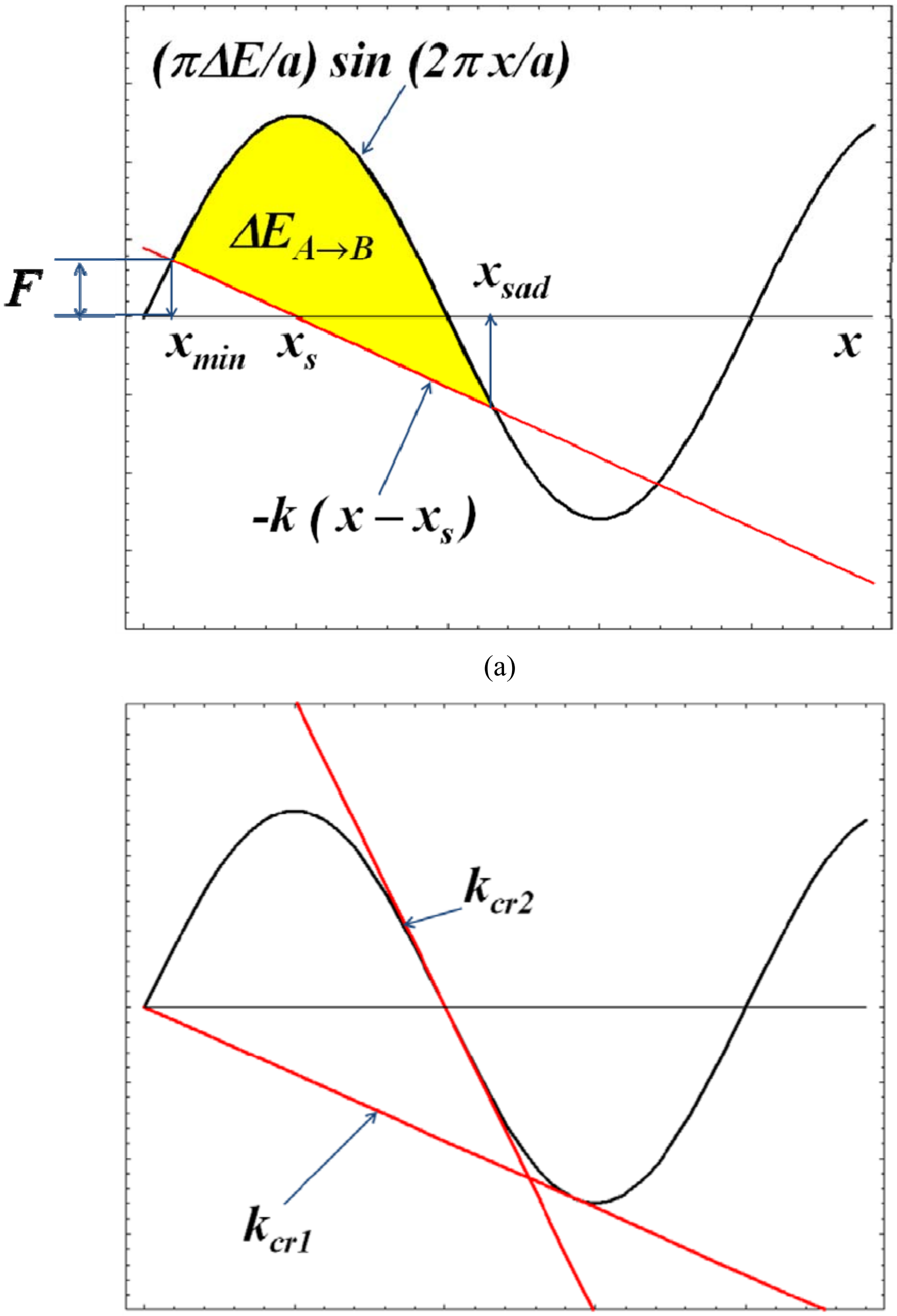

(a)

(b)

Figure 3.3 Illustration of the graphical methods to find the solutions of the Tomlinson model at zero temperature. (a) $x_{\min}$ and x_{sad} indicate the minimum and the saddle point respectively, and the yellow area corresponds to the instantaneous energy barrier, $\Delta E_{A\rightarrow B}$ and $F = k(x_S - x_{\min})$ (b) when $k > k_{cr1}$ initially there is only one well, but as the slider moves new wells appear. When $k > k_{cr2}$ there is always only one well.

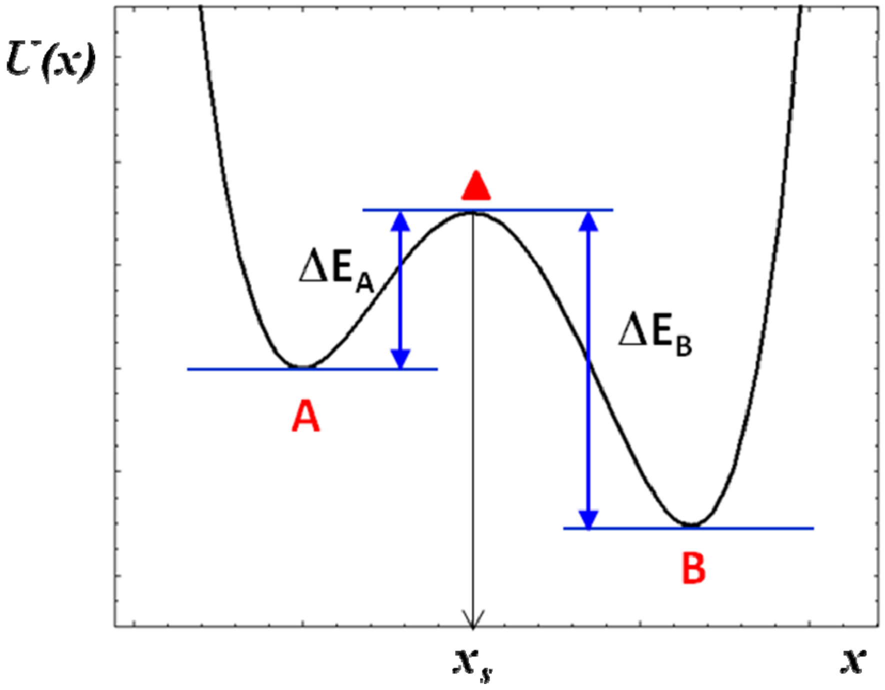

Figure 3.4 A potential energy curve with two wells. The red triangle indicates the saddle point.

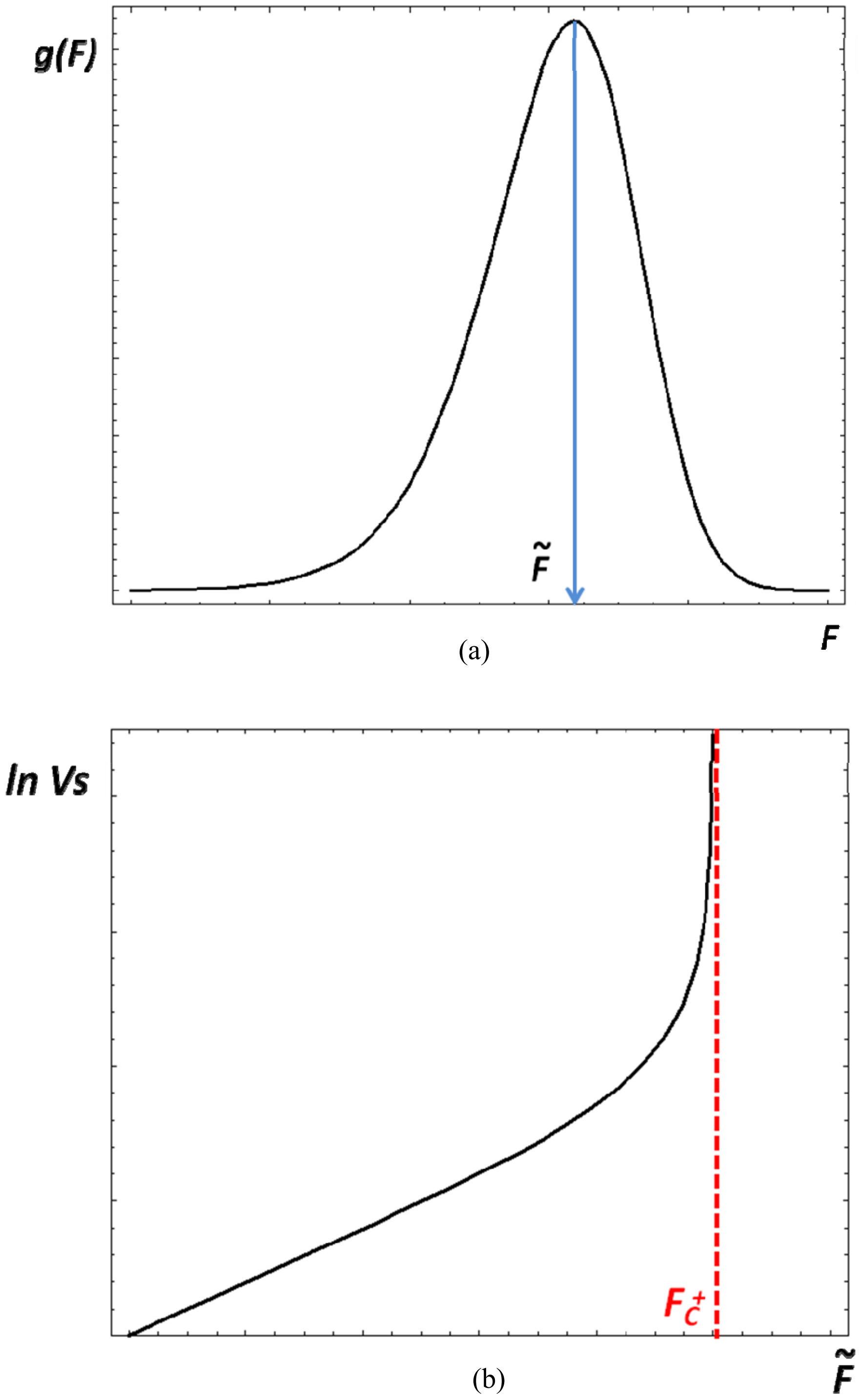

(a)

(b)

Figure 3.5 Illustrations of (a) the distribution of the force at the transition and (b) the sliding velocity dependence of the most probable transition force.

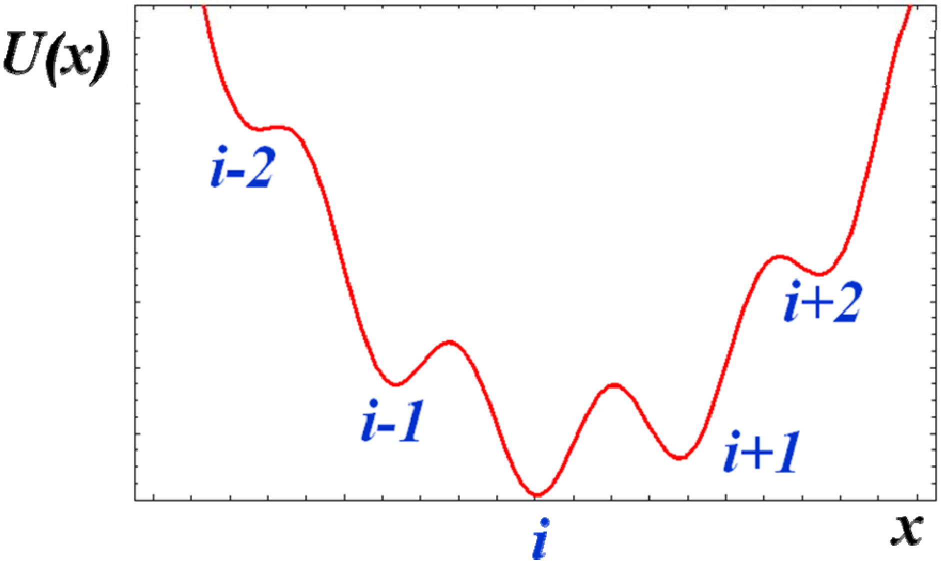

Figure 3.6 A diagram of the total energy *U(x)* as a function of the tip position *x*. The minima are labeled by ascending indices from the left to the right.

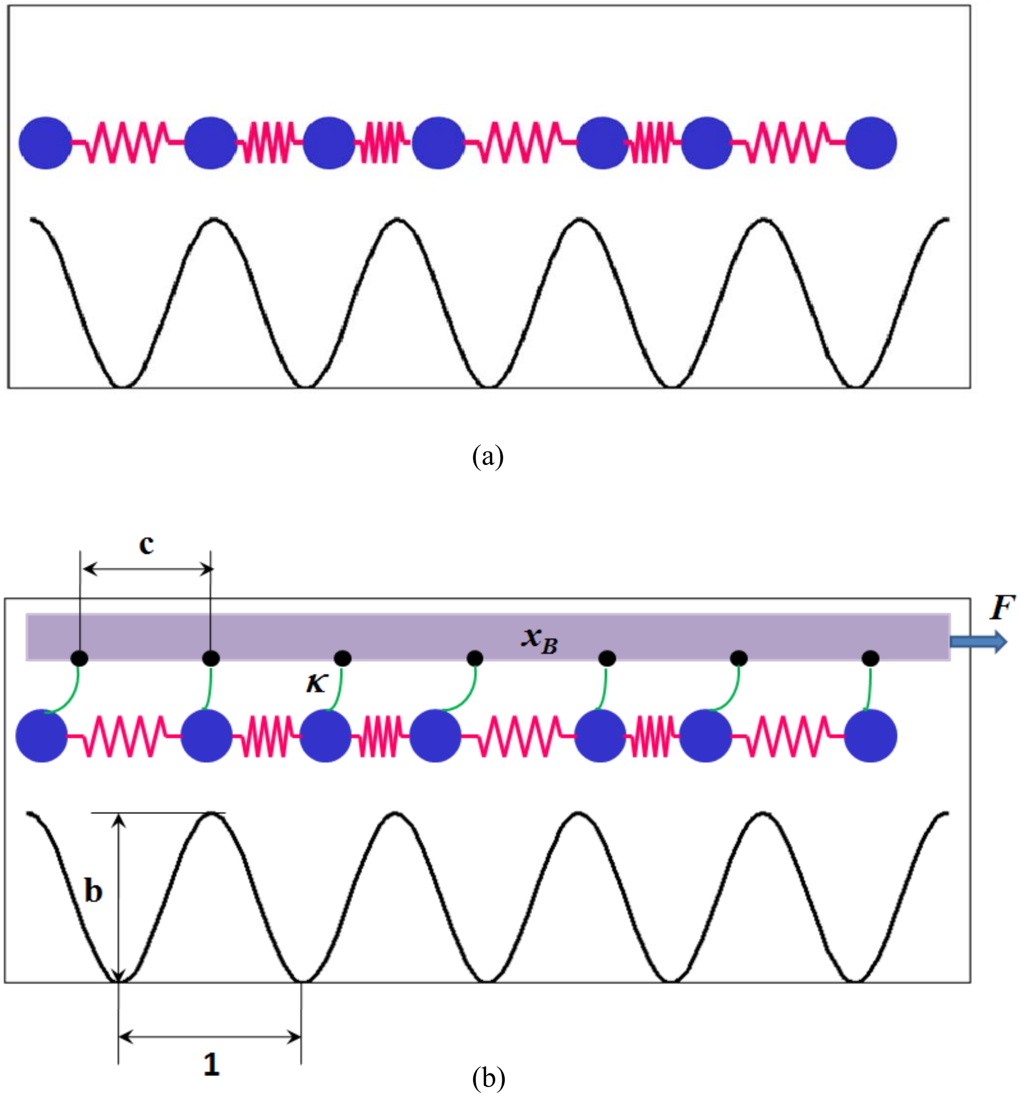

(a)

(b)

Figure 3.7 Illustrations of friction models. (a) Frenkel-Kontorova model and (b) Frenkel-Kontorova-Tomlinson model.

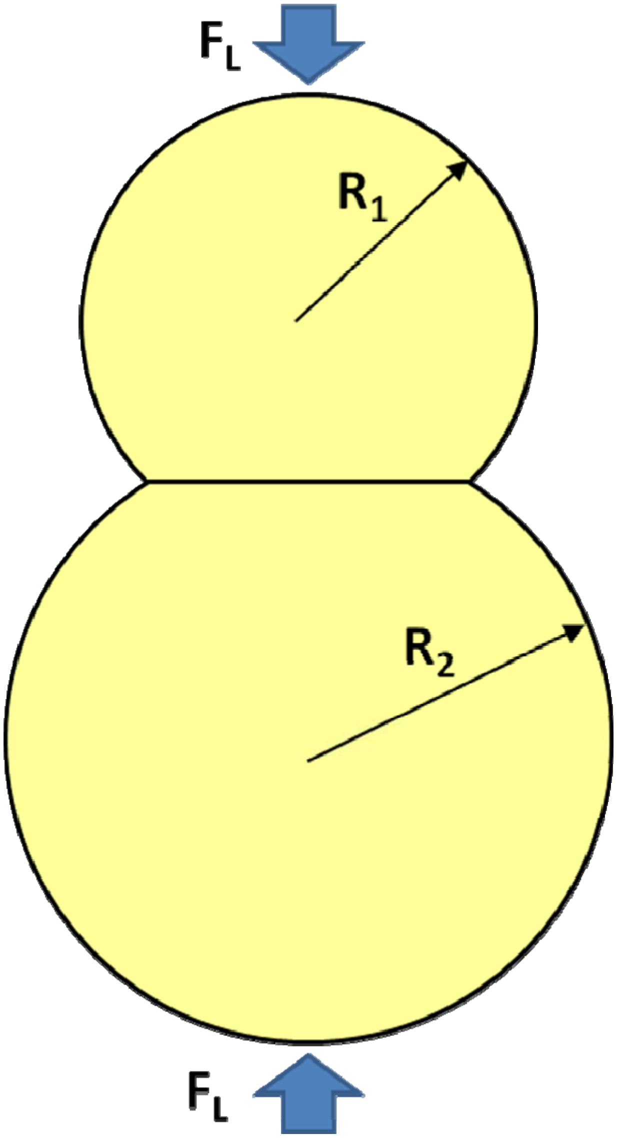

Figure 3.8 A diagram of two elastic spheres contacting each other.

References

[1] G. A. Tomlinson, “*A Molecular Theory of Friction*”, Philos. Mag., 7, 905 (1929).

[2] E. Gnecco, R. Bennewitz, T. Gyalog, Ch. Loppacher, M. Bammerlin, E. Meyer, and H.-J. Güntherodt, “*Velocity Dependence of Atomic Friction*”, Phys. Rev. Lett., 84, 1172 (2000).

[3] Y. Sang, M. Dube, and M. Grant, “*Thermal Effects on Atomic Friction*”, Phys. Rev. Lett., 87, 174301 (2001).

[4] E. Riedo, E. Gnecco, R. Bennewitz, E. Meyer, and H. Brune, “*Interaction Potential and Hopping Dynamics Governing Sliding Friction*”, Phys. Rev. Lett., 91, 084502 (2003).

[5] S. Y. Krylov, K. B. Jinesh, H. Valk, M. Dienwiebel, and J. W. M. Frenken, “*Thermally Induced Suppression of Friction at the Atomic Scale*”, Phys. Rev. E, 71, 065101 (2005).

[6] J. Frenkel and T. Kontorova, “*On the Theory of Plastic Deformation and Twinning*”, J. Phys. (USSR), 1, 137 (1939).

[7] O. M. Braun, T. Dauxois, M. V. Paliy, and M. Peyrard, “*Nonlinear Mobility of the Generalized Frenkel-Kontorova Model*”, Phys. Rev. E, 55, 3598 (1997).

[8] M. Weiss and F.-J. Elmer, “*Dry Friction in the Frenkel-Kontorova-Tomlinson Model: Static Properties*”, Phys. Rev. B, 61, 2335 (2000).

[9] A. Socoliuc, R. Bennewitz, E. Gnecco, and E. Meyer, “*Transition from Stick-Slip to Continuous Sliding in Atomic Friction: Entering a New Regime of Ultralow Friction*”, Phys. Rev. Lett., 92, 134301 (2004).

[10] C. E. Maloney and D. J. Lacks, “*Energy Barrier Scalings in Driven Systems*”, Phys. Rev. E, 73, 061106 (2006).

[11] R. W. Carpick, and M. Salmeron, “*Scratching the Surface: Fundamental Investigations of Tribology with Atomic Force Microscopy*”, Chem. Rev., 97, 1163 (1997).

[12] F. P. Bowden and D. Tabor, *The Friction and Lubrication of Solids* (1958).

[13] K. L. Johnson, K. Kendall, and A. D. Roberts, “*Surface Energy and the Contact of Elastic Solid*”, P. Roy. Soc. Lond. A Mat., 324, 301 (1971).

[14] B. V. Derjaguin, V. M. Muller, and Y. P. Toporov, “*Effect of Contact Deformations on Adhesion of Particles*”, J. Colloid Interf. Sci., 53, 314 (1975).

CHAPTER IV

Hyperdynamics

4.1 Introduction

As discussed in chapter II, we have two major methodologies for dynamical systems. One is the KMC method and the other is the MD method. KMC can access much longer time scales than MD by several orders of magnitude, but transition mechanisms and rates should be known *a priori*. In the MD simulation, a system evolves naturally without requiring any prior information about the transition modes the system will take when making transitions. However, it has not been possible to perform MD simulations longer than microseconds. An ideal solution would allow us to perform dynamics simulations on time scales reachable by KMC.

About a decade ago, Voter proposed a novel method to extend the MD time-scale, now called hyperdynamics [1]. In hyperdynamics, a given potential energy function is modified such that the energy barriers are reduced while the characteristic dynamics are preserved. In principle hyperdynamics simulation can advance the system at an accelerated pace while preserving the correct relative transition probabilities. Furthermore, the acceleration rate can be calculated concurrently during the simulation.

The subsequent sections present a systematic review of the hyperdynamics method. Sec. 4.2 presents a general review of hyperdynamics, and critical issues are discussed in Sec. 4.3. Finally, the modifications of the original hyperdynamics method and a parallel algorithm for an externally driven system are described in Sec. 4.4.

4.2 General Review

Let us consider a simple two-dimensional system, i.e., the potential energy of the system has two independent variables. As shown in Fig. 4.1, the potential has four minima, labeled by A, B, C, D, respectively, and initially the system resides in the state A, which has three adjacent states (B, C, D). We assume that there is a surface (a curve in a two-dimensional case) S completely surrounding the state A and the surface can be divided into three parts ($S = S_B \cup S_C \cup S_D$) such that whenever the system crosses one of them, it “hops” to the corresponding state (i.e. if the system crosses S_B, it equilibrates in B).

As expressed in Eq. (2-15), the TST rate constant for transition from the state A to one of its neighboring states (e.g. B) is given by

$$R_{A\to B}^{TST} = \frac{1}{2}\frac{\int_{S_B} dS \int d\vec{v}\, |v_n|\, e^{-V/k_BT} e^{-K/k_BT}}{\int_A d\vec{r} \int d\vec{v}\, e^{-V/k_BT} e^{-K/k_BT}} \quad , \tag{4-1}$$

and the total escape rate from A is the sum of the individual rates such that

$$R_A^{TST} = R_{A\to B}^{TST} + R_{A\to C}^{TST} + R_{A\to D}^{TST} = \frac{1}{2}\frac{\int_S dS \int d\vec{v}\, |v_n|\, e^{-V/k_BT} e^{-K/k_BT}}{\int_A d\vec{r} \int d\vec{v}\, e^{-V/k_BT} e^{-K/k_BT}} \tag{4-2}$$

Using Eq. (2-10) and Eq. (4-1), we can also calculate the relative probabilities. Thus,

$$\frac{p_{A\to C}}{p_{A\to B}} = \frac{R^{TST}_{A\to C}}{R^{TST}_{A\to B}} = \frac{\int_{S_C} dS \int d\vec{v}\, |v_n|\, e^{-V/k_BT} e^{-K/k_BT}}{\int_{S_B} dS \int d\vec{v}\, |v_n|\, e^{-V/k_BT} e^{-K/k_BT}} \quad , \tag{4-3}$$

Note that this ratio depends on the potential energy values at the surfaces only.

Now, our goal is to increase the overall escape rate, R_A^{TST}, which is the same as the inverse of the average waiting time $(R_A = 1/\bar{t}_A)$ while preserving the relative transition probabilities shown in Eq. (4-3). Voter's idea was to use a modified potential energy function instead of the original potential to accomplish this goal [1]. The modified potential is obtained by adding a bias potential, $\Delta V(\vec{r})$, which has positive values in A, surrounded by *S*, and zero along the dividing surface *S*. Thus, the modified potential and the bias potential are

$$V_b(\vec{r}) = V(\vec{r}) + \Delta V(\vec{r}) \quad , \tag{4-4}$$

$$\Delta V(\vec{r}) = \begin{cases} > 0\,, & in\ A \\ = 0\,, & along\ S \end{cases} \quad . \tag{4-5}$$

Fig. 4.2 shows the original potential and the biased potential together, which are plotted along the dashed line in Fig. 4.1, illustrating how the potential energy changes after it is biased by ΔV; the energy barrier between A and B is reduced, but the original potential is not modified at the saddle point.

The rate constant in the modified potential energy, V_b, becomes

$$\left(R_A^{TST}\right)_b = \frac{1}{2} \frac{\int_S dS \int d\vec{v}\, |v_n|\, e^{-V_b/k_BT} e^{-K/k_BT}}{\int_A d\vec{r} e^{-V_b/k_BT} e^{-K/k_BT}} \quad . \tag{4-6}$$

Knowing that the modified potential has the same values at the dividing surface as the original potential, the ratio of the average waiting times in both potentials, denoted by β, can be obtained by

$$\beta = \frac{\bar{t}_A}{\left(\bar{t}_A\right)_b} = \frac{\left(R_A^{TST}\right)_b}{R_A^{TST}} = \frac{\int_A d\vec{r}\; e^{-V/k_BT}}{\int_A d\vec{r}\; e^{-V_b/k_BT}} \quad . \tag{4-7}$$

Because V_b is larger than V in A, β is always larger than 1 and the average waiting time in the modified potential becomes shorter than the average waiting time in the original potential. By manipulating Eq. (4-7), we can derive two means of calculating the boost factor,

$$\beta = \left\langle e^{+\Delta V/k_BT} \right\rangle_b = \frac{\int_A d\vec{r}\; e^{+\Delta V/k_BT} e^{-V_b/k_BT}}{\int_A d\vec{r}\; e^{-V_b/k_BT}} \quad , \tag{4-8-a}$$

and

$$\beta = \frac{1}{\left\langle e^{-\Delta V/k_BT} \right\rangle} = \frac{\int_A d\vec{r}\; e^{-V/k_BT}}{\int_A d\vec{r}\; e^{-\Delta V/k_BT} e^{-V/k_BT}} \quad . \tag{4-8-b}$$

Thus, the boost factor obtained in hyperdynamics can be calculated from either the thermodynamic average of $e^{+\Delta V/k_BT}$ in the biased potential or the inverse of the average of $e^{-\Delta V/k_BT}$ in the original potential. Note that the boost factor is easier to calculate using either Monte Carlo (MC) Method or MD than the transition rate as in Eq. (2-15) or Eq. (4-1) because the boost factor is less dependent on the potential energy values at the dividing surface, which is rarely visited.

Moreover, the relative transition probability in the biased potential is given by

$$\frac{p_{A\to C}}{p_{A\to B}} = \frac{\left(R^{TST}_{A\to C}\right)_b}{\left(R^{TST}_{A\to B}\right)_b} = \frac{\int_{S_C} dS \int d\vec{v}\,|v_n|\, e^{-V_b/k_BT} e^{-K/k_BT}}{\int_{S_B} dS \int d\vec{v}\,|v_n|\, e^{-V_b/k_BT} e^{-K/k_BT}}$$

$$= \frac{\int_{S_C} dS \int d\vec{v}\,|v_n|\, e^{-V/k_BT} e^{-K/k_BT}}{\int_{S_B} dS \int d\vec{v}\,|v_n|\, e^{-V/k_BT} e^{-K/k_BT}} = \frac{R^{TST}_{A\to C}}{R^{TST}_{A\to B}} \quad , \qquad (4\text{-}9)$$

which is the same as the relative transition probability in the original potential.

Therefore, the system in the biased potential will evolve following the same stochastic sequence of states as in the original potential, but at an accelerated pace.

4.3 Critical issues

4.3.1. The Boost Factor

According to Voter's guide [1], the time t in the original potential can be recovered from the time t_b elapsed in the potential V_b modified with a bias potential ΔV using

$$t = \sum_{i=1}^{N_{TOT}} \Delta t_{MD}\, e^{+\Delta V[\vec{r}(t_i)]/k_BT} \quad , \qquad (4\text{-}10)$$

where N_{TOT} is the total number of MD steps, Δt_{MD} is the time interval for numerical integration, and t_i is the time at *i*th MD step ($= i \times \Delta t_{MD}$). To verify Eq. (4-10), let us imagine that we are repeating a simulation starting in the same initial state many times to measure a waiting time for the same transition event in the unbiased potential. At each trial, the outcome will vary, but the distribution of the outcomes will converge to a definite distribution, given by

$$p(t) = R \exp(-Rt) \quad , \qquad (4\text{-}11)$$

where R is the rate constant in the original potential. If we perform the same procedure with the biased potential, we will have another distribution of a form of Eq. (4-11), but in this case the rate constant will be different.

$$p(t_b) = R_b \exp(-R_b t_b) \quad , \tag{4-12}$$

where R_b is the rate constant in the biased potential. If we assume that we can use the TST approximation for the actual rates, the relationship between these two rate constants can be given by the boost factor β, as in Eq. (4-7),

$$\beta = \frac{R_b}{R} \quad . \tag{4-13}$$

Now let us consider a distribution of a variable ξ, called a recovered time, obtained by multiplying the waiting time in the biased potential, t_b, by the boost factor β. It can be shown that the distribution of the recovered time ξ ($= t_b \times \beta$) is identical to the distribution of the waiting time in the original potential, using the following derivation

$$\begin{aligned} p(\xi) &= \frac{d\,t_b}{d\xi}\, p(t_b) \\ &= \frac{1}{\beta}\, p(t_b) && \text{from } \frac{d\,t_b}{d\xi} = \frac{1}{\beta} \\ &= \frac{R_b}{\beta} \exp(\frac{R_b}{\beta}\,\xi) && \text{from Eq. (4-12)} \\ &= R \exp(R\,\xi) && \text{from Eq. (4-13)}\ . \end{aligned}$$

Therefore, the stochastic outcome of the waiting time in the original potential can be replaced by the recovered time.

Now return to Eq. (4-10) and consider a single transition event simulated with MD. We can regard this MD simulation as a sampling to obtain the ensemble average in Eq. (4-8-a). Then, Eq. (4-8-a) can be obtained by

$$\beta = \frac{\sum_{i=1}^{N_{TOT}} e^{+\Delta V[\vec{r}(t_i)]/k_B T}}{N_{TOT}} \ . \tag{4-14}$$

Note that the MD simulation should be performed with the biased potential, i.e., the force vector should be obtained from the biased potential, in order to calculate β using Eq. (4-8-a). Since the recovered time can be regarded as the original waiting time, we have

$$\begin{aligned} t &= \xi = t_b \times \beta \\ &= N_{TOT} \times \Delta t_{MD} \times \beta && \text{from } t_b = N_{TOT} \times \Delta t_{MD} \\ &= \sum_{i=1}^{N_{TOT}} \Delta t_{MD}\, e^{+\Delta V[\vec{r}(t_i)]/k_B T} && \text{from Eq. (4-14).} \end{aligned}$$

This agrees with the supposition in Eq. (4-10).

In the above derivation it is assumed that Eq. (4-14) holds, an assumption that largely depends on the total number of MD steps sampled in each escape event. If a bias potential is chosen too aggressively, the system will stay in the starting state for a short time and hop to other states soon. Then, there will be too small a number of MD steps to obtain β accurately. With an inaccurate β , the recovered time ξ loses its statistical meaning and its ability to approximate the original time. In an optimistic view expressed in [1], even with the aggressive choice, the accumulated time error after many transitions may vanish because the time error in each escape is not correlated with others. However, it is also likely that a bad choice of a bias potential can cause the time error in a biased way such that it always yields shorten estimations or lengthen estimations at every transition.

Thus, we propose to use Eq. (4-8-b) to calculate the boost factor in case of aggressive boosting rather than Eq. (4-8-a). Then, β is approximated by

$$\beta = \frac{N_{TOT}}{\sum_{i=1}^{N_{TOT}} e^{-\Delta V[\vec{r}(t_i)]/k_B T}} \quad . \tag{4-15}$$

This requires a pre-simulation using the original, unbiased potential before we launch the boosted simulation. Because this process requires extra computation, a trade-off arises between the choice of an aggressive bias potential with the boost factor obtained from Eq. (4-15) that requires pre-computation and a safe bias potential with the boost factor from Eq. (4-10) that does not.

The major advantage of this pre-computation is that once we perform a MD simulation with the original potential in a sufficient number of MD steps to accurately obtain the ensemble average in Eq. (4-8-b), we can adjust parameters in the form of a bias potential to maximize the boost factor. We do not need to run the simulation again when we modify the parameters because Eq. (4-8-b) is based on the original potential, which does not depend on the parameters of the bias potential. On the contrary, if we used Eq. (4-8-a), we would have to re-run the MD simulation with the biased potential whenever we modified the parameters. Moreover, the information obtained from the pre-simulation can be used to find the maximum allowed boost factor of a given bias potential using a local variable. To verify this, let us consider a bias potential which is defined by a local variable λ such that $\Delta V = \Delta V(\lambda)$ such that it vanishes when $\lambda < \lambda_{CR}$. Then, the boost factor is given by

$$\beta = \frac{1}{\left\langle e^{-\Delta V / k_B T} \right\rangle} = \frac{1}{\int_{\lambda} p(\lambda)\, e^{-\Delta V(\lambda)/k_B T} d\lambda} \quad , \tag{4-16}$$

and the maximum boost factor can be found by

$$\begin{aligned}\beta &= \frac{1}{\int_{\lambda<\lambda_{CR}} p(\lambda)\, e^{-\Delta V(\lambda)/k_B T} d\lambda + \int_{\lambda\geq\lambda_{CR}} p(\lambda)\, e^{-\Delta V(\lambda)/k_B T} d\lambda} \\ &= \frac{1}{p(\lambda<\lambda_{CR}) + \int_{\lambda\geq\lambda_{CR}} p(\lambda)\, e^{-\Delta V(\lambda)/k_B T} d\lambda} \leq \frac{1}{p(\lambda<\lambda_{CR})} \quad ,\end{aligned} \tag{4-17}$$

where $p(\lambda)$ is the probability density of λ in the original potential. Therefore, the boost factor cannot be larger than the inverse of the probability that $\lambda < \lambda_{CR}$ in each state. For example, if we use the lowest eigenvalue of the Hessian matrix as the local variable and set zero as the critical value, the maximum achievable boost factor is limited to the ratio of the phase space volume of the unboosted region, where the lowest eigenvalue of the Hessian matrix is negative, to that of the entire basin.

4.3.2 Various Bias Potentials

As shown in Sec. 4.2, a bias potential $\Delta V(\vec{r})$ must be constructed to implement hyperdynamics. In addition to satisfying Eq. (4-5), a proper bias potential should not introduce new barriers inside a state whose waiting times compete with the original one [1]. Moreover, the bias potential should not result in significant computational overhead exceeding the boost factor obtainable with the modified potential.

To successfully create a bias potential, we first need to identify a criterion for identifying the dividing surface because a bias potential should be zero at the surface. As discussed in Sec. 2.3, the dividing surface can be achieved either by minimizing Eq. (2-

19) or by finding all the first-order saddle points. However, it is much more practical to define a bias potential based on local properties of a given potential energy surface, defined at a point $\vec{r}$ in the configuration space. Candidates for such local properties include the potential energy $V(\vec{r})$, the gradient $\nabla V(\vec{r})$, and the Hessian $H_{ij} (= \partial^2 V / \partial r_i \partial r_j)$, but may include other properties of the system energy or configuration.

In [1] and [2], Voter used the lowest eigenvalues and corresponding eigenvectors of the Hessian to construct a bias potential, using the definition of an approximate dividing surface proposed by Sevick *et. al.* [3]. The bias potential energy has the form [2],

$$\Delta V(\vec{r}) = \frac{A_1}{2}\left[1 + \frac{\varepsilon_1}{\sqrt{\varepsilon_1^2 + (g_{1p} / A_2)^2}}\right], \tag{4-18}$$

where A_1 and A_2 are parameters, ε_1 is the lowest eigenvalue, and $g_{1p} = \vec{C}_1 \cdot \nabla V$, where $\vec{C}_1$ is the corresponding eigenvector to ε_1. Note that Eq. (4-18) vanishes when the condition Eq. (2-31) is satisfied. One of the most difficult barriers for implementing this bias potential is calculating the lowest eigenvalue. Furthermore, calculating boost forces requires its derivative, which is related to the third derivative of the potential. In [2], Voter presented an alternative method to approximate the lowest eigenvalue and its derivative and the method requires only first derivatives. Because the eigenvalues of the Hessian are the second derivatives of the potential along the direction of eigenvectors, the lowest eigenvalue can be obtained by finding a direction minimizing the second derivative of the Hessian. Moreover, instead of using the exact second derivative, he minimized the finite difference form for it, given by

$$\kappa(\vec{c}) = \frac{V(\vec{r} + h\,\vec{c}) - 2\,V(\vec{r}) + V(\vec{r} - h\,\vec{c})}{h^2} \quad , \tag{4-19}$$

where $\kappa(\vec{c})$ is the approximate second derivative along a direction vector $\vec{c}$, and h is the interval for the finite difference scheme. Thus, the approximate value for the lowest eigenvalue, ε_{appx} , is obtained by finding the direction minimizing $\kappa(\vec{c})$.

$$\varepsilon_{appx} = \min[\kappa(\vec{c})] \quad . \tag{4-20}$$

Then, the derivative of ε_{app} is given by

$$\frac{\partial \varepsilon_{appx}}{\partial \vec{r}} = \left[\frac{\vec{g}\,(\vec{r} + h\,\vec{c}_{\min}) - 2\,\vec{g}\,(\vec{r}) + \vec{g}\,(\vec{r} - h\,\vec{c}_{\min})}{h^2} \right] \quad , \tag{4-21}$$

where $\vec{g}$ is the gradient ($= \nabla V$), and $\vec{c}_{\min}$ is the direction along which Eq. (4-20) is minimized. Note that Eq. (4-21) is the exact derivative for Eq. (4-20). Another tricky part in this bias potential is to obtain the derivative of g_{1p} . In [2], Voter proposed a method, called the lambda method, to approximate g_{1p} and its derivative, but the method requires two additional minimizations and the derivative is obtained by the difference between two minimized quantities, which is difficult to obtain high accuracy with a reasonable computational load. In our implantation, when we calculate the lowest eigenvalue we use a Lanczos iterative method [4], which is more efficient than the Voter's minimization method. After the eigenvalue and eigenvector are found, the derivative of the eigenvalue is obtained by Eq. (4-21).

While Voter's method is well motivated, it is very expensive and therefore we need to examine other implementations. One of the simplest bias potential was the one proposed by Steiner *et. al.* [5]. In their method, a constant energy value E_B is chosen and whenever the original potential becomes less than E_B, the modified potential, which is the sum of the original potential and a bias potential, have this value. When the original potential becomes larger than E_B, the bias potential becomes zero so that the modified potential has the same value as the original one. Thus, their bias potential is

$$\Delta V(\vec{r}) = \begin{cases} = \quad 0, & when \;\; V(\vec{r}) > E_B \\ = E_B - V, & when \;\; V(\vec{r}) \leq E_B \end{cases} . \tag{4-22}$$

For this method, E_B must be chosen as a value lower than the lowest saddle point energy and it is difficult to verify whether or not this is truly satisfied. Moreover, it is possible, particularly for complex energy landscapes, that when the condition is satisfied, the boost factor obtained by the bias potential is very small.

Recently, a more reasonable bias potential without significant computational overhead, called the bond-boost method, was proposed by Miron and Fichthorn [6]. The bond-boost method utilizes the characteristic of bond-breaking that most solid-state systems experience when making transitions. If we compare the configurations before and after a transition, the bond lengths of atom pairs in the system become different. By introducing the fractional bond length change of a bond, e_k, defined below and assuming there is a threshold q such that $e_{\max} > q$ after crossing a dividing surface, a bias potential can be defined by .

$$\Delta V = \Delta V(\, e_1, e_2, \cdots) = A(e_{\max}) \sum_{k=1}^{N_b} \delta V(e_k) \;\; , \tag{4-23}$$

and

$$e_k = \left| \frac{l_k - l_k^{ref}}{l_k^{ref}} \right| \;\; , \tag{4-24}$$

where l_k is a bond length of *k*th bond; l_k^{ref} is a reference bond length defined at the minimum configuration; N_b is the total number of bonds, and A is an envelope function defined below. δV is a boost energy defined as

$$\delta V(e_k) = \begin{cases} > 0\,, & when\ e_k \le q \\ = 0\,, & when\ e_k > q \end{cases} \quad . \tag{4-25}$$

Thus, as e_k approaches *q*, δV decreases, and when e_k exceeds the limit *q*, δV vanishes. The threshold parameter *q* can be determined by an empirical simulation, and by choosing *q* conservatively, we can make the bias potential vanish before the system reach the dividing surface. Because the bond length changes depend on the reference configuration, when a transition is detected, a new reference configuration needs to be defined. After a transition is detected and some equilibration time has elapsed, the new reference configuration is found by minimizing the potential energy. In addition to this, it is required that the overall bias energy ΔV must vanish when the maximum fractional bond length change $e_{\max}$ crosses the limit. An envelope function A, which is a function of $e_{\max}$ only, is introduced for this purpose. One common choice is

$$A(e_{\max}) = \begin{cases} = 1\,, & when\ e_{\max} \le q \\ = 0\,, & when\ e_{\max} > q \end{cases} \quad . \tag{4-26}$$

Thus, ΔV vanishes when $e_{\max} > q$. However, using an envelope function causes a significant side effect to the method [6]. There is an extra force component due to the bias potential which is applied only to the bond experiencing the maximum length change. This extra force component is much larger than other bias force components, and when the maximum bond pair switches, the biased force of the old maximum pair suddenly disappears and the biased force of the new maximum pair appears, i.e., the force field due to the bias potential of the bond-boost method is discontinuous.

Another shortcoming of the bond-boost method is illustrated in Fig. 4.3. The blue curves in the figure represent the original pair interactions where bias potentials of the bond-boost method (shown as red curves) are added to result in biased potentials (cyan curves). Since the reference bond length is determined from the minimum configuration of the entire collection of atoms, it is different from the equilibrium position of the single pair interaction as shown in Fig. 4.3 (a). Depending on how far the reference position is from the equilibrium position, a bias potential can introduce a double-well into the pair interaction, which is physically unrealistic. The double-well also makes the hyperdynamics simulation very inefficient because when the atoms in the pair with the double-well are located on the farther of the two equilibrium positions, the bond length changes remains large most of the time without undergoing any transitions. Thus, the boost factor remains very small. Moreover, when a transition occurs by the formation of new bonds, the bond-boost method may not detect this mechanism because a bias potential of the bond-boost method cannot be added to an unbound pair, because it always creates a double well under these circumstances as shown in Fig. 4.3 (b).

As discussed above, several bias potentials have been proposed thus far, but some have significant computational overhead, which degrades an achieved boost factor, and others lack the generality required to detect every transition. Thus, finding a new bias potential that gives much larger boosting without significant extra computation remains a challenging problem.

4.3.3. General Procedure to Construct a Bias Potential, Using Local Variables

Like the lowest eigenvalue of the Hessian, it is desirable to use local variables for a bias potential, but to calculate eigenvalues requires significant computational overhead. Thus, identifying another local variable to approximate a dividing surface is a priority. In this section, we first present a general procedure to define a bias potential using a local variable, and then several other local variables are discussed.

Let us assume that there is a variable λ that is a function of position $\vec{r}$ and at a dividing surface, either the upper bound of λ, λ_{up}, or the lower bound λ_{low} is known. For example, it seems that the lowest eigenvalue has the upper bound of zero at a dividing surface. If λ has the upper bound λ_{up}, then λ should go below λ_{up} when the system crosses the dividing surface and λ can be used to define a bias potential in the following way:

$$\Delta V[\lambda(\vec{r})] = \begin{cases} > 0 \ , & when \ \ \lambda(\vec{r}) > \lambda_{up} \\ = 0 \ , & when \ \ \lambda(\vec{r}) \le \lambda_{up} \end{cases} , \tag{4-27}$$

$$\Delta \vec{F}[\lambda(\vec{r})] = \begin{cases} = \ -\dfrac{\partial \Delta V}{\partial \lambda}\dfrac{\partial \lambda}{\partial \vec{r}} \ , & when \ \ \lambda(\vec{r}) > \lambda_{up} \\ = \qquad 0 \ , & when \ \ \lambda(\vec{r}) \le \lambda_{up} \end{cases} . \tag{4-28}$$

Let's consider a number of local variables that could be used in place of or in addition to the lowest eigenvalue of the Hessian. Fig. 4.4 (a) shows contours of a two-dimensional potential energy function. The state A has two saddle points and the potential energy along a straight line passing through one saddle point, which can be regarded as a dividing surface, is illustrated in Fig. 4.4 (b). Since the potential energy has the minimum at the saddle point, this saddle point energy can be used as the critical value for a bias potential using the potential energy as a local variable. This approach is the one by Steiner *et. al.* mentioned above [5].

As a next candidate, consider the distance from the minimum as shown in Fig. 4.5, which is defined by

$$d = \sqrt{\sum_{k=1}^{3N} (r_k - r_{O,k})^2} \quad , \tag{4-29}$$

where r_k is a component of the position vector $\vec{r}$ and $r_{O,k}$ is a component of the position vector $\vec{r}_O$ at the minimum. It is obvious that when a system hops to other minima, the distance from the starting minimum should increase. In this case, the lower bound along the dividing surface is not necessarily located at a saddle point, but it must exist as shown in Fig. 4.5 (b). Unlike the lowest eigenvalue, there is no universal critical value for the distance, and in this case, the critical value largely depends on a system length scale. However, an experimental simulation for a given system may provide a guide for the critical value. If this is the case, then the distance from the minimum can be used to construct a bias potential. Then, the derivative of the distance is given by

$$\frac{\partial d}{\partial \vec{r}} = \frac{\vec{r} - \vec{r}_O}{d} \quad . \tag{4-30}$$

Note that the computational overhead due to the bias potential by the distance is negligible.

Another possible choice is the potential energy slope or curvature along the direction vector connecting a position and the minimum, $\vec{s} = (\vec{r} - \vec{r}_O)/d$. They are defined by

$$\sigma = \nabla V \cdot \vec{s} = \frac{d\,V}{d\,s} \quad , \tag{4-31}$$

$$\kappa = \frac{d^2 V}{d\,s^2} \quad . \tag{4-32}$$

In some specific systems, the slope in Eq. (4-31) and/or the curvature in Eq. (4-32) becomes smaller when the system approaches a dividing surfaces and in such cases it may be possible to determine critical values for them. The derivatives are given by

$$\frac{\partial \sigma}{\partial \vec{r}} = \frac{\vec{g}_1}{d} + \left[\frac{d^2 V}{d\,s^2} - \frac{\vec{g}_1 \cdot \vec{s}}{d} \right] \vec{s} \quad , \tag{4-33}$$

$$\frac{\partial \kappa}{\partial \vec{r}} = \frac{\vec{g}_2}{d} + \left[\frac{d^3 V}{d\,s^3} - \frac{\vec{g}_2 \cdot \vec{s}}{d} \right] \vec{s} \ , \tag{4-34}$$

where

$$\vec{g}_1 = -\frac{\partial (\vec{F}\,s)}{\partial s} = -\frac{\partial \vec{F}}{\partial s} - \vec{F} \quad , \tag{4-35}$$

$$\vec{g}_2 = -\frac{\partial^2 (\vec{F}\,s)}{\partial s^2} = -\frac{\partial^2 \vec{F}}{\partial s^2}\, s - 2\frac{\partial \vec{F}}{\partial s} \quad . \tag{4-36}$$

Note that all the higher order derivatives along a specific direction can easily be approximated using the finite difference scheme.

When we implement a bias potential, we find that combining two local variables is a more efficient way to obtain a larger boost factor. As discussed in Sec. 4.3.1, the maximum achievable boost factor is limited to the ratio of the phase space volume of the unboosted region to that of the entire basin. If we use one local variable λ_1 and its critical value is $\lambda_{1,cr}$, the unboosted region is a set of phase space points where $\lambda_1 < \lambda_{1,cr}$. If we use two local variables λ_1 and λ_2 with critical values $\lambda_{1,cr}$ and $\lambda_{2,cr}$, then the unboosted region becomes a subset of the phase space where $\lambda_1 < \lambda_{1,cr}$ "and" $\lambda_2 < \lambda_{2,cr}$. The phase space volume of this region is smaller than the volume of the region where $\lambda_1 < \lambda_{1,cr}$, which means a larger maximum achievable boost factor.

Fig. 4.6 shows a bias potential which is a function of two local variables; the eigenvalue and the slope. Using this bias potential, we can obtain additional gain in computations because we can avoid computing eigenvalues, which is very expensive, until slope approaches its critical value.

4.3.4. Useful formulas and Prediction of the behavior in the biased potential

I will conclude this section by describing several useful formulas for hyperdynamics simulation that will be important for the discussions that follows. These formulas provide (1) the relationship between the ensemble average in the original potential and that in the biased potential, and (2) the relationship between the probability distribution of a variable in the original potential and that in the biased potential.

The ensemble average, in the state A, of a variable $B(\vec{r})$ in the original potential and the ensemble average in the biased potential are given by

$$< B(\vec{r}) >= \frac{\int_A B(\vec{r})\, e^{-V/k_B T} d\vec{r}}{\int_A e^{-V/k_B T}\, d\vec{r}} \quad , \tag{4-37}$$

$$< B(\vec{r}) >_b = \frac{\int_A B(\vec{r})\, e^{-V_b/k_B T} d\vec{r}}{\int_A e^{-V_b/k_B T}\, d\vec{r}} \quad . \tag{4-38}$$

By manipulating Eq. (4-37) and Eq. (4-38), we obtain the following relationship

$$< B(\vec{r}) >= \frac{1}{\beta} < B(\vec{r})\ e^{\Delta V(\vec{r})/k_B T} >_b \quad . \tag{4-39}$$

When the average value is calculated by MD, then the following equation can be used.

$$< B(\vec{r}) > \approx \frac{\sum_k B(\vec{r}_k)\ e^{+\Delta V(\vec{r}_k)/k_B T}}{\sum_k e^{+\Delta V(\vec{r}_k)/k_B T}} \quad . \tag{4-40}$$

Now let us consider a conversion between the probability distribution in the original potential and that in the biased potential. The probability distribution of a variable λ in the original potential and that in the biased potential are given by

$$P(\lambda = \lambda_1) = \frac{\int_A \delta(\lambda(\vec{r}) - \lambda_1) e^{-V/k_B T} d\vec{r}}{\int_A e^{-V/k_B T} d\vec{r}} \quad . \tag{4-41}$$

$$P_b(\lambda = \lambda_1) = \frac{\int_A \delta(\lambda(\vec{r}) - \lambda_1) e^{-V_b/k_B T} d\vec{r}}{\int_A e^{-V_b/k_B T} d\vec{r}} \quad . \tag{4-42}$$

It can be shown that the following relationship between Eq. (4-41) and Eq. (4-42) holds,

$$P_b(\lambda = \lambda_1) = \beta \times e^{-\Delta V(\lambda_1)/k_B T} \times P(\lambda = \lambda_1) \ . \tag{4-43}$$

Thus, as discussed in the previous section, once a pre-simulation with the original potential has been performed with a proper number of time steps to sufficiently sample the phase space, we can obtain the distribution of λ, and, at the same time, we can predict the distribution in the biased potential and how the system will behave in the biased potential.

4.4 Schemes for a Driven System

In this section, we propose a modified hyperdynamics methodology for non-equilibrium systems, and we develop a parallel algorithm suitable for modeling frictional sliding in the thermally activated regime.

4.4.1. Hyperdynamics for a driven system

Hyperdynamics is based on transition state theory, which assumes a system is fully equilibrated at each local state (the local minimum and its neighborhood) and the rate of escape from the state is governed by the equilibrium properties of the state. However, in a system driven by time-varying external parameters, the potential energy changes with time. For example, we saw the total energy of a sliding system in the Tomlinson model changes as a slider moves.

Although this is the case, if the rate of change is slow enough to allow the atoms to equilibrate to the instantaneous potential energy, we can still apply the method developed from transition state theory. In deriving the analytical formulas that relate the friction force and the sliding velocity in the modified Tomlinson model, we used these same rate equations even though the potential energy changes in time. Thus, we assume that the framework for hyperdynamics is still valid for continuously changing potentials at sufficiently slow sliding rates.

Then, the remaining problem is how to define a bias potential for such time-varying potentials. We have several points to consider. First, continuously changing bias potentials are computationally expensive because the most bias potentials we discussed so far depend on the location of the potential energy minimum, which changes in time.

Second, the relationship between the time for the slider motion and the boost factor obtained from a bias potential is not clear in this case. Therefore, we have developed a modified hyperdynamics scheme to solve these problems using stepped sliding, as explained below.

In our AFM model the external parameter changing in time is the slider position, x_S, and the potential energy is a function of the slider position as well as the atomic positions. In stepped sliding, the slider position is updated by $\Delta\sigma$ after a time period $\Delta\tau$ has elapsed instead of changing continuously as shown in Fig. 4.7. $\Delta\tau$ is determined by the sliding rate ($\Delta\tau = \Delta\sigma / v_S$). Because both the slider position and the potential energy do not change for $\Delta\tau$, we can construct a bias potential for this system. For this process to be equivalent to the continuous sliding, $\Delta\sigma$ should be small compared to the length scale that characterizes the surface corrugation. Moreover, $\Delta\tau$ must be longer than the thermal equilibration time-scale ($\Delta\tau >> \tau_{eq}$). The validity of the stepped sliding simulations has been verified by direct comparison to continuous sliding as will be shown in Chap. V.

Now turn to the interpretation of the hyperdynamics simulations with the stepped sliding scheme. In the stepped sliding, if we use the original potential, frozen for $\Delta\tau$, we have to run the simulation for the same period $\Delta\tau$. Then, the probability for the transition for this time period is given by

$$1 - e^{-R\Delta\tau} , \tag{4-44}$$

where R is the transition rate. If we perform the same simulation with a biased potential, which has the boost factor of β, then the transition rate becomes faster ($R_b = \beta \times R$).

Note that we have the same probability for the shorter time period ($\Delta\tau_b = \Delta\tau / \beta$) because $1-e^{-R\Delta\tau} = 1-e^{-(R\beta)(\Delta\tau/\beta)} = 1-e^{-R_b\Delta\tau_b}$. Therefore, with the biased potential we can significantly reduce the simulation time.

4.4.2 Parallel Distribution Method

In addition to hyperdynamics, we can further reduce simulation time by using a parallel algorithm. Recall that transition state theory assumes each transition is uncorrelated. Moreover, in the previous section, we showed how we can update the slider position in a stepped way, assuming that the slider moves so slowly that the system is fully equilibrated at each slider position. Thus, the transition probabilities at each slider position during stepped sliding are independent of each other, and we do not necessarily need to perform the simulations successively. Rather, we can perform the simulations with different slider positions in parallel as illustrated in Fig. 4.8. For example, if we use the conventional serial algorithm for the system shown in Fig. 4.8, we have to first perform a simulation at $x_S = 1$ (Fig. 4.8 (a)), and after it finishes, we perform another simulation at $x_S = 2$ (Fig. 4.8 (b)), etc. until we observe a transition. This corresponds to throwing dice and throwing again after knowing the first result. However, if these two events are independent of each other, we can throw both simultaneously. Thus, we can perform four simulations at $x_S = 1, 2, 3, 4$, simultaneously. If we have a transition at $x_S = 3$ and this is the latest slider position that experienced a transition in the time interval, then we ignore the result at $x_S = 4$ and redistribute the jobs starting from $x_S = 3$ and restart to perform the simulations. The speed-up obtained by this parallel distribution method is roughly proportional to the number of processors used for one system.

If we use this method combined with hyperdynamics, we can reduce the simulation time at each processor by the boost factor β. The overall efficiency of this combined method will be

$$\frac{(\#\,of\ \ processors)\times(the\,boost\ \ factor\ of\ \ the\,bias\ \ potential)}{(computational\ overhead\ due\,to\,extra\,calculations\ \ for\ hyperdynamics)}.$$

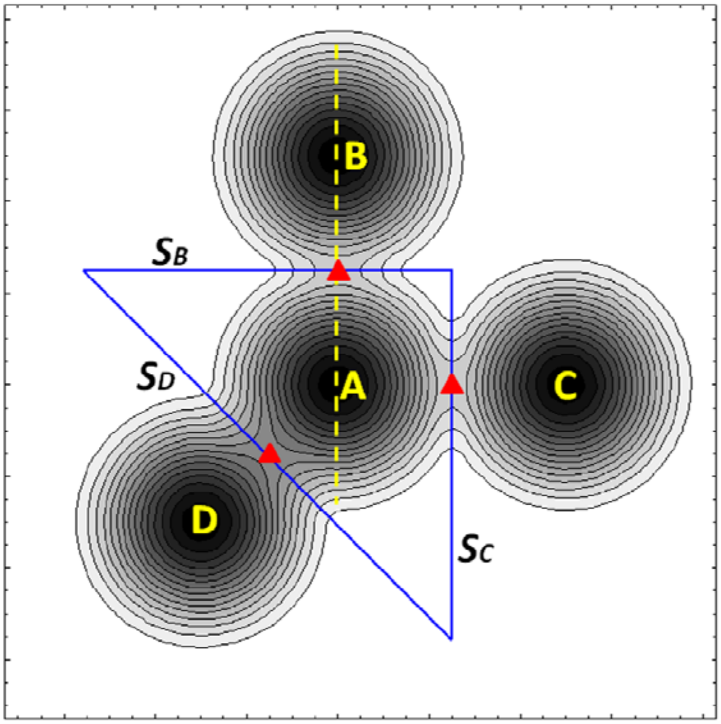

Figure 4.1 Contours of a two-dimensional example potential energy, which has four minima (dark regions labeled by A, B, C, and D). The saddle points are shown as red triangles and blur curves represent dividing surface separating A from others.

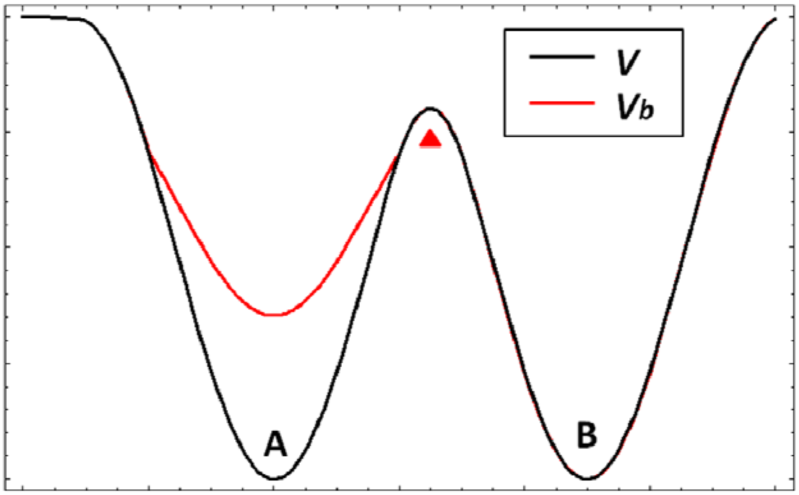

Figure 4.2 Cross-section of a two-dimensional example potential energy along the dashed line connecting A and B shown in Fig. 4.1.

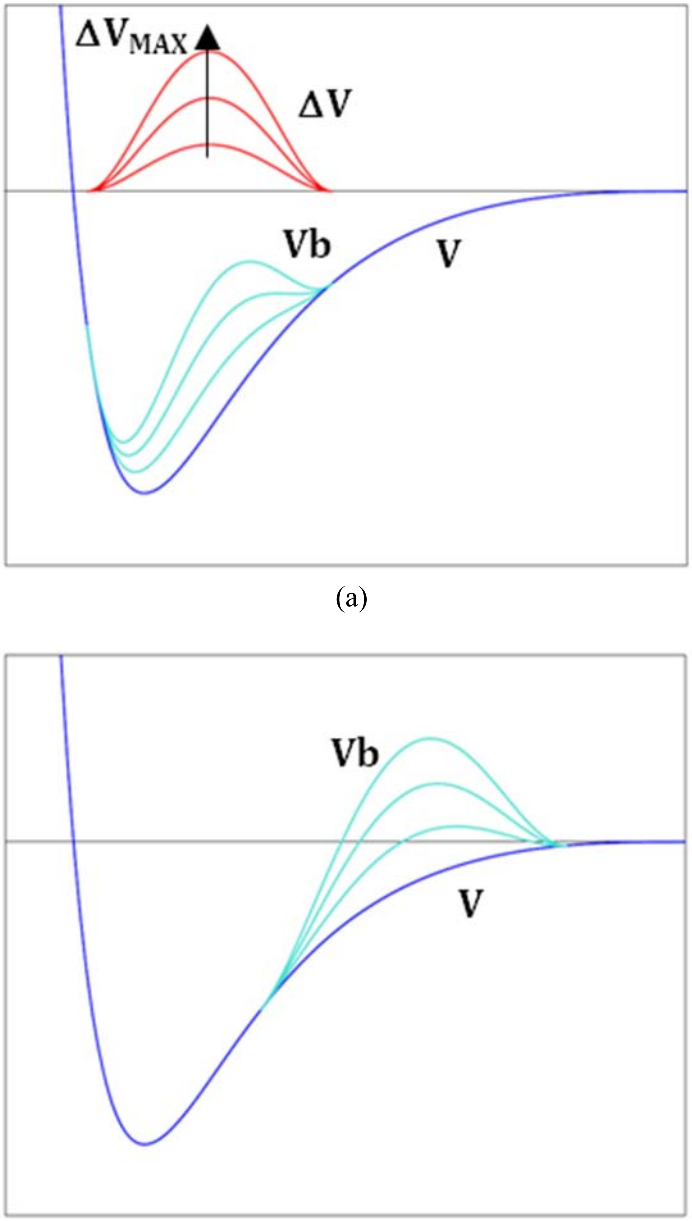

(a)

(b)

Figure 4.3 Illustrations of double-well introduction in the bond-boost method. Blue curves are the original pair interactions, red curves are bias potentials, and cyan curves are the resulting biased potentials. (a) Large bias potentials are added to the original potential. (b) Bias potentials are added to unbound pair.

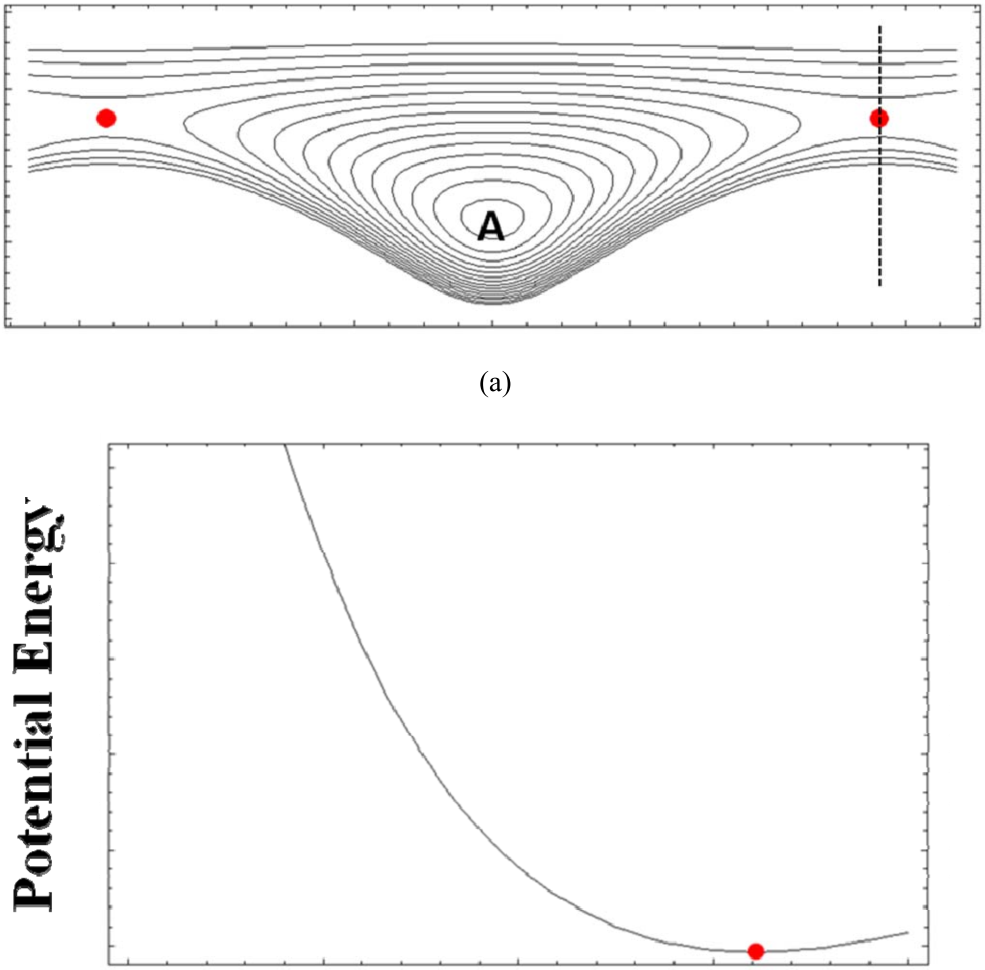

(a)

(b)

Figure 4.4 (a) Contour lines of a potential energy. Red dots are saddle points and A labels the minimum. (b) Potential energy plotted along the dashed line shown in (a).

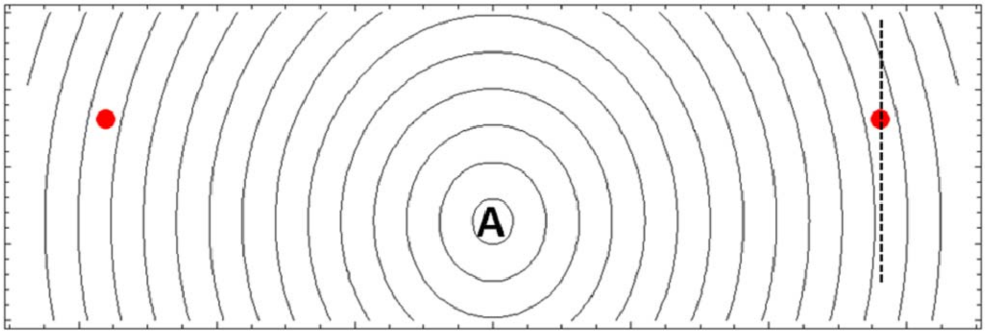

(a)

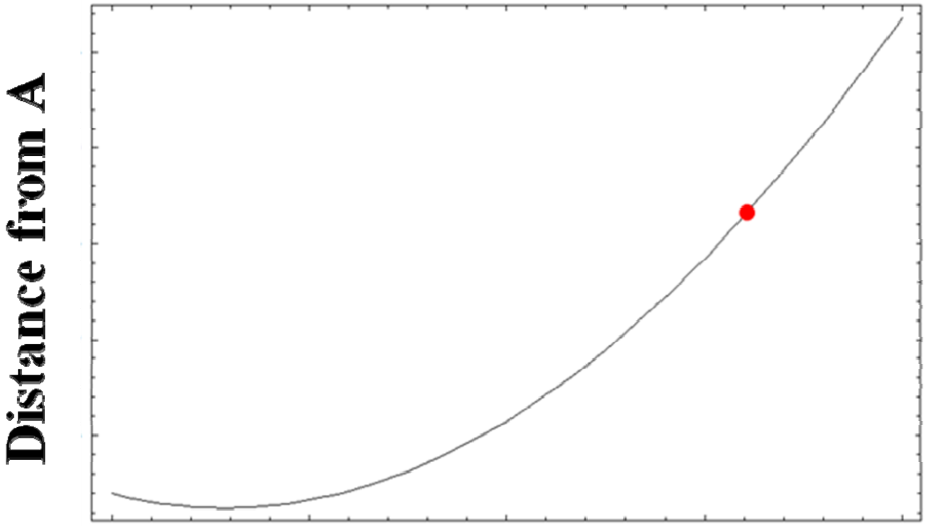

(b)

Figure 4.5 (a) Contour lines of distance from the minimum A. Red dots are saddle points and A labels the minimum. (b) Distance plotted along the dashed line shown in (a).

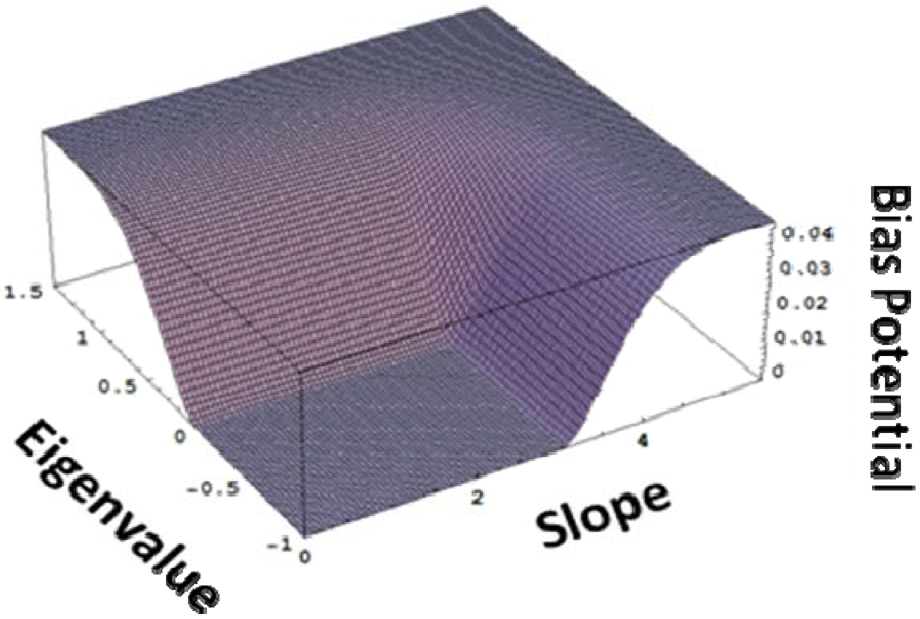

Figure 4.6 An illustration of a bias potential defined as a function of the eigenvalue and the slope.

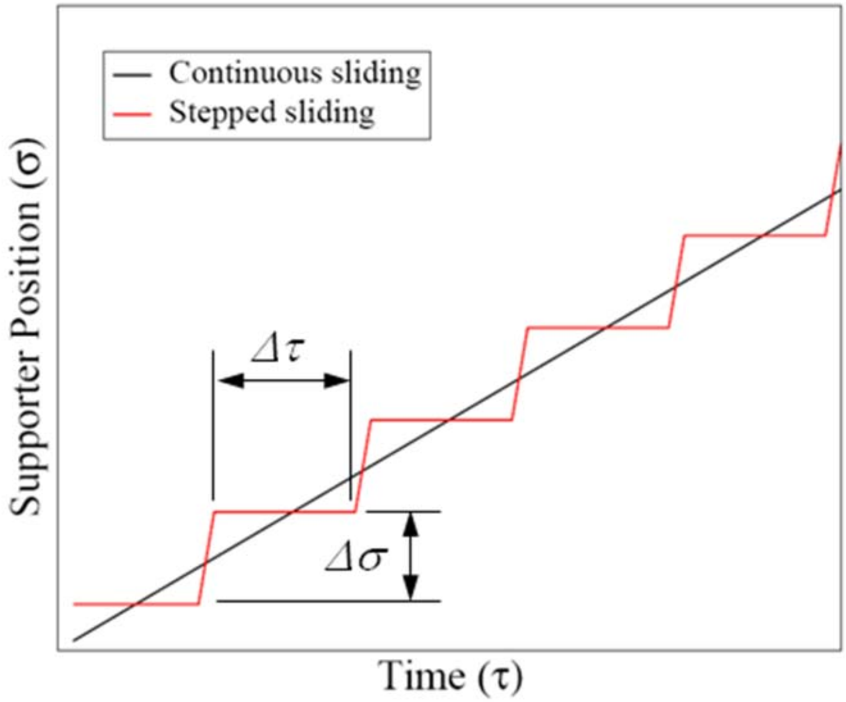

Figure 4.7 Slider position vs. time. The Black line represents the continuous change of the slider position in time, and in the red lines, the slider position is fixed for $\Delta\tau$ and updated by $\Delta\sigma$ after this time period has elapsed.

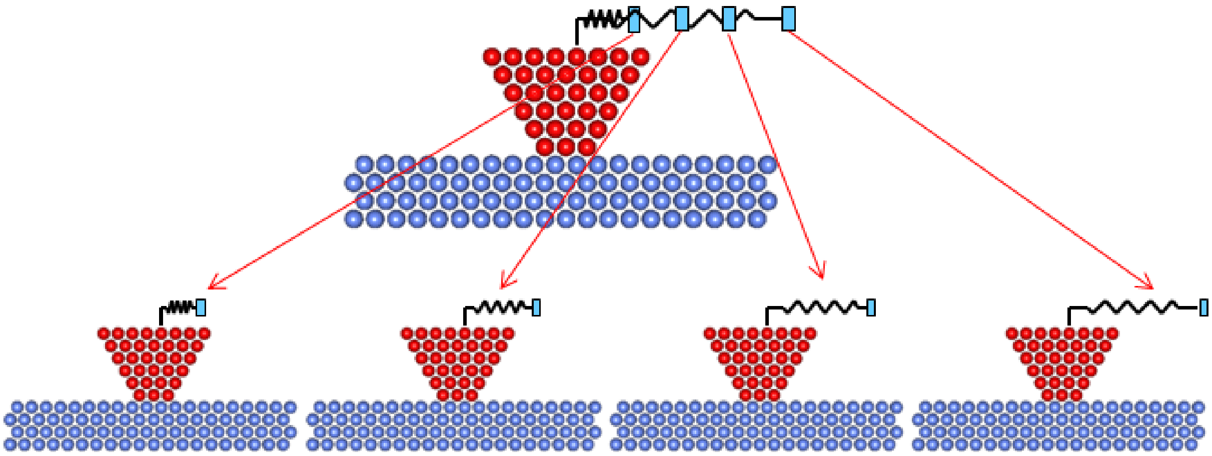

(a) $x_S = 1$ (b) $x_S = 2$ (c) $x_S = 3$ (d) $x_S = 4$

Figure 4.8 An illustration of the parallel distribution method.

References

[1] A. F. Voter, "*A Method for Accelerating the Molecular Dynamics Simulation of Infrequent Events*", J. Chem. Phys. 106, 4665 (1997).

[2] A. F. Voter, "*Hyperdynamics: Accerlated Molecular Dynamics of Infrequent Events*", Phys. Rev. Lett., 78, 3908 (1997).

[3] E. M. Sevick, A. T. Bell, and D. N. Theodorou, "*A Chain of States Method for Investigating Infrequent Event Processes Occurring in Multistate, Multidimensional Systems*", J. Chem. Phys., 98, 3196 (1993).

[4] R. A. Olsen, G. J. Kroes, G. Henkelman, A. Arnaldsson, and H. Jonsson, "*Comparison of Methods for Finding Saddle Points without Knowledge of the Final States*", J. Chem. Phys., 121, 9776 (2004).

[5] M. M. Steiner, P.-A. Genilloud, J. W. Wilkins, "*Simple Bias Potential for Boosting Molecular Dynamics with the Hyperdynamics Scheme*", Phys. Rev. B, 57, 10236 (1998).

[6] R. A. Miron and K. A. Fichthorn, "*Accelerated Molecular Dynamics with the Bond-Boost Method*", J. Chem. Phys., 119, 6210 (2003).

CHAPTER V

Methodological Validation

5.1 Introduction

In the previous chapters, we developed various efficient methods to perform molecular dynamics simulation of a driven system on a longer time scale. Although these methodologies could be applied to any driven system with time-varying external parameters, we will focus on simulating frictional sliding, in particular, the AFM experiment. To accomplish this and to systematically test our methodologies, we apply these procedures in succession, testing our results for consistency. We first replace the continuous motion of the slider by stepped motion where the slider position is fixed for a prescribed time period and updated to a new position after this period has elapsed. Next we apply the parallel algorithm during which simulations at various slider positions are performed simultaneously on multiple processors. Finally these simulations are accelerated with the hyperdynamics scheme using biased potentials.

In this chapter, these methods are tested with simple 2-dimensional and 3-dimenstional AFM models. We used four different methods;

(1) Continuous sliding on a single processor,

(2) Stepped sliding on a single processor,

(3) Stepped sliding using the parallel method,

(4) Stepped sliding using a biased potential (hyperdynamics) with the parallel method.

Method (4) using hyperdynamics is the most efficient method when a suitable biased potential can be employed that does not result in excessive computational overhead.

In the subsequent sections, the simulation results are presented. In addition, these simulations have provided an opportunity to test the theories discussed in Chap. III.

5.2 2-Dimensional Model

5.2.1 Simulation

A simple 2-dimensional AFM model is shown in Fig. 5.1. The substrate consists of 80 atoms marked in blue, and the tip contains 33 atoms marked in red. The tip and the substrate have a 2-dimensional crystalline structure corresponding to an FCC crystal in 3-dimension. The lattice parameters of the tip and the substrate are identical. Thus, the tip atoms contacting the substrate are located at the lattice sites of the substrate as shown in Fig. 5.1.

The atoms on the bottom layer of the substrate are fixed to prevent a rigid-body translation in the vertical direction, and the system is subject to the periodic boundary condition in the horizontal direction. The relative motions of the atoms on the top layer of the tip are constrained, but they can move like a rigid body. These top atoms are pulled by a spring and pushed downward by the applied normal force as shown in Fig. 5.1. We used a spring stiffness of $k = 5\ \varepsilon / \sigma^2$ and an applied normal force of $F_N = 5\ \varepsilon / \sigma$. All the quantities are expressed with the length unit σ, the energy unit ε, and the mass unit *m*. For example, the time is measured in the time unit of $\tau = \sqrt{m \sigma^2 / \varepsilon}$

The interactions of the atoms are modeled by the Lennard-Jones potential,

$$V(r) = 4\,\varepsilon_{ab}\left[\left(\frac{\sigma_{ab}}{r}\right)^{12} - \left(\frac{\sigma_{ab}}{r}\right)^{6}\right], \tag{5-1}$$

where ε_{ab} is the bond energy between the atom of the type a and the atom of the type b, σ_{ab} is the characteristic length parameter, and r is the distance between the two atoms. We used the following parameters.

$\sigma_{ss} = \sigma_{tt} = \sigma_{ts} = 1.0\,\sigma$, $\varepsilon_{ss} = \varepsilon_{tt} = 1.0\,\varepsilon$, $\varepsilon_{ts} = 0.5\,\varepsilon$ (*s*: substrate, *t*: tip)

Note that we used a smaller value of the bond energy for the interaction between the tip and the substrate to guarantee that the shear deformation always occurs at the interface rather than inside the tip.

For the hyperdynamics simulations, we used bias potentials constructed using the eigenvalue of the Hessian and the local slope of the potential energy as defined in Chap. IV. The critical value for the eigenvalue can be set to zero, but to obtain the critical value for the local slope, we perform pre-simulations near the transitions. The detailed procedure is explained as follows. First, from the simulation results at higher velocities using the original potential we estimate the slider positions where transitions occur. Then, we prepare a certain number of samples (typically 100 samples are used) with different initial conditions at a slider position earlier than the estimated slider positions in the previous step. With these samples, we perform sliding simulations at a specific sliding velocity, which is usually lower by one order of magnitude than the sliding velocities used in the original simulations. During simulations, to detect the moment of transition and determine the local slope value at that moment, we perform minimizations periodically when the calculated slope is larger than a provisional limit and at every step while the slope is smaller than the limit. Finally, we set the critical value to the maximum (with a safety factor) among these values.

In case a system experiences transitions in a non-uniform potential energy landscape, the critical values obtained at one specific transition may not be suitable for other transitions. With such systems, we have to use a bias potential defined only with the eigenvalue which has the universal critical value of zero. Therefore, devising a systematic scheme to estimate critical values on the fly remains as a challenge.

Moreover, since the local slope is measured along the direction connecting a current position and the minimum, a new local minimum must be found whenever the slider position is updated to a new position. After the new minimum is indentified, the boost factor is calculated by a simulation with the original potential. Then, the hyperdynamics simulation is performed using the biased potential with the pre-calculated boost factor.

We varied the sliding velocity by 5 orders of magnitude ranging from $v_S = 10^{-4}\ \sigma / \tau^2$ to 10^{-8} and three different temperatures ($T = 0.1, 0.01, 0.001\ \varepsilon / k_B$) have been simulated using the Nose-Hoover chain method [1]. The equations of motion are solved using a modified velocity-Verlet algorithm [2].

5.2.2 Simulation Results

The graphs shown in Fig. 5.2 through Fig. 5.5 are obtained from a simulation with $v_S = 10^{-6}$ and $T = 0.01$ (starting from this point, units are omitted unless there is ambiguity) and illustrate typical frictional behaviors of the model.

Fig. 5.2 shows the tip position as a function of the slider position, and the slider position is plotted together with the tip position. The tip position is measured at the top layer. As in the Tomlinson model, apparent stick-slip motion is observed. The tip position increases linearly during the stick-phase and jumps at several discrete points corresponding to slip events. The average distance of these points corresponds to the lattice parameter of the substrate. Note that the tip position, x_T , shown in the figure also represents the quantity averaged over a time period (otherwise the curve is very noisy due to thermal fluctuations) and is not identical to the location at the local minimum. Thus,

$$\bar{x}_T = \frac{1}{N_{MD}} \sum_{i=1}^{N_{MD}} x_T(t_i) \approx \langle x_T \rangle = \frac{\int x_T \, e^{-V(\vec{r})/k_B T} d\,\vec{r}}{\int e^{-V(\vec{r})/k_B T} d\,\vec{r}} \quad , \tag{5-2}$$

where N_{MD} is the number of steps in the time period for the average and the slider position either is fixed (during stepped sliding) or changes a small amount (during continuous sliding) for this time period. In case of stepped sliding, we update the slider position by $\Delta\sigma = 0.01$ and the time period, $\Delta\tau$ ($= \Delta\sigma / v_S$), during which the slider position is fixed increases as the sliding velocity decreases. We use $\Delta\tau_{dsv} = \Delta\tau / 10$ for the time period for the average so that N_{MD} ($= \Delta\tau_{dsv} / \Delta t_{MD}$) increases as the sliding velocity decreases. Δt_{MD} is the time interval for numerical integration. For continuous sliding, we use as many steps for the average as used in stepped sliding at the same sliding velocity.

Fig. 5.3 (a) shows the lateral force as a function of the slider position, and Fig. 5.3 (b) shows the lateral force as a function of the tip position. The lateral force, F , is also averaged over a time period and has the following relation with the tip position,

$$\overline{F} = \overline{k\,(x_S - x_T)} = k\,(x_S - \overline{x}_T) \approx k \left(x_S - \frac{\int x_T\, e^{-V/k_B T} d\,\vec{r}}{\int e^{-V/k_B T} d\,\vec{r}} \right) . \qquad \text{(5-3)}$$

As expected from Fig. 5.2, where the tip position is linearly proportional to the slider position ($x_T \approx k_C\, x_S$), the lateral force exhibits a linear dependence on both the slider position and the tip position. The lateral forces at each peak are not identical to each other and have a distribution as we discussed in Chap. III. Fig. 5.4 shows a closer look at the lateral force curves near a transition. The straight line extends from the initially linear portion of the curves and illustrates that the lateral force deviates from the linear dependence near the transition. Thus, the assumption that $F = k_{eff}\, x_S$ in Eq. (3-32), used in the derivation of the relationship between the lateral force and the sliding velocity, is not strictly correct even in this simple model.

The potential energy, which is a function of the tip position as well as the atom positions, $V(\vec{r}_1, \cdots, \vec{r}_N; \vec{r}_T)$, is shown in Fig. 5.5. Fig. 5.5 (a) shows the potential energy as a function of the slider position, and Fig. 5.5 (b) shows the potential energy as a function of the tip position. The potential energy is averaged for a time period,

$$\overline{V}(x_S) \approx \langle V \rangle = \frac{\int V(\vec{r})\, e^{-V(\vec{r})/k_B T} d\,\vec{r}}{\int e^{-V(\vec{r})/k_B T} d\,\vec{r}} . \qquad \text{(5-4)}$$

The increase in the potential energy is due to the elastic deformation of the tip and can be fit to a quadratic function. We expect that

$$\overline{V} \sim \frac{1}{2} k_1\, x_S^2 \quad , \qquad \text{(5-5)}$$

where k_1 is a constant. From Fig. 5.4, we could expect that the potential energy would deviate from the quadratic form near transition, but such deviation is not clear in Fig. 5.5.

Fig. 5.6 shows the dependence of the lateral force on the sliding velocity. At a temperature of 0.01 the results from five different sliding velocities ($10^{-4}, 10^{-5}, 10^{-6}, 10^{-7}$, 10^{-8}) are shown. It is apparent that as the sliding velocity decreases the tip makes a transition at an earlier slider position, which is consistent with the prediction of the modified Tomlinson model [3, 4]. The temperature dependence is shown in Fig. 5.7 and Fig. 5.8. In Fig. 5.7, we can observe that the transition occurs at much earlier slider position at higher temperature, and the effective stiffness k_{eff}, the slope of the lateral force vs. slider position curve, slightly reduces as temperature increases due to softening of the tip and contact stiffness. Fig. 5.8 shows the lateral forces as functions of temperature with linear fits. By manipulating Eq. (3-36), we have the following relation,

$$\widetilde{F} = F_C^+ - \frac{1}{\lambda} \ln\left[\frac{f_O}{\lambda k_{eff} v_S}\right] k_B T - \frac{\ln(k_B T)}{\lambda} k_B T \quad , \tag{5-6-a}$$

$$\approx F_C^+ - \alpha T \quad (\alpha > 0) \; . \tag{5-6-b}$$

In Eq. (5-6-b), we assume that the second term on the right hand side in Eq. (5-6-a) is more dominant than the third term and $f_O > \lambda k_{eff} v_S$. Note that α increases as v_S decreases, and this agrees with the trend shown in Fig. 5.8.

Finally, we compare the results from various methods. Fig. 5.7 summarizes the simulation results at various sliding velocities and various temperatures obtained from the four different methods listed in Sec. 5.1. At each velocity and temperature, we prepared 10 samples for serial simulations and 5 samples for parallel simulations. Each sample has different initial conditions. The lateral forces in this graph are measured at the transition points and averaged over eight different transition points and over different samples.

The continuous sliding and the stepped sliding (using the original potential on a single processor) are tested at the velocities of $10^{-4}, 10^{-5}, 10^{-6}$ and at temperatures of 0.001, 0.01, 0.1. All the data overlap and agree within the range of the standard deviation shown as the error bar in Fig. 5.7. Most data ranges even within the standard error.

At the sliding velocity of 10^{-6} and the temperature of 0.01, all four methods are tested and all the measured lateral forces agree. The simulations on a single process could not been performed at the sliding velocities lower than 10^{-6} due to excessive running time on a standard workstation, but all the data from the parallel simulations at 10^{-7} and 10^{-8} using either the original potential or the biased potential range close to the trend line extended from the data obtained from continuous sliding.

The lateral forces show the logarithmic dependence on the sliding velocity, and no plateaus are found in any velocity range. The slope of the lateral force vs. ln v_S curve increases as temperature increases, and this trend agrees with the prediction of Eq. (3-36).

5.2.3 Discussion

With the conventional method, we were not able to perform simulations at velocities lower than 10^{-6} because of the extended running time on a standard workstation. With the velocities above this limit, the simulation results from the stepped sliding agree with the results of the continuous sliding. Thus, the platform for the other methods (the parallel method and the hyperdynamics methods) is well verified. Using the parallel method makes it possible to lower the sliding velocity by one order of magnitude, and with the hyperdynamics methodology we can lower the sliding velocity further.

As discussed in Chap. IV, the maximum achievable boost factor depends on the phase space volume of the unboosted region. In this 2-dimensional sliding system, we have found that the volume of the unboosted region in the phase space is altered as the slider position changes. When the slider position is far from the transition point, the pre-simulation using the original potential to calculate the boost factor does not sample any points in unboosted region. Thus, in principle, there is no limit for the maximum boost factor. However, as the slider approaches the transition point, some unboosted points are sampled and the maximum achievable boost factor reduces. Since as the sliding velocity decreases the transition occurs at earlier slider positions where the maximum boost factor is larger, we expect that we can reduce the sliding velocity further below 10^{-8}.

Although the lateral force shows a logarithmic dependence on the sliding velocity, this is likely due to the simplicity of the current model. Since the tip maintains its crystalline structure after transitions and no defects arise inside the tip due to much weaker interaction between the tip and the substrate, the only possible transition mechanisms are backward and forward hopping, which have initially the same magnitude of energy barriers. As the slider advances, the forward hopping (in the sliding direction) becomes more favorable than the backward hopping. Moreover, the relative configurations of the system before and after transition do not change.

However, in more realistic situations, the tip may lose atoms during sliding and its interface configuration may be altered during transitions. In the subsequent chapters, we treat more complicated models; the incommensurate surface model and the amorphous interface model.

5.3 3-dimensional Model

Before moving on to more realistic models, we tested the methods using a 3-dimensional system. This model exhibits transitions through the same mechanism as the 2-dimensional model, but reveals the increasing difficulty of reducing the sliding velocity as the problem size and complexity increase.

5.3.1 Simulation

Fig. 5.10 illustrates a 3-dimenstional system modeling an AFM tip and a substrate. The tip has 183 atoms shown in red and the substrate consists of 1800 atoms shown in blue. The substrate has FCC crystalline structure, and the tip is created by carving an FCC crystal with the same lattice parameter as the substrate into a conical shape with flat ends. The tip and the substrate are joined in the [001] direction, and as shown on the right side of Fig. 5.10, nine atoms on the bottom of the tip are in contact with the substrate. Because the tip and the substrate have the same lattice parameter and are aligned in the same orientation the tip atoms are in registry with the substrate.

The sliding simulation is realized in the same way as the 2-dimensional model. A spring ($k = 10$) is linked to the top layer of the tip and the bottom layer of the substrate is fixed. A normal force ($F_N = 5$) is applied to the top of the tip.

The interaction between substrate atoms and the interaction between a substrate atom and a tip atom are modeled by the Lennard-Jones (L-J) potential, and the following parameters are used.

$$\begin{matrix} \sigma_{ss} = 1.0\,\sigma \\ \sigma_{st} = 1.0\,\sigma \end{matrix} \;,\quad \begin{matrix} \varepsilon_{ss} = 1.0\,\varepsilon \\ \varepsilon_{st} = 0.2\,\varepsilon \end{matrix} \quad \text{(}s\text{: substrate, }t\text{: tip)}$$

For the interaction between tip atoms, we used a harmonic potential, which does not allow any bond breaking to maintain the shape of the tip and prevent wear during sliding.

$$V(r) = \frac{1}{2} k \,(r - r_O)^2 \;, \tag{5-7}$$

where k is the stiffness (= 57.2), and r_O is the equilibrium bond length (= 1.12). The stiffness and the equilibrium length are chosen to be identical to the values of the L-J potential with $\sigma_{tt} = 1, \varepsilon_{tt} = 1$ at the equilibrium position.

We performed simulations at four different sliding velocities (10^{-4}, 10^{-5}, 10^{-6}, 10^{-7}) and at a temperature of 0.01. As in the 2-dimensional model, we used the Nose-Hoover chain method to control temperature [1] and a modified velocity-Verlet algorithm to numerically solve the equations of motion [2].

5.3.2 Results

We plotted the lateral force and the potential energy as functions of both the slider position and the tip position in Fig. 5.11, Fig. 5.12, and Fig. 5.13, where the data are obtained from the simulations with $v_S = 10^{-5}$ and $T = 0.01$. As in the 2-dimensional case, the lateral forces show the linear dependence (Fig. 5.11), but deviate from the straight lines near transition points (Fig. 5.12). The potential energy changes like a quadratic function of the slider position at earlier slider positions, but shows earlier deviation from the quadratic fits than 2-D models and very stiff changes near transitions (Fig. 5.13).

Fig. 5.14 summarizes the simulation results. The lateral forces shown in the figure are the averages of the peak values at each transition over the samples and the peaks. At sliding velocities of 10^{-4} and 10^{-5}, the lateral forces measured from the continuous sliding show close agreement with the forces from the stepped sliding. Thus, the fundamental assumption of our methodologies is verified with this 3-dimensional model. However, although the number of atoms in this model (1,983) is not large, the simulations on a single processor using the conventional method at lower sliding velocities ($\leq 10^{-6}$) are prohibitive due to the running time requiring more than one month on a standard workstation.

By the parallel method using 50 processors, we were able to perform MD simulations at a sliding velocity of 10^{-6}. The running time was less than a week. However, without the aid of hyperdynamics, the simulations at lower sliding velocities ($\leq 10^{-7}$) are not attainable because whenever we lower the sliding velocity by a factor of 10, we have to increase the running time 10 times. Using a bias potential constructed using the eigenvalue and the local slope, the simulations at a sliding velocity of 10^{-7} could be performed.

All the data measured from the various methods show close agreement with the trend line obtained from the continuous method on a single processor within the standard deviation shown as the error bars in Fig. 5.14. Moreover, as expected from the modified

Tomlinson model, the lateral force exhibits the logarithmic dependence on the sliding velocity within the range of the parameters used in this simulation study.

5.4 Conclusions

The validity of the methodologies is well verified with the simulations of the 2-dimensional and 3-dimensional AFM models. With both methods, the stepped sliding serves as a reasonable approximation for continuous sliding, and the simulation results using the other methods both the parallel methodology and hyperdynamics showed close agreements with the simulation results of the conventional method.

Moreover, both 2-D and 3-D simulations showed that the average of the lateral forces at the transitions have the logarithmic dependence on the sliding velocity. 2-D simulation at three temperature points showed the lateral force linearly decreases as the temperature increases.

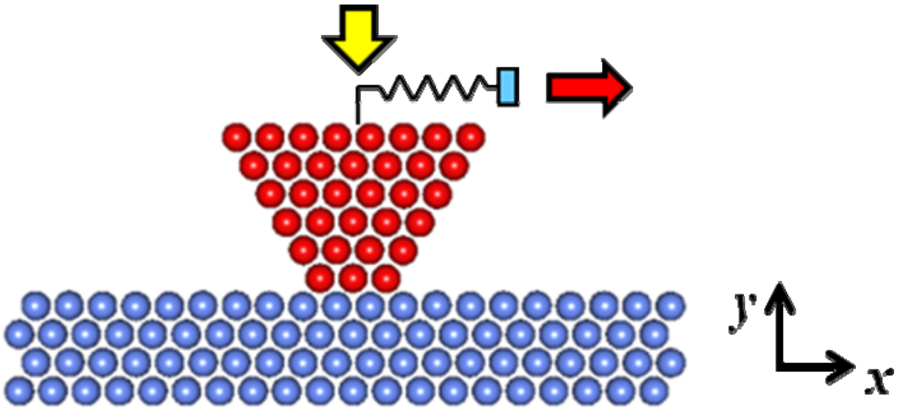

Figure 5.1 A diagram of a 2-dimensional AFM model consisting of a tip and a substrate. The tip atoms are shown in red and the substrate atoms are shown in blue. The top layer of the tip is pulled by a spring, which is attached to a slider moving in the positive x direction (the red arrow), and pushed by a normal force expressed as the yellow arrow.

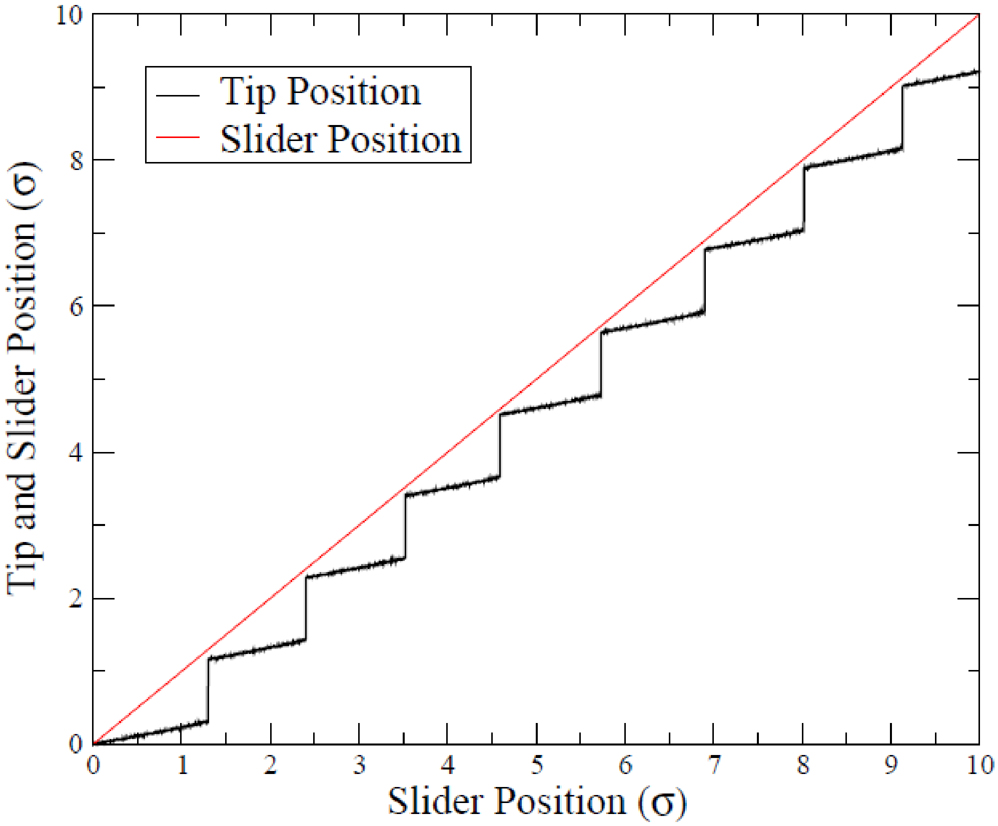

Figure 5.2 Tip position as a function of slider position calculated from the 2-D model simulated at $v_S = 10^{-6}$ and $T = 0.01$. Slider position is also plotted for comparison.

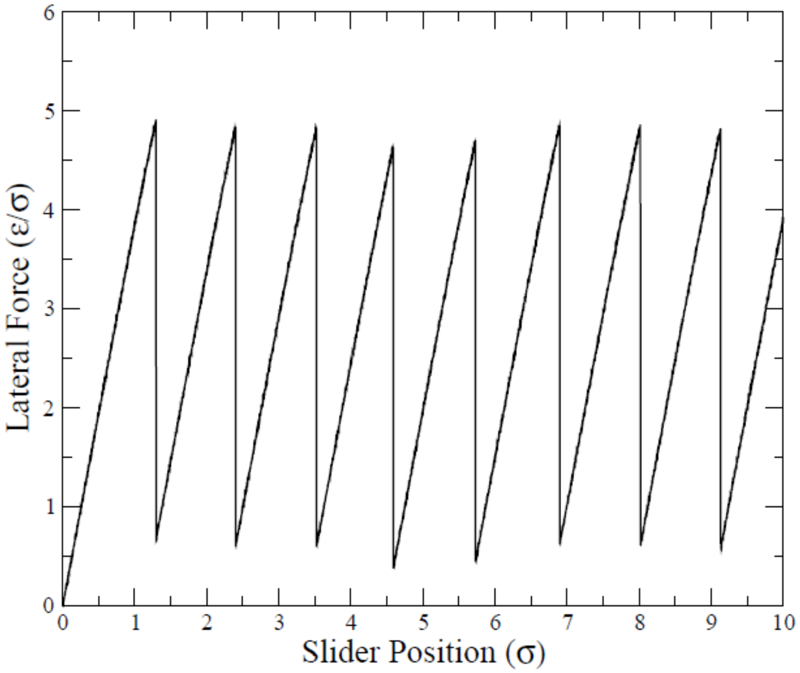

(a)

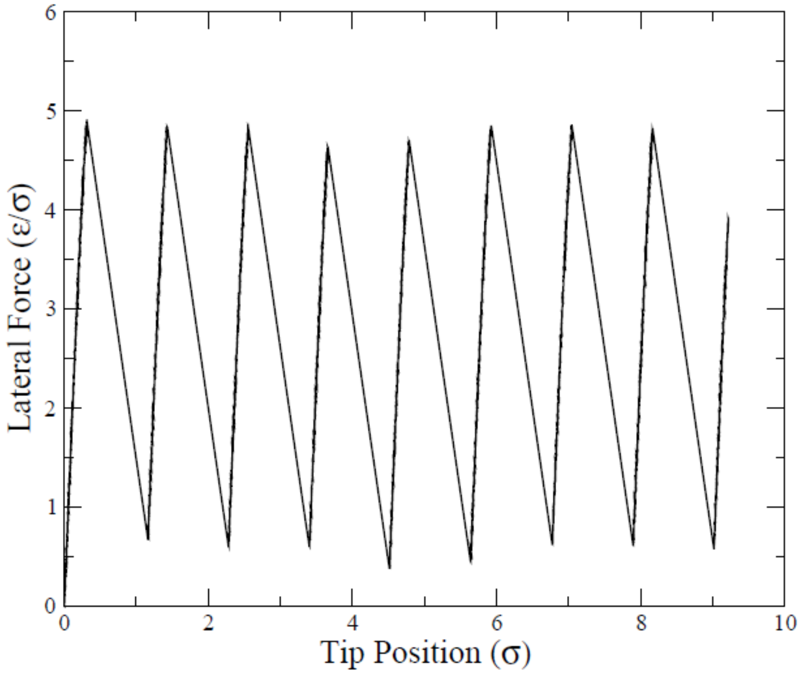

(b)

Figure 5.3 Lateral forces calculated from the 2-D model simulated at $v_S = 10^{-6}$ and $T = 0.01$. (a) Lateral force vs. slider position and (b) Lateral force vs. tip position.

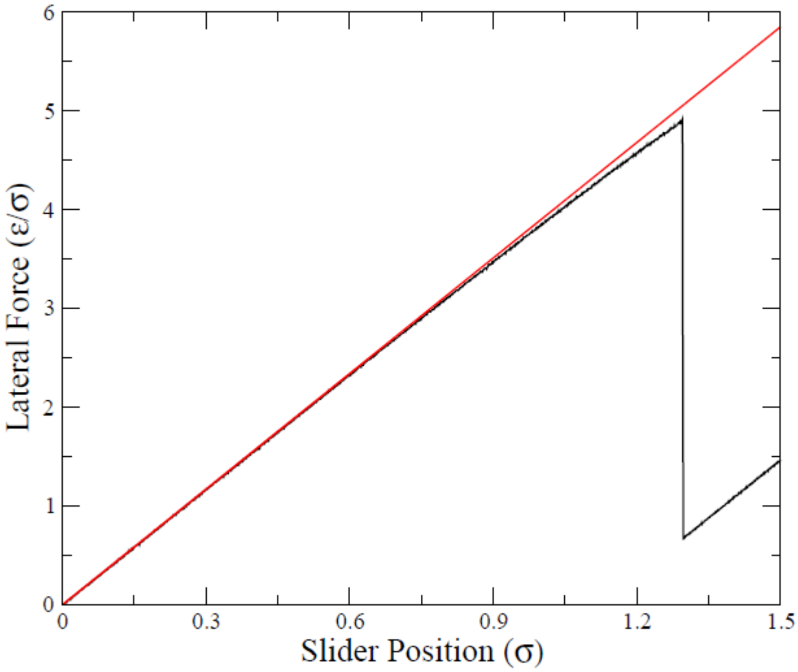

(a)

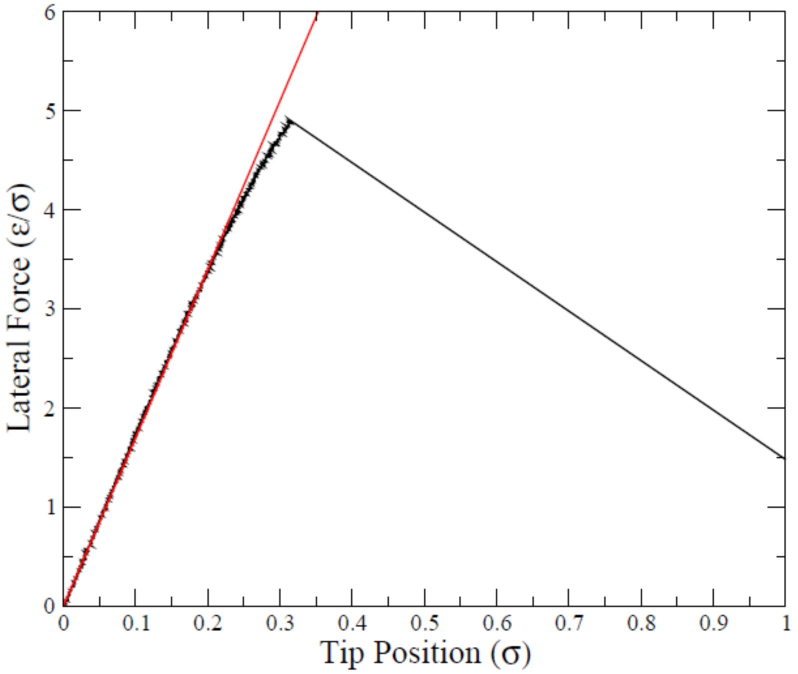

(b)

Figure 5.4 Lateral forces (black curves) calculated from the 2-D model simulated at $v_S = 10^{-6}$ and $T = 0.01$ and linear fittings (red straight line) extended from initially linear portion (a) Lateral force vs. slider position and (b) Lateral force vs. tip position.

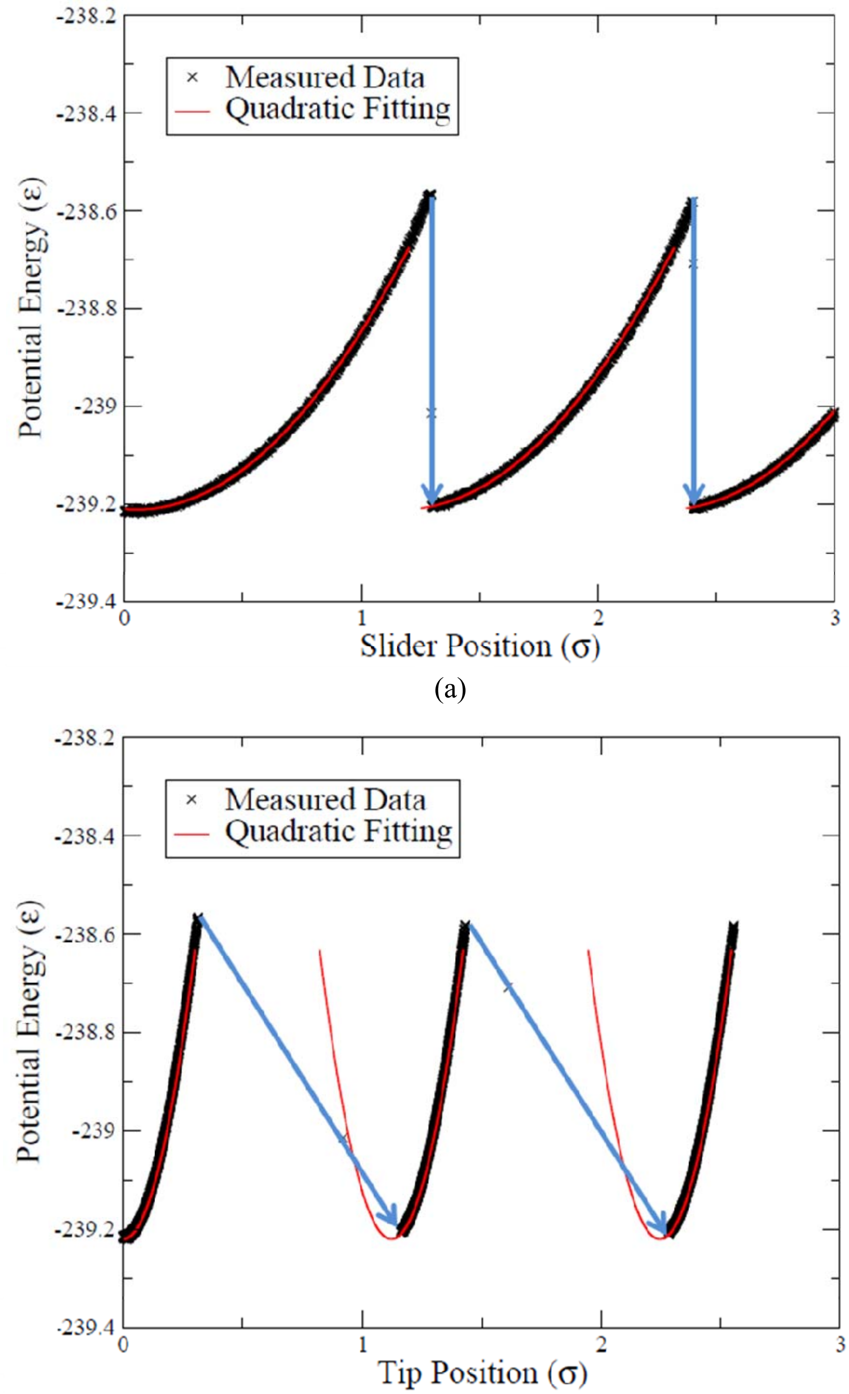

(a)

(b)

Figure 5.5 Potential energy curves (black curves) obtained from the 2-D model simulated at $v_S = 10^{-6}$ and $T = 0.01$, and quadratic fittings (red curves). The discontinuous points are connected by blue arrows. (a) Potential energy vs. slider position and (b) Potential energy vs. tip position. The blue arrows indicate transitions.

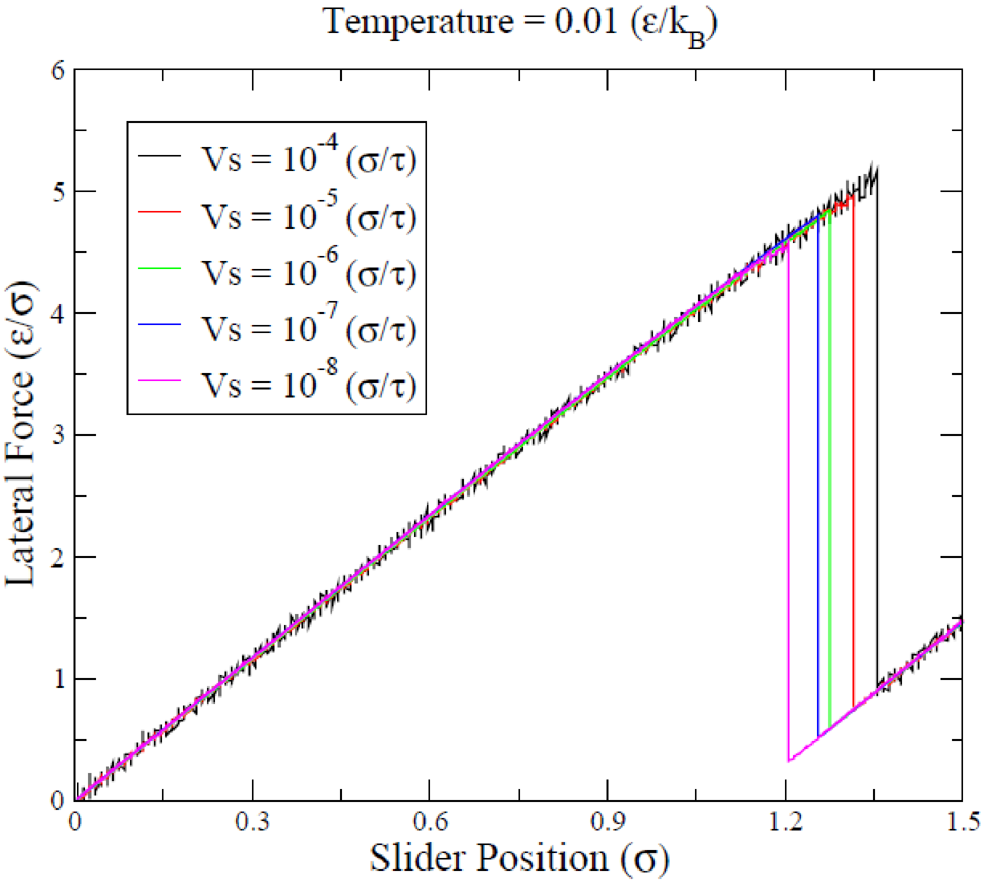

Figure 5.6 Sliding velocity dependence of lateral force obtained from the 2-D model simulated at $T = 0.01$. Lateral forces are shown as functions of slider position at five different sliding velocities ($v_S = 10^{-4}, 10^{-5}, 10^{-6}, 10^{-7}, 10^{-8}$).

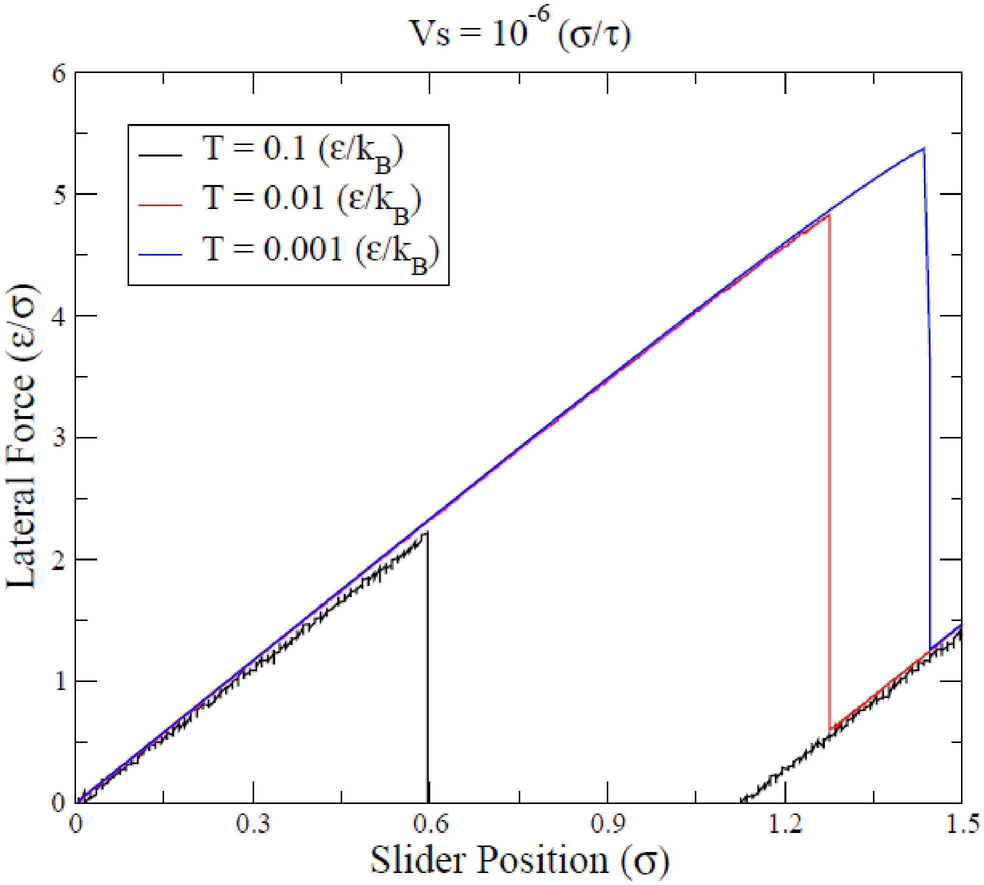

Figure 5.7 Temperature dependence of lateral force obtained from the 2-D model simulated at $v_S = 10^{-6}$. Lateral forces are shown as functions of slider position at three temperatures ($T = 0.001, 0.01, 0.1$).

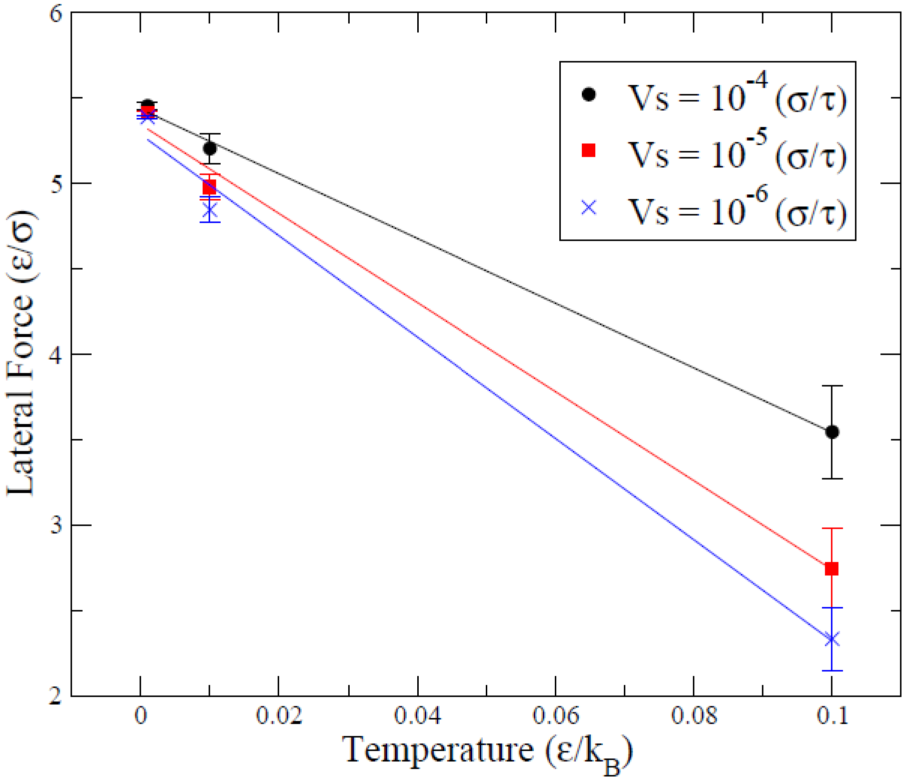

Figure 5.8 Lateral forces as functions of temperature obtained from the 2-D model simulated at three different sliding velocities ($v_S = 10^{-4}, 10^{-5}, 10^{-6}$). The straight lines are the linear fittings of the data.

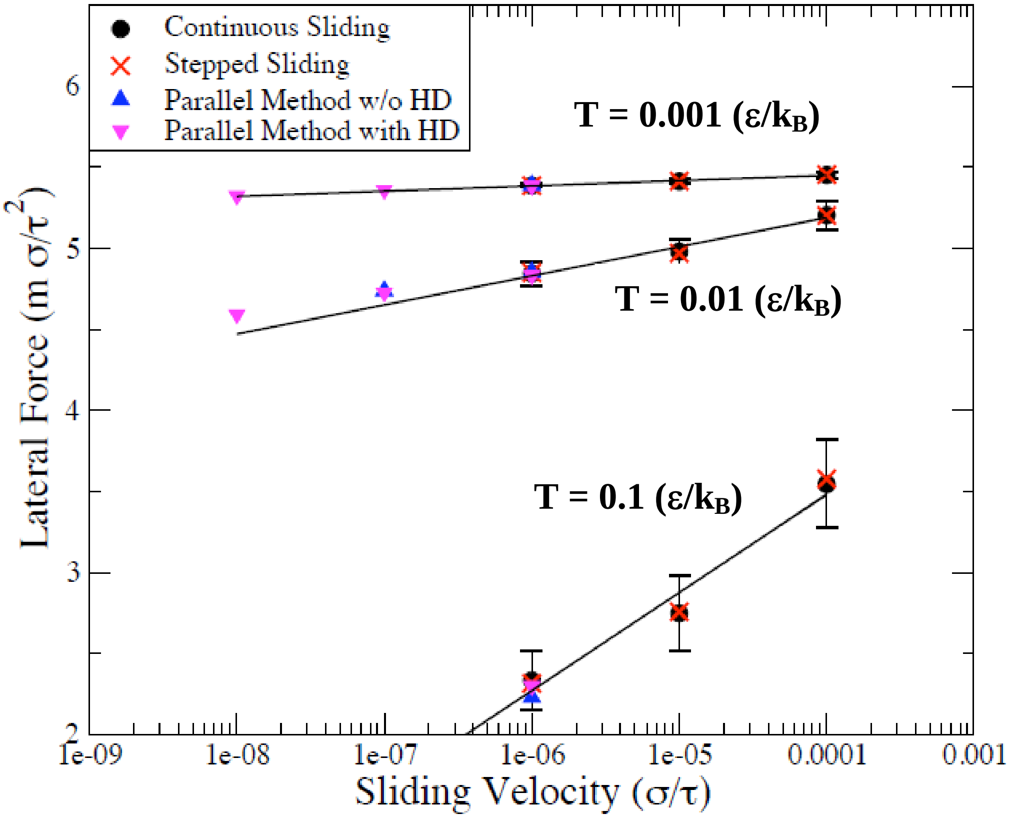

Figure 5.9 Lateral forces as functions of sliding velocity obtained from the 2-D model simulated at three different temperatures ($T = 0.001, 0.01, 0.1$) using four different methods. The straight trend lines and the error bars (the standard deviation) are obtained from the data of the continuous sliding simulations.

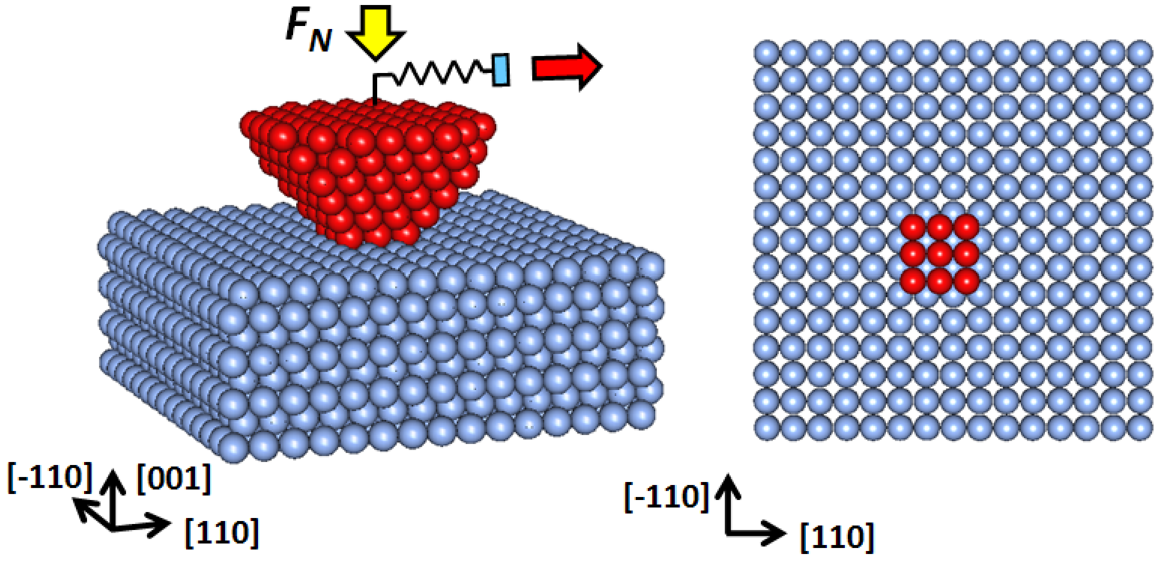

Figure 5.10 A diagram of a 3-dimensional AFM model consisting of a tip and a substrate. The atoms in the tip are shown in red, and the atoms in the substrate are shown in blue. The top layer of the tip is pulled by a spring moving in the sliding direction (the red arrow), and pushed by a normal force expressed as the yellow arrow.

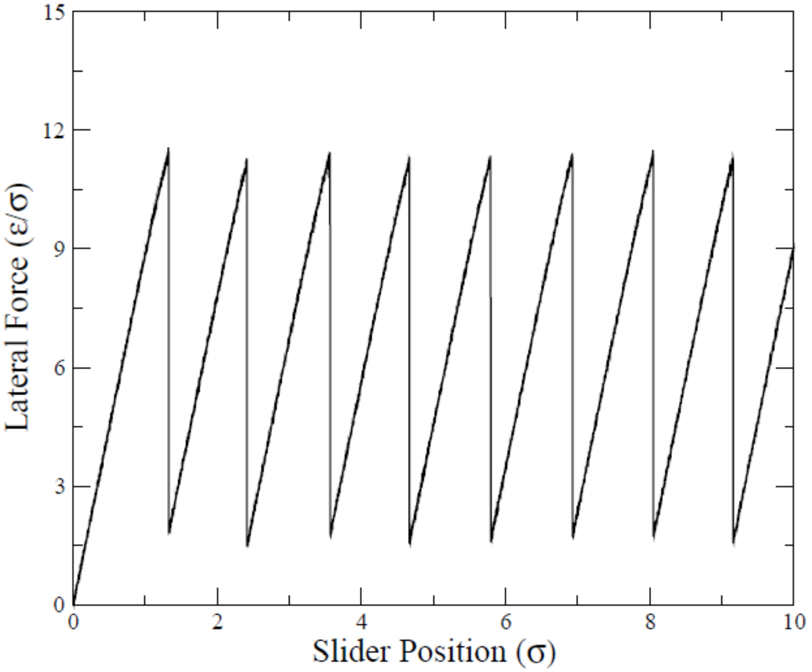

(a)

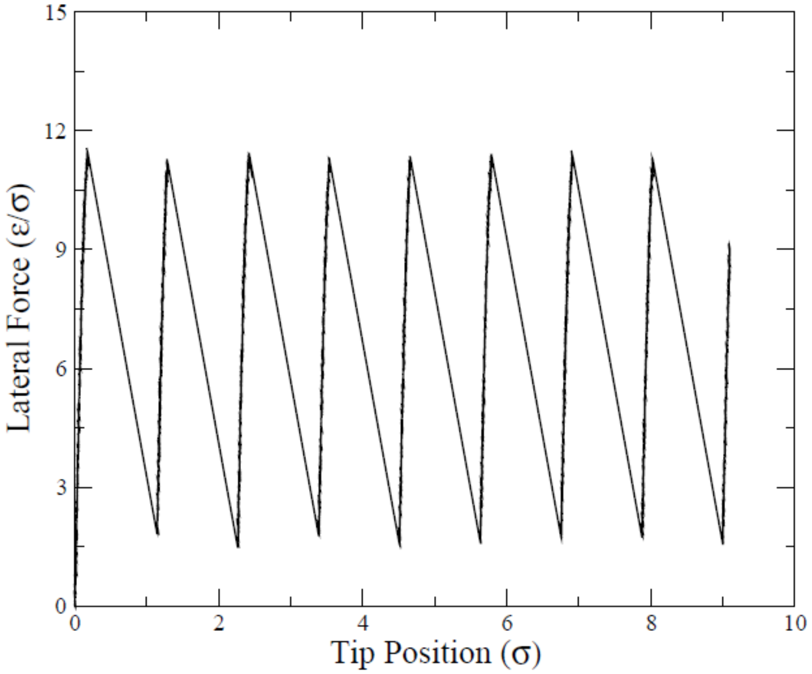

(b)

Figure 5.11 Lateral forces calculated from the 3-D model simulated at $v_S = 10^{-5}$ and $T = 0.01$. (a) Lateral force vs. slider position and (b) Lateral force vs. tip position.

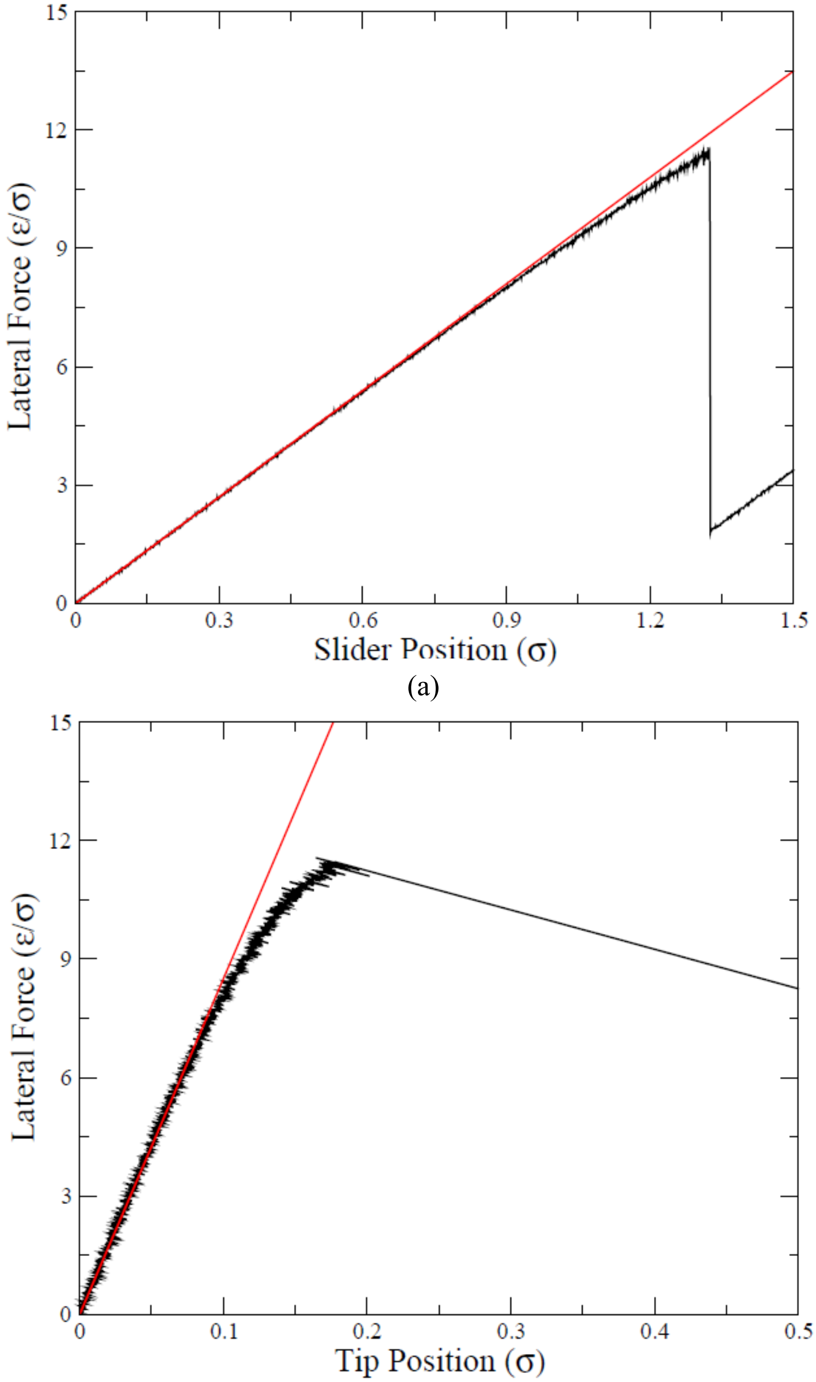

(a)

(b)

Figure 5.12 Lateral forces (black curves) calculated from the 3-D model simulated at $v_S = 10^{-5}$ and $T = 0.01$ and linear fittings (red straight line) extended from initially linear portion (a) Lateral force vs. slider position and (b) Lateral force vs. tip position.

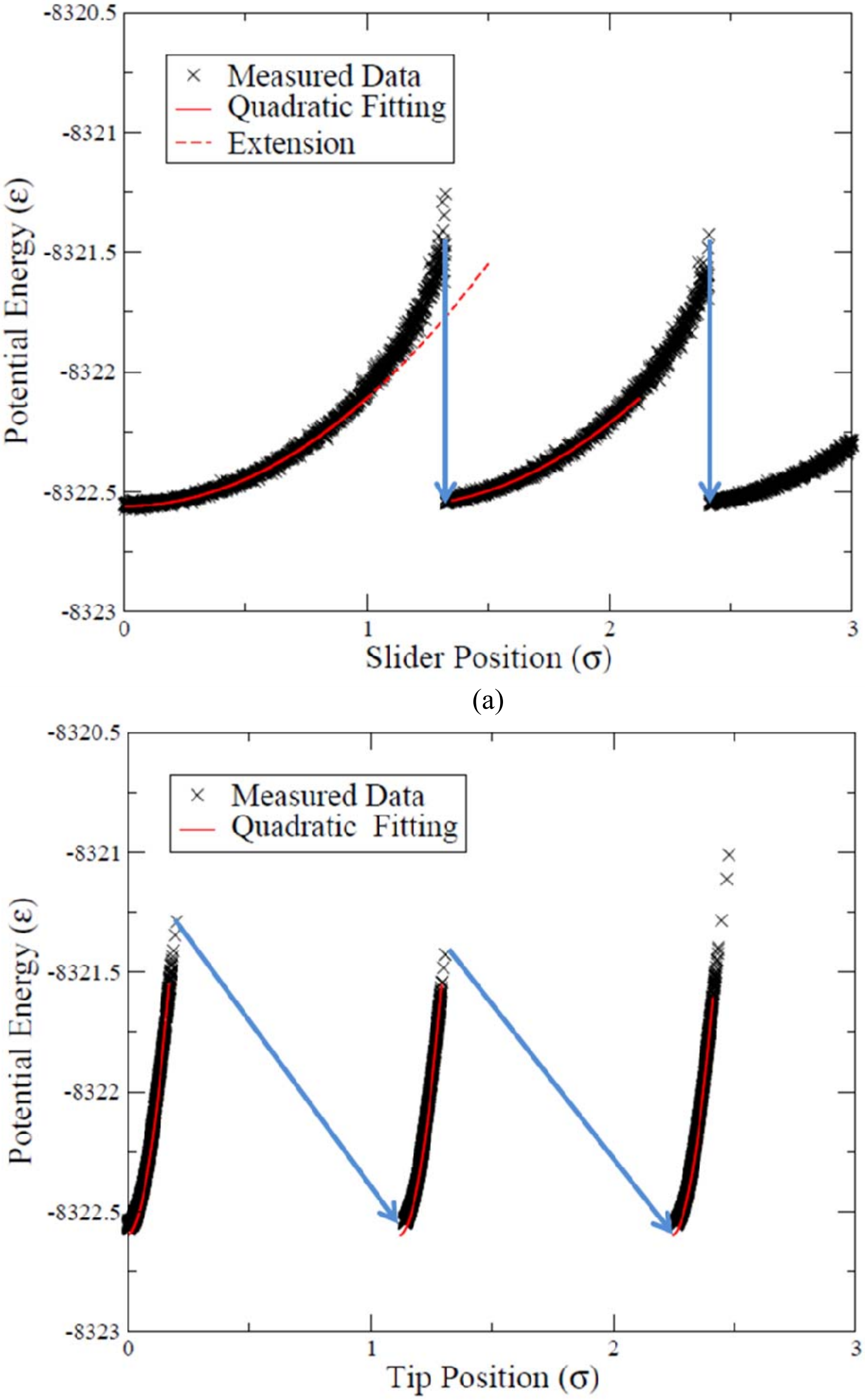

(a)

(b)

Figure 5.13 Potential energy curves (black curves) obtained from the 3-D model simulated at $v_S = 10^{-5}$ and $T = 0.01$, and quadratic fittings (red curves). The discontinuous points are connected by blue arrows. (a) Potential energy vs. slider position and (b) Potential energy vs. tip position. The blue arrows indicate transitions.

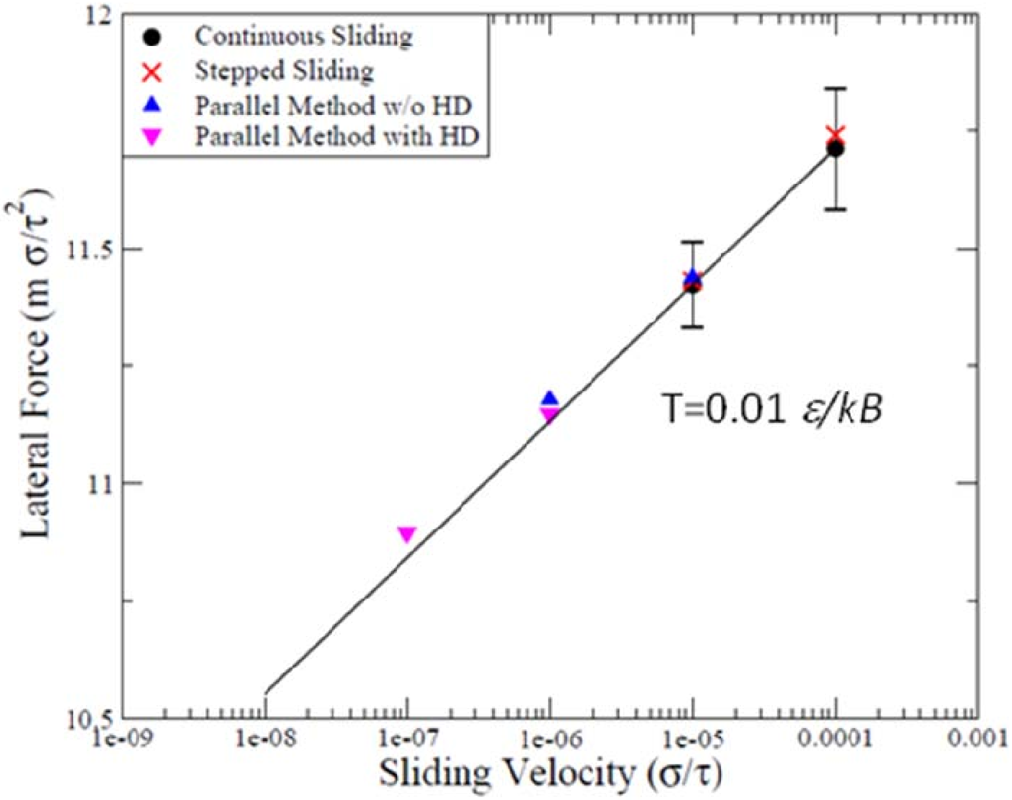

Figure 5.14 Lateral forces as functions of sliding velocity obtained from the 3-D model simulated at a temperatures of 0.01 using four different methods. The straight trend lines and the error bars (the standard deviation) are obtained from the data of the continuous sliding simulations.

References

[1] G. J. Martyna, M. L. Klein, and M. Tuckerman, "*Nose-Hoover Chains: The Canonical Ensemble via Continuous Dynamics*", J. Chem. Phys., 97, 2635 (1992).

[2] G. J. Martyna, M. E. Tuckerman, D. J. Tobias, and M. L. Klein, "*Explicit Reversible Integrators for Extended Systems Dynamics*", Mol. Phys., 87, 1117 (1996).

[3] E. Gnecco, R. Bennewitz, T. Gyalog, Ch. Loppacher, M. Bammerlin, E. Meyer, and H.-J. Güntherodt, "*Velocity Dependence of Atomic Friction*", Phys. Rev. Lett., 84, 1172 (2000).

[4] E. Riedo, E. Gnecco, R. Bennewitz, E. Meyer, and H. Brune, "*Interaction Potential and Hopping Dynamics Governing Sliding Friction*", Phys. Rev. Lett., 91, 084502 (2003).

CHAPTER VI

Friction between Incommensurate Surfaces

6.1 Introduction

Friction between two bare surfaces depends on the relative arrangement of atoms at the interface. If the contacting surfaces have the same crystalline pattern aligned in the same directions and their lattice parameters can be expressed as a ratio of two integers, the surfaces are commensurate and exhibit non-vanishing static friction which is proportional to the contact area. The 2-dimensional and 3-dimensional models studied in the previous chapter are the examples of commensurate surfaces. On the contrary, if there is no such periodicity, surfaces are incommensurate and their static friction becomes zero as the contact area increases. As shown in Fig. 6.1, two identical crystalline surfaces can easily be made incommensurate by rotating them relative to each other. Thus, unless we intentionally align the orientation of surfaces so as to have the identical orientation in the laboratory surfaces usually form incommensurate contacts.

Ultralow friction forces have been observed between incommensurate surfaces in nano scale experiments [2-4]. This phenomenon is termed superlubricity. A molecular dynamics simulation with rigid incommensurate walls exhibited similar behavior [5]. Incommensurate surfaces on a macro scale do not exhibit exceptionally low friction force.

It is hypothesized that this is due to “third bodies” such as hydrocarbons existing between the surfaces [6].

However, even clean incommensurate surfaces do not always show superlubricity. Socoliuc *et. al*. [4] observed a transition from the superlubricity regime (zero friction force) to the stick-slip regime (high friction force) by increasing the applied normal load. The surfaces, which exhibited vanishing force at low load, showed high friction force as the load increases. They explained this phenomenon with the relationship between the strength of the lateral atomic surface potential and the contact stiffness. As an analysis based on the one-dimensional Frenkel-Kontorova-Tomlinson (FKT) model [7] and a study using MD simulations [5] have pointed out, incommensurate surfaces can show large static friction if the atoms of one surface are weakly bound when compared to the interaction between the surfaces. Under these conditions the surface atoms can be rearranged into local energy minima with respect to the other surface.

In this chapter, we present MD simulation results performed with a 3-dimensional system modeling an AFM experiment involving incommensurate surfaces. The dependence of friction on the tip compliance and the normal load has been studied. The frictional behavior of a softer tip has been observed at different sliding velocities. We observe that the friction of incommensurate surfaces is a complicated phenomenon that involves emergence of several metastable states. In our simulations superlubricity breaks down with softer tips and at higher normal loads.

6.2 Simulation

The simulation system is illustrated in Fig. 6.2. The system models an AFM tip which consists of 263 atoms shown in red and a substrate which consists of 1800 atoms shown in blue. The substrate is an FCC crystal, and the tip is created by carving an FCC crystal, which has a larger lattice parameter than the substrate, into a cylindrical shape. The tip is also tapered slightly to the lower side and rotated by 8 degrees about the axis perpendicular to the contact surface. The tip and the substrate are joined in the [001] direction. The mismatch of lattice parameters and the rotation prevent the tip atoms from being arranged into the lattice points of the substrate when the tip atoms are more tightly bound than the interaction between the tip and the substrate.

A spring with a stiffness, $k = 10$, is linked to the top layer of the tip, which consists of atoms moving together without changing their relative positions, and pulls the tip as the other end of the spring (the slider) moves at a constant speed. All the quantities are expressed with the same units used in the previous chapter and omitted unless there is ambiguity. A normal force, F_N, is applied on the top layer of the tip, and the periodic boundary condition is used in the [110] and [-110] directions. As in Socoliuc's experiments [4], the magnitudes of the normal force are varied and we observe the dependence of superlubricity on the normal load. The atom positions on the bottom layer of the substrate are fixed to prevent a rigid-body translation in the vertical direction as we remove the periodic boundary condition in this direction.

The interaction between substrate atoms and the interaction between a substrate atom and a tip atom are modeled by the Lennard-Jones potential as expressed in Eq. (5-1), and the following parameters are used.

$$\begin{array}{ll} \sigma_{ss} = 1.0\,\sigma & \varepsilon_{ss} = 1.0\,\varepsilon \\ \sigma_{st} = 0.8\,\sigma & \varepsilon_{st} = 0.5\,\varepsilon \end{array} , \qquad (s\text{: substrate, } t\text{: tip})$$

Because we test very small tip stiffnesses, any potential allowing bond breaking may result in plastic deformation of the tip. To preserve the tip shape, we used the harmonic potential as in Eq. (5-7) for the interaction between tip atoms. The tip compliances are varied by changing the spring constant of the harmonic potential.

All the simulations have been performed at one temperature point (T = 0.01) and temperature is controlled by a variant of the Nose-Hoover thermostat [8]. All the atoms except in the bottom layer of the substrate and the top layer of the tip are subject to the thermostat. With the softest tip we prepared, the velocity dependence was tested at three sliding velocities ($v_S = 10^{-4}$, 10^{-5}, 10^{-6}). The parallel method was used to simulate the lowest sliding velocity (10^{-6}), but we were unable to apply the hyperdynamics methodology for the reasons we will discuss in this chapter. The equations of motion are numerically integrated using a modified Velocity-Verlet algorithm [9].

6.3 Result

We first observed the dependence of the friction force on the tip stiffness by changing the spring constant between the tip atoms. The friction force (or the lateral force) is measured by the deformation of the spring as in the AFM experiment. Fig. 6.2 (b) shows the initial interface configurations with a rigid tip and a softer tip. When the tip atoms are more strongly bound than the interaction between the tip and the substrate (a rigid tip), they maintain their original crystalline configuration as shown in the left of Fig. 6.2 (b), where the orientation of the tip is also clearly evident. As the tip becomes softer, the tip atoms contacting the substrate are rearranged into the lattice point of the substrate as seen in the right of Fig. 6.2 (b). Thus, we can expect that the lateral force will increase as the tip gets softer.

Fig. 6.3 (a) and (b) shows the friction forces measured during sliding as functions of the slider position with various stiffnesses. All the simulations were performed at F_N=5.0. We can observe that the softer tips experience a larger lateral force at each transition than the tips with higher stiffnesses. Moreover, while rigid tips show relatively uniform transitions and their lateral forces oscillate around zero, the softer tips display irregular transitions and their lateral forces remain positive after transitions. When $k <= 10$ as in Fig. 6.3 (a), the graph shows small drops in the lateral force in addition to major decreases. On the contrary, the tip with $k = 57.2$ does not show such behavior.

To check the system-to-system variation, we simulated ten samples with different initial conditions. With the same stiffness value, all samples showed a similar trend. The lateral force is averaged over the slider position. For a rigid tip (k = 57.2), the average friction forces range from 0.08 to 0.1 among the samples while a softer tip (k = 3.81) shows a larger variation from 7.34 ~ 8.53.

Fig. 6.4 shows the average lateral forces as a function of the stiffness. Instead of exhibiting monotonically increasing force with decreasing stiffness, we see an abrupt increase around a stiffness of 5. The regime with the stiffness larger than 5 corresponds to superlubric friction due to incommensurate surfaces.

At the stiffnesses of $k = 10.0$, 15.0, 25.0, 57.2, we increased the normal load F_N up to 100.0 to observe the normal force dependence of the system. All the simulations with these stiffnesses at the normal load of F_N=5.0 showed vanishing friction forces. Fig. 6.5 shows the lateral force vs. the slider position graphs at $k = 10.0$, 15.0, 25.0, 57.2 and at different normal loads. At the stiffness of $k = 10.0$ (Fig. 6.5 (a)), larger friction forces are observed as the normal force increases. The existence of metastable states at higher normal loads can still be noticed by observing the small drops in the lateral force curves. At the stiffnesses of $k = 15.0$ and 25.0 (Fig. 6.5 (b) and (c)), the lateral forces still fluctuate around zero, but their behaviors become non-uniform and exhibit multiple large drops as the normal force increases. In fig. 6.5 (d) at the stiffness of $k = 57.2$, the lateral force curves show no change regardless of the magnitude of the normal load. Fig. 6.6 shows the average lateral forces as a function of the normal load. It is clear that the superlubricity breaks down as the normal load increases at $k = 10.0$ although this transition is not observed at other stiffness values. The data at $k = 10.0$ was fit to a formula shown in Eq. (3-47) assuming the energy barrier E_O has a linear dependence on the normal load.

$$\overline{F} \sim C_1 \, F_N \exp[C_2 \, F_N] \quad , \tag{6-1}$$

where C_1 and C_2 are fitting parameters. The fitting curve is shown as a dashed curve in Fig. 6.6.

To investigate the frictional behavior of soft tips in more detail, we have performed further simulations with the softest tip (k = 3.81) by reducing the sliding velocity. Fig. 6.7 shows lateral forces as functions of slider position at three different sliding velocities ($v_S = 10^{-4}, 10^{-5}, 10^{-6}$). While the highest velocity results show the sporadic distributions of the transition forces, the lower velocity results display the relatively uniform transitions. Fig. 6.8 shows details of transitions at $v_S = 10^{-4}$ and $v_S = 10^{-5}$. Although the transitions at lower sliding velocity appear uniform, the transition to slip is not a single step of transition. The system passes through several intermediate states shown in Fig. 6.8 (b). These states are similar at each transition. In most cases, two or three tip atoms in the right row are relocated into new sites in the sliding direction, and then the others follow resulting in a major slip motion. On the contrary, at higher sliding velocity ($v_S = 10^{-4}$), the system undergoes a transition through many complicated mechanisms including the local shear inside the tip shown in Fig. 6.8 (a), and the mechanisms are different at each transition.

Further analysis reveals that even in the stick phase where the tip deforms elastically the tip atoms at the interface continually change their configurations among several metastable states. Because these metastable states do not accompany a noticeable change in the location of the tip position, there is no significant change in the lateral force. We found these states by performing a potential energy minimization using the FIRE scheme [10]. The 8 identified metastable configurations are shown in Fig. 6.9, where only interface (the top layer of the substrate and the bottom layer of the tip) atoms are presented. Fig. 6.10 shows the potential energy differences of each of these states from the value of the #1 state as functions of slider position. Because not all the states are stable at all slider positions, the curves are not complete and appear only when a stable state was identified.

Initially, the #1 state is the most stable state and there is only one metastable state (#2). Starting from at a slider position of 0.33, other metastable states start to appear, and after a slider reaches 0.52, the #2 state become more stable. Eventually, the states branching off from the #2 state (#3, #4, #7) become more stable than the states from the #1 state (#5, #6). After a slider position of 1.44, the #8 state, an intermediate state through which the system passes in a major transition, becomes most stable. The probability for major transitions increases as the energy of state 8 approaches that of state 2.

The time scale for transitions among these metastable states is much shorter than the time scale related to the major transition. Thus, the system continually changes interface configuration amongst the metastable states prior to making a major transition.

6.4 Discussion

Difficulties arise from the existence of multiple low energy barriers when we attempt to apply the hyperdynamics methodology in simulating this system. Fig. 6.8 (a) illustrates a potential energy well. Suppose that this well has multiple energy barriers and all the barriers are large so that the transitions through these barriers are all rare events. By introducing a biased potential which reduces all the energy barriers by the same amount, we can accelerate the escape from this well preserving the relative transition probabilities through the energy barriers. However, in a system with incommensurate surfaces a different situation arises. A simple example is shown in Fig. 6.8 (b), where two wells are separated by a smaller energy barrier, but these two wells are surrounded by larger barriers. As observed in the simulations with incommensurate surfaces, the system hops frequently back and forth between these small wells. As we apply a biased potential to accelerate the escape from a single well, the biased potentials for this system will be the ones shown in Fig. 6.8 (b). Then, the boost factor of the biased potential will be small because the average escape time of the original potential is not large. In fact, we do not need to accelerate the escape from the small wells. They occur without the aid of biased potentials. Moreover, we cannot accelerate these events with a boost factor without introducing systematic errors. Thus, the simulations of incommensurate surfaces at lower sliding velocities require long running time even when we apply the hyperdynamics scheme. If we could identify when a transition occurs between two wells more than once within a critical time window (a criterion for determining rare events), a biased potential as illustrated in Fig. 6.8 (c) could be applied to make the simulation more efficient. The construction and application of this type of bias potential remain as a future work.

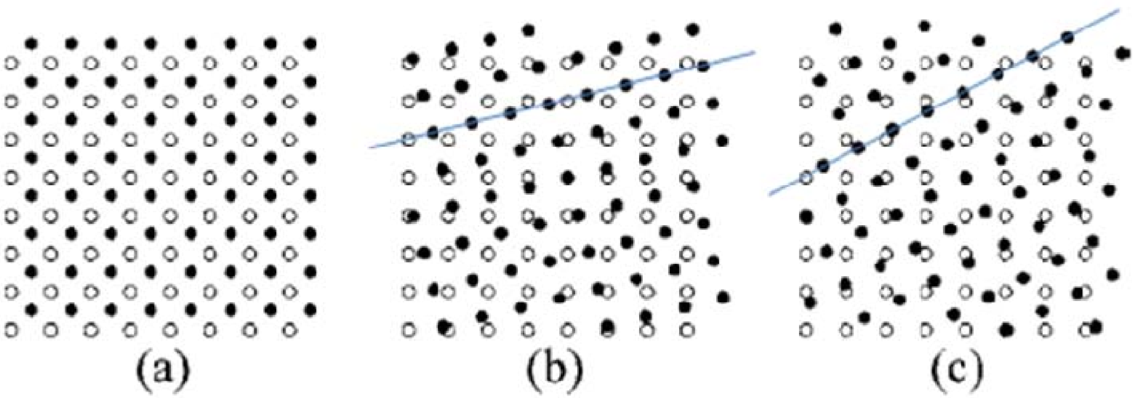

Figure 6.1 Two surfaces contacting each other. The surface consisting of the black atoms are on the top of the surface of the white atoms. (a) The two surfaces are commensurate and the atoms on the top surface are arranged into the center of the four lattice points of the bottom surface. (b) and (c) The top surface is rotated about an axis perpendicular to the bottom surface, and each atom on the top surface is in different configurations [1].

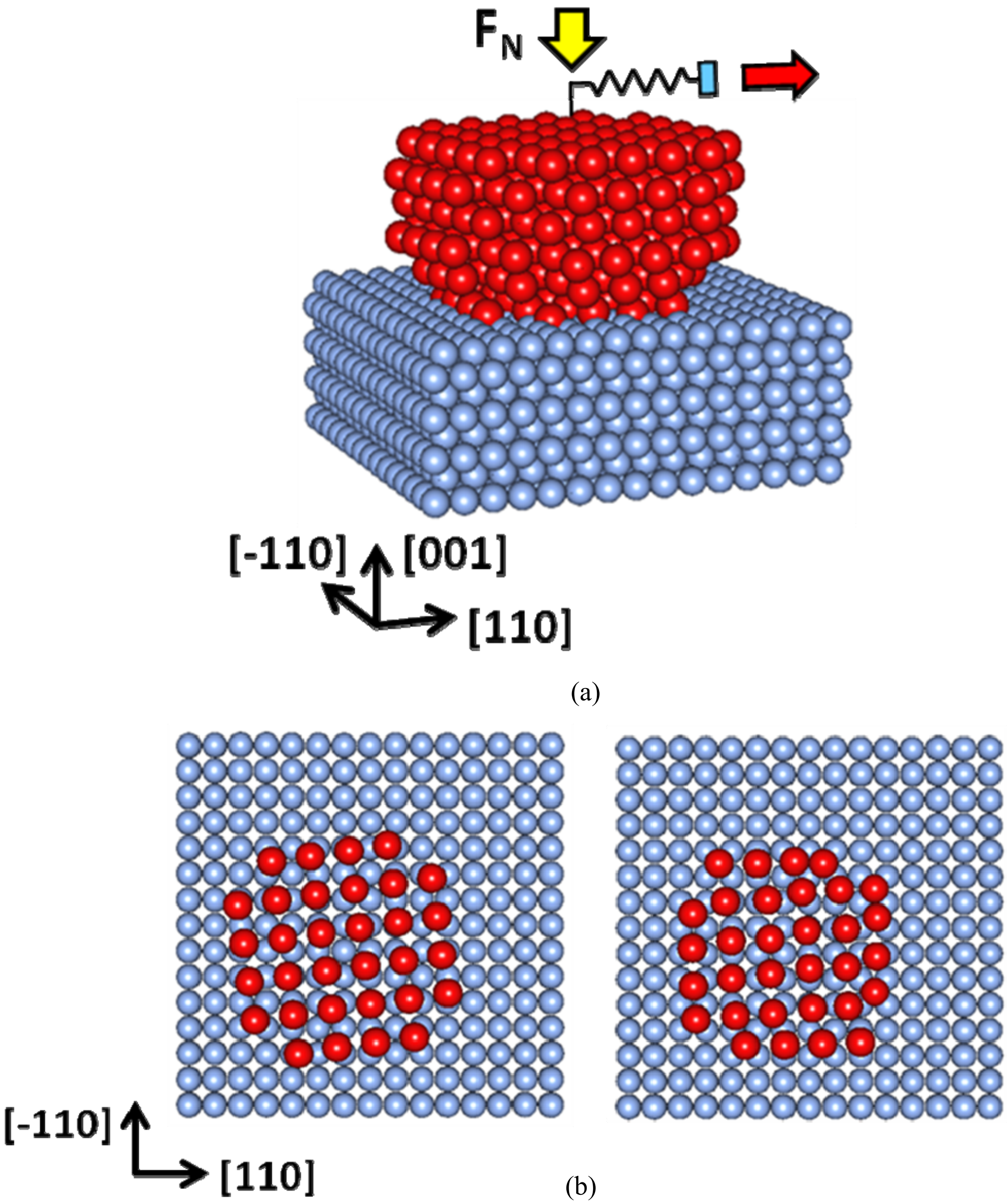

Figure 6.2 A diagram of a 3-dimensional AFM model with a tip and a substrate. The tip atoms are shown in red and the substrate atoms are shown in blue. (a) A 3-D perspective. (b) The configuration of atoms at the interface between the bottom layer of the tip and the top layer of the substrate. The left configuration is from a rigid tip and the right configuration is from a softer tip.

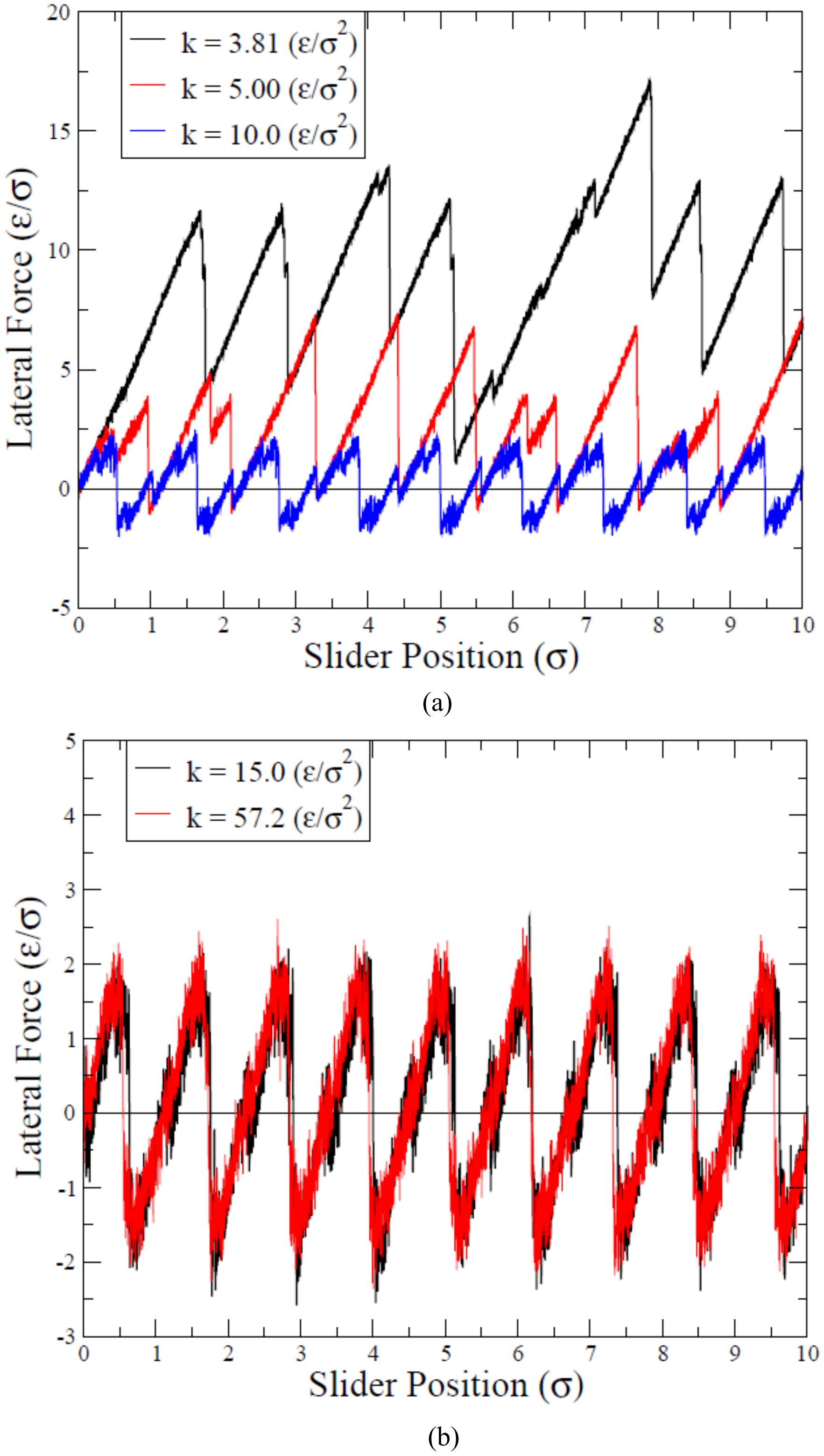

Figure 6.3 Lateral force vs. slider position at different stiffnesses. All the simulations were performed at F_N =5.0. (a) k = 3.81, 5.0, 10.0 (ε/σ^2) (b) k = 15.0, 57.2 (ε/σ^2).

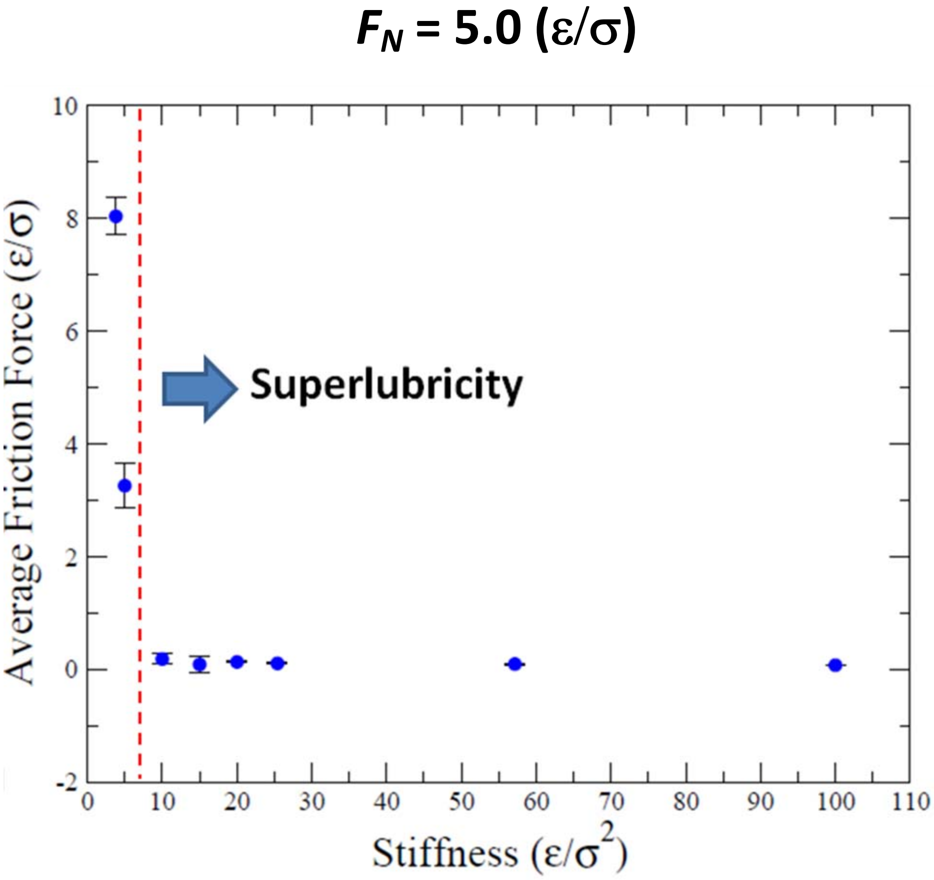

Figure 6.4 The relationship between the average lateral force and the tip stiffness. The graph shows two distinct regimes divided by the red dashed line. When the tip stiffness is larger than a critical value (~7) indicated by the red line, almost vanishing average friction force is observed (superlubricity). When the stiffness is smaller than the critical value, it shows very high force. . The error bars show the standard deviation of the samples.

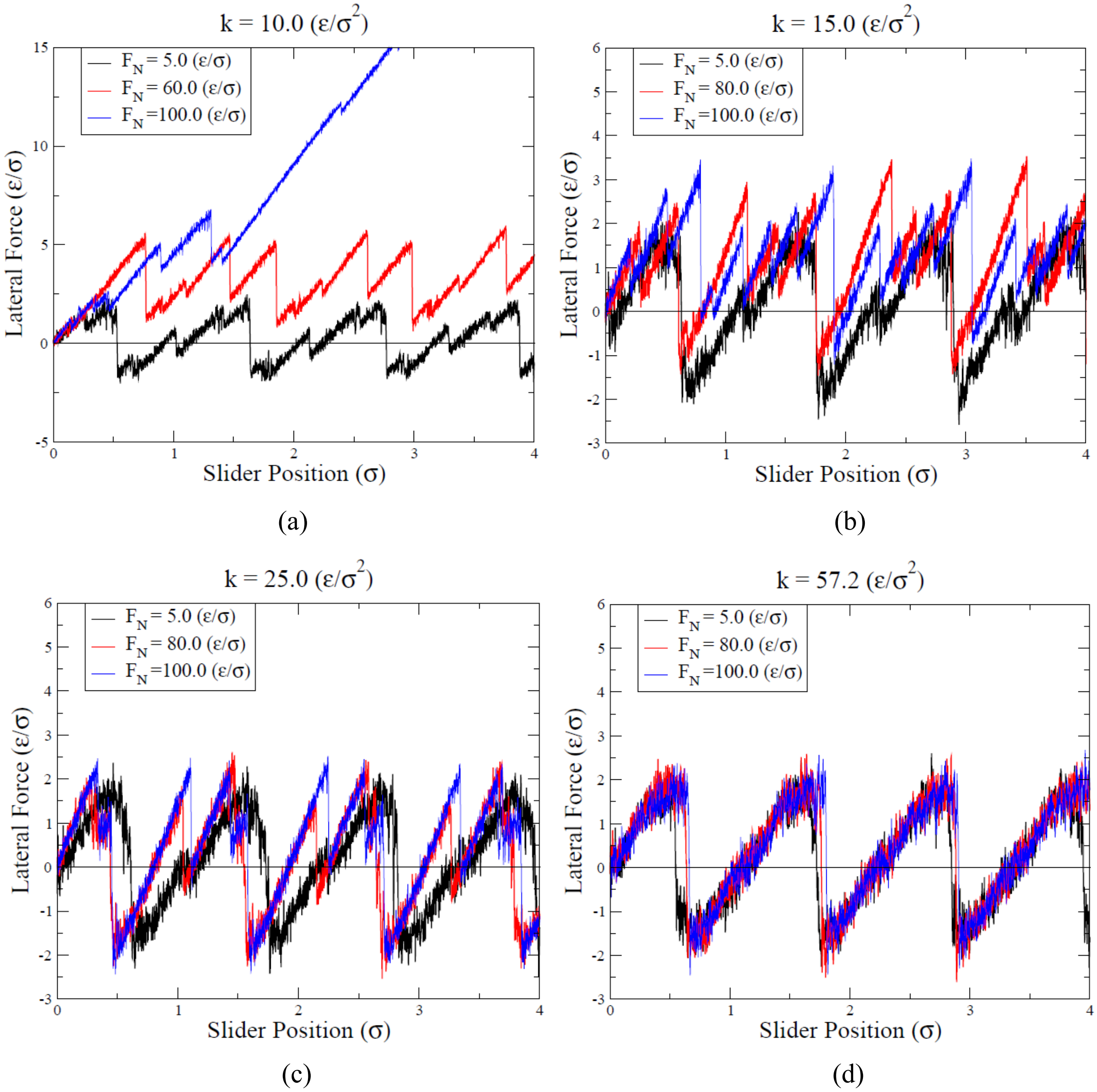

Figure 6.5 Lateral force vs. slider position at different stiffnesses and different normal loads. (a) k = 10.0 (F_N =5.0, 60.0, 100.0) (b) k = 15.0 (F_N =5.0, 80.0, 100.0) (c) k = 25.0 (F_N =5.0, 80.0, 100.0) (d) k = 57.2 (F_N =5.0, 80.0, 100.0).

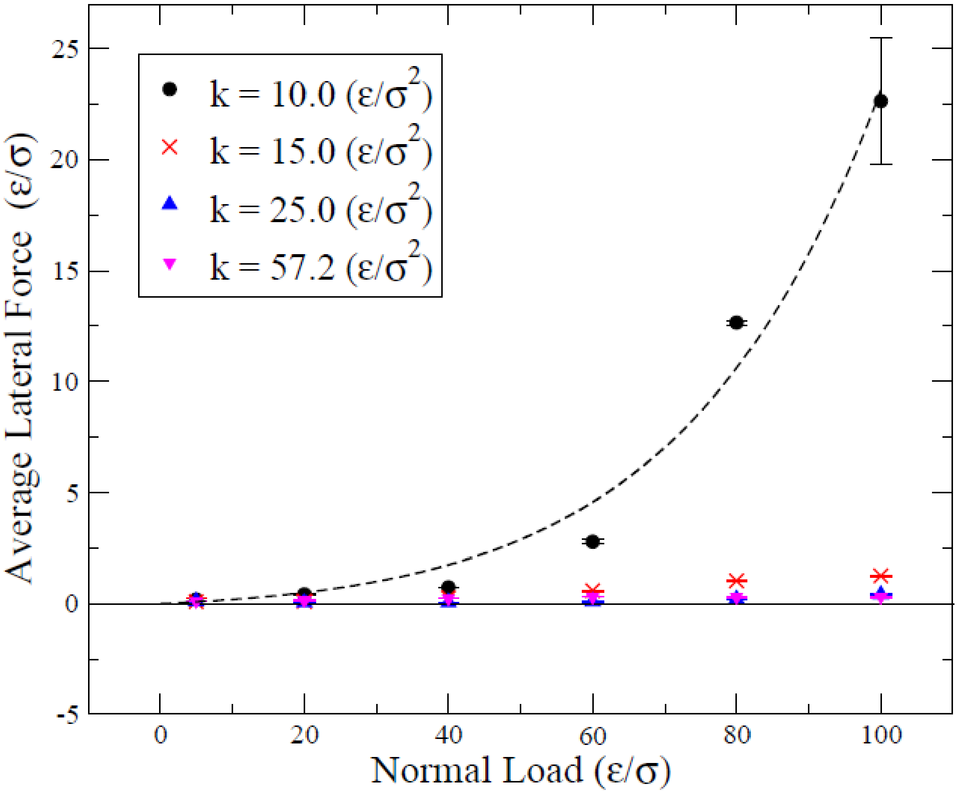

Figure 6.6 The relationship between the average lateral force and the applied normal load obtained from the simulations with four different tip stiffnesses (k = 10, 15, 25, 57.2). The dashed curve is a fit to the data at k = 10 ($\overline{F} \sim 0.0143 F_N \exp(0.0278 F_N)$).

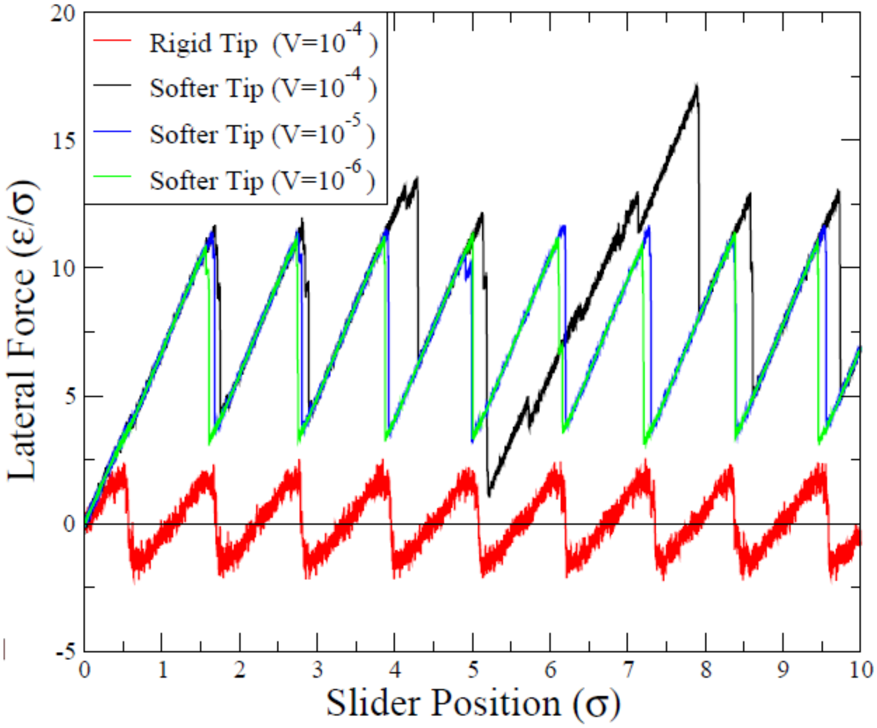

Figure 6.7 Lateral Force vs. slider position at different sliding velocities with a rigid tip (k = 57.2) and a softer tip (k = 3.81).

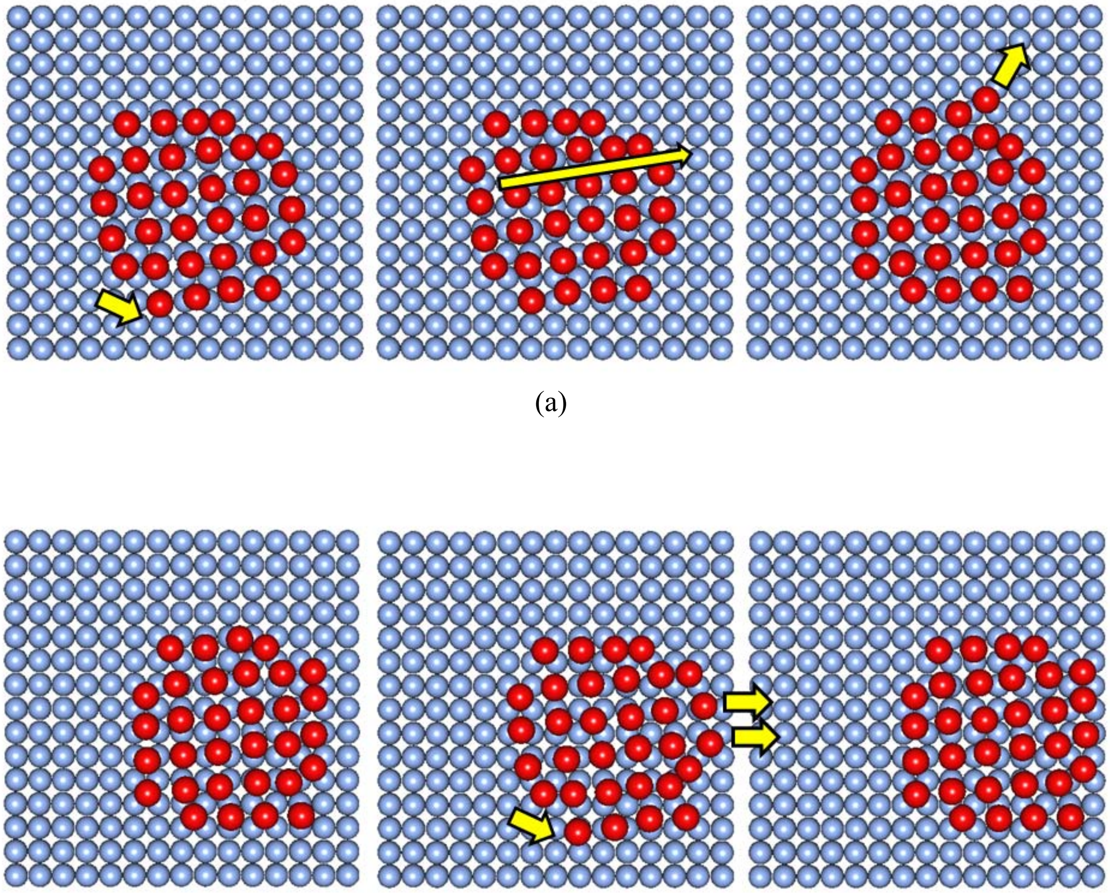

(a)

(b)

Figure 6.8 Intermediate states the tip passes when making a major transition. (a) v_S = 10^{-4} and (b) v_S = 10^{-5} .

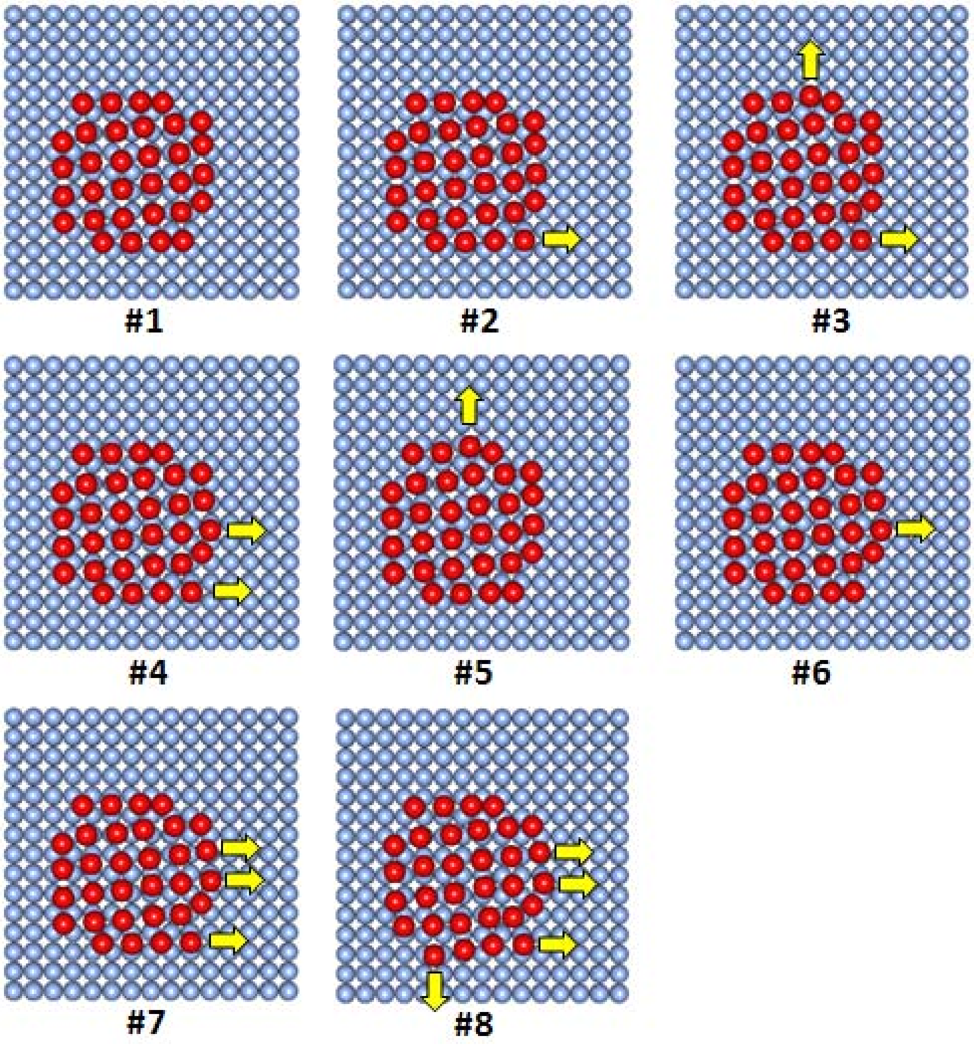

Figure 6.9 The metastable states among which the system hops prior to making a transition. Only the two layers at the interface are shown. The yellow arrows indicate the shifts of the atoms relative to the #1 state. The #8 state is one of the intermediate states the system passes when making a major transition.

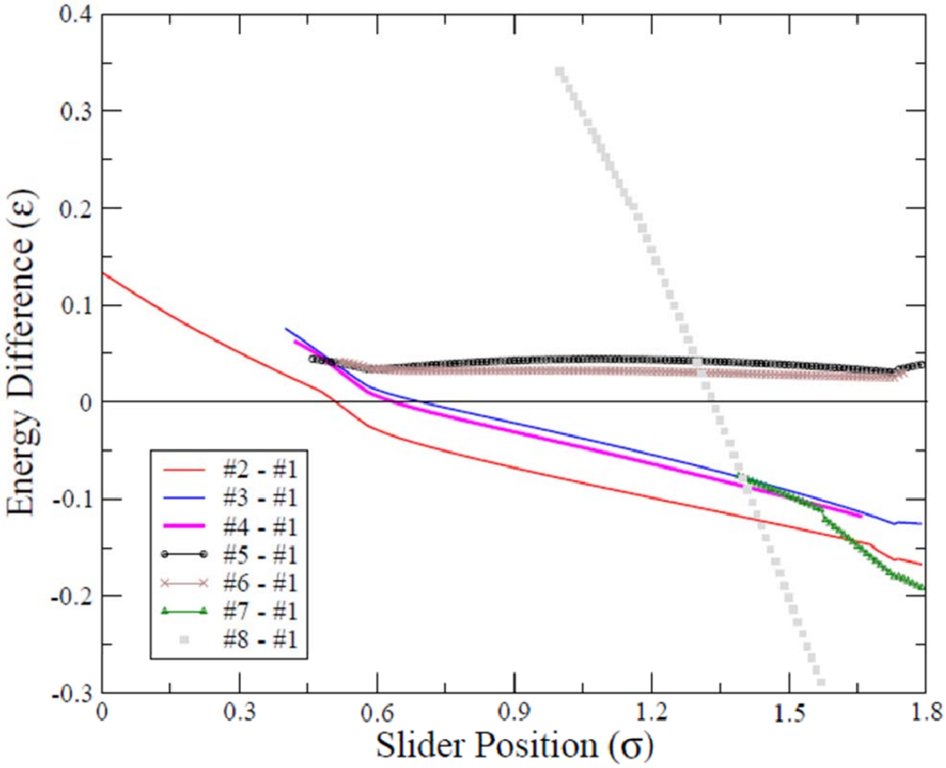

Figure 6.10 The energy differences between the metastable states from the #1 state energy as functions of the slider position.

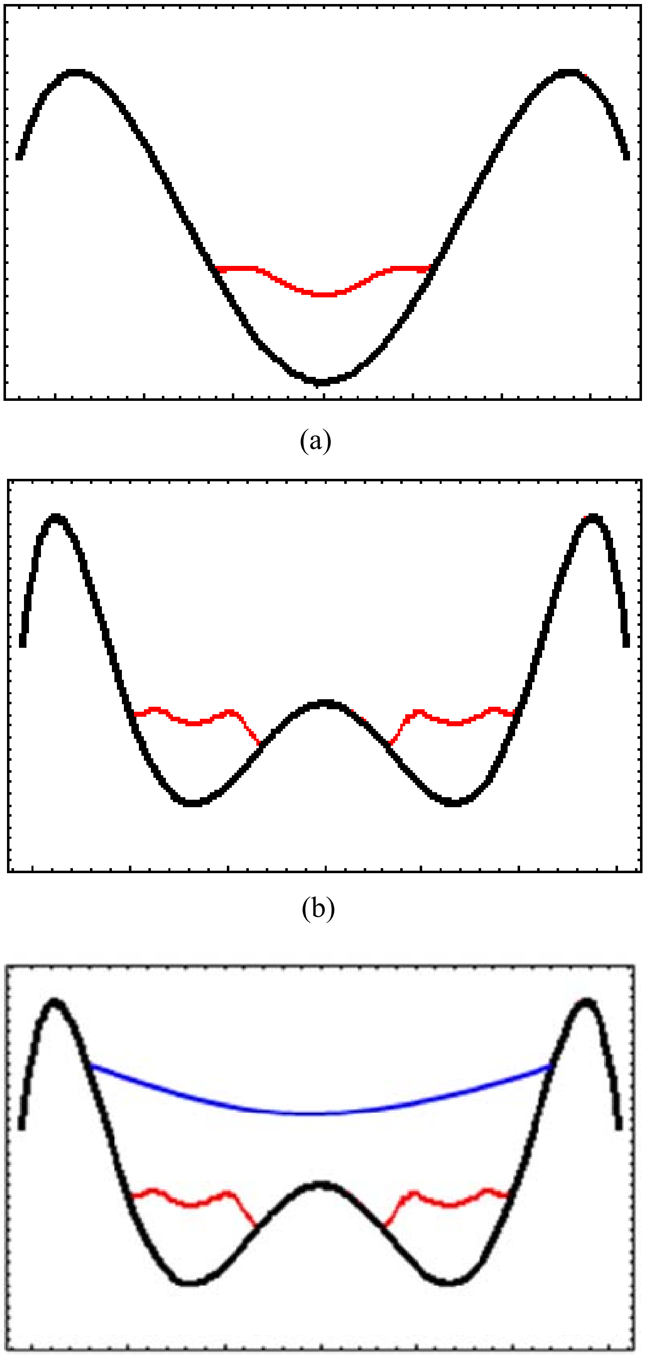

(a)

(b)

(c)

Figure 6.11 Illustrations of the various situations in which hyperdynamics is applied to an incommensurate surface. (a) Single well with higher energy barrier (b) A large well with two small sub wells. The small wells are separated by small energy barrier. (c) Ideal biased potential (the blue curve) for the system in (b).

References

[1] J. Ringlein and M. O. Robbins, "*Understanding and Illustrating the Atomic Origins of Friction*", Am. J. Phys., 72, 884 (2004).

[2] M. Hirano, K. Shinjo, R. Kaneko, and Y. Murata, "*Anisotropy of Frictional Forces in Muscovite Mica*", Phys. Rev. Lett., 67, 2642 (1991)

[3] M. Dienwiebel, G. S. Verhoeven, N. Pradeep, J. W. M. Frenken, J. A. Heimberg, and H. W. Zandbergen, " *Superlubricity of Graphite*", Phys. Rev. Lett., 92, 126101 (2004).

[4] A. Socoliuc, R. Bennewitz, E. Gnecco, and E. Meyer, "*Transition from Stick-Slip to Continuous Sliding in Atomic Friction: Entering a New Regime of Ultralow Friction*", Phys. Rev. Lett., 92, 134301 (2004).

[5] M. H. Müser and M. O. Robbin, "*Conditions for Static Friction between Flat Crystalline Surfaces*", Phys. Rev. B, 61, 2335 (2000).

[6] G. He, M. H. Müser, and M. O. Robbins, "*Adsorbed Layers and the Origin of Static Friction*", Science, 284, 1650 (1999).

[7] M. Weiss and F.-J. Elmer, "*Dry Friction in the Frenkel-Kontorova-Tomlinson Model: Static Properties*", Phys. Rev. B, 61, 2335 (2000).

[8] G. J. Martyna, M. L. Klein, and M. Tuckerman, "*Nose-Hoover Chains: The Canonical Ensemble via Continuous Dynamics*", J. Chem. Phys., 97, 2635 (1992).

[9] G. J. Martyna, M. E. Tuckerman, D. J. Tobias, and M. L. Klein, "*Explicit Reversible Integrators for Extended Systems Dynamics*", Mol. Phys., 87, 1117 (1996).

[10] E. Bitzek, P. Koskinen, F. Gähler, M. Moseler, and P. Gumbsch, "*Structural Relaxation Made Simple*", Phys. Rev. Lett., 97, 170201 (2006).

CHAPTER VII

Friction between Amorphous Silica Surfaces

7.1 Introduction

Silicon is the second most abundant element (after oxygen) in the earth's crust and the most widely used material for micro/nano electro-mechanical systems (MEMS/NEMS) because of its economy, compatibility with integrated-circuit technology and many advantageous mechanical properties such as fatigue resistance [1]. Moreover, polycrystalline silicon can be fabricated into complex, micro-scale structures using surface micromachining based on selective etching of multilayered films [2].

One of the current problems with MEMS/NEMS is the treatment of contacting surfaces. The performance and fabrication of MEMS/NEMS devices shows significant dependence on adhesion and friction mainly due to their large surface-to-volume ratios. Because of these problems, MEMS/NEMS devices with sliding interfaces in rotary and linear motion (Fig. 7.1) have not been marketed [3]. Therefore, the triobological properties of silicon surfaces have been widely investigated.

Recently, an AFM experiment with a silicon tip and a silicon surface with oxidized layers revealed interesting relationships between friction force and sliding velocity with nontrivial temperature dependences [4]. For temperatures below approximately 150 K, the frictional force showed the typical logarithmic dependence, but above 150 K the frictional force had no apparent dependence on the sliding velocity. Moreover, the researchers observed that as temperature decreases the friction coefficient exhibits a peak around 100 K and a subsequent drop instead of a monotonic increase.

One possible explanation of this behavior arises from a statistical analysis of experimental data by Evstigneev *et. al*. [5] in which they hypothesized that the transitions of sliding systems with nanometer scale contacts can occur through multiple mechanisms and the dominant mechanism depends on both temperature and sliding rate. As one candidate mechanism they proposed the formation of new bonds at the interface of the tip and the substrate during stick-phase biasing the friction force.

Currently there does not exist any clear demonstration of which mechanisms are actually present at various temperatures and sliding rates and the resulting affects on friction. In order to determine these mechanisms and explain the origin of characteristic temperature and sliding rate dependences, we model an AFM experiment with oxidized silicon surfaces using a molecular dynamics methodology.

In the subsequent chapter we first present the potential energy function we use for the silica simulations. Sec. 7.3 contains the details of sliding simulations with bare silicon surfaces and cylindrical tips. Sec. 7.4 details the effects of oxide layers on friction comparing results from several models with bare and oxidized surfaces. These sliding simulations are performed at high sliding velocities. Finally, in Sec. 7.5 we describe simulation results at sliding rates close to experiments achieved using hyperdynamics with a bond-boost potential.

7.2 Silicon and Silica Potentials

As silicon and silica are the most widely used industrial materials, a myriad of potentials for silicon and silica have been proposed. Stillinger-Weber (SW) [6], Tersoff [7], and the Environment-Dependent Interatomic Potential (EDIP) [8] are commonly used to model silicon, and TTAM [9], BKS [10], Feuston and Garifolini [11], Vashishta [12], and Huang and Kieffer [13] for have been developed for silica. Some potential functions have three body terms to treat covalent bonding properly [6, 11, 12, 13], others include coordination dependent terms [7, 8, 13] and others use a charge transfer function to consider charge redistribution during bond formation and breaking [13]. However, potential functions which can treat both silicon and silica simultaneously are rare. The extended Stillinger-Weber potential developed by Watanabe [14] is one such potential.

Most of the silica potentials have a Coulomb interaction term that models the effective charges of silicon and oxygen atoms. The Coulomb interaction presents particular challenges for molecular dynamics simulation because is long-ranged and does not converge within typical short-range cut-off lengths [15]. Convergence is typically achieved by employing a conventional Ewald summation method, but this method is very time-consuming. The Watanabe potential does not explicitly include the Coulomb interaction terms, and all the interactions are modeled by short-ranged pair interactions and three-body interactions as in the SW potential. Long-ranged interactions are incorporated into the coordination-dependent Si-O pair interaction term and the three-body term. The function form is expressed as

$$\Phi = \sum_{i} \sum_{j>i} f_2(\vec{r}_i, \vec{r}_i) + \sum_{i} \sum_{j>i} \sum_{k>j} f_3(\vec{r}_i, \vec{r}_j, \vec{r}_k) \quad , \qquad (7\text{-}1)$$

where,

$$f_2(\vec{r}_i, \vec{r}_j) = g_{ij} A_{ij} (B_{ij} r_{ij}^{-p_{ij}} - r_{ij}^{-q_{ij}}) \exp[(r_{ij} - a_{ij})^{-1}] \quad , \tag{7-2}$$

$$f_3(\vec{r}_i, \vec{r}_j, \vec{r}_k) = h(r_{ij}, r_{ik}, \theta_{jik}) + h(r_{ji}, r_{jk}, \theta_{ijk}) + h(r_{ki}, r_{kj}, \theta_{jki}) \quad , \tag{7-3}$$

and

$$h(r_{ij}, r_{ik}, \theta_{jik}) = \lambda_{jik} \exp[\gamma_{ij}^{jik} (r_{ij} - a_{ij}^{jik})^{-1} + \gamma_{ik}^{jik} (r_{ik} - a_{ik}^{jik})^{-1}] (\cos\theta_{jik} - \cos\theta_{jik}^{\mathrm{O}})^2 . \tag{7-4}$$

Here *A, B, p, q, a, λ, γ, θ* are parameters that depend on the atom types. g_{ij} shown in the two body terms of Eq. (7-2) is introduced to treat the coordination number of oxygen. It becomes 1 in Si-Si and O-O interactions, and in the case of Si-O interaction it depends on the coordination number of O. In this case g_{ij} is a function of *z*, the number of neighboring Si atoms. To calculate z, a cut-off function f_C is used as follows.

$$z = \sum_{j \in Si} f_C(r_j) \quad , \tag{7-5}$$

where r_j is the distance from O to a neighboring Si and

$$f_C(r_j) = \begin{cases} 1 \quad \text{if } r_j < 2.51\,\mathring{\mathrm{A}} \\ \text{continuously changes from 1 to 0} \quad \text{if } 2.51\,\mathring{\mathrm{A}} \le r_j \le 2.93\,\mathring{\mathrm{A}} \\ 0 \quad \text{if } r_j > 2.93\,\mathring{\mathrm{A}} \end{cases} .$$

A proper functional form was chosen to make –z *g*(z) have minimum when z = 2 (Fig. 7.2).

$$g(z) = \frac{m_1}{\exp[(m_2 - z)/m_3] + 1} \exp[m_4 (z - m_5)^2] \ . \tag{7-6}$$

As a result, an oxygen atom is most stable when it has two neighboring silicon atoms. The parameters which appear in the two and three body terms are chosen by performing a best fit the *ab initio* calculations as shown in Fig. 7.3.

Because this potential can treat both silicon and silica, it has advantages for modeling an oxide film developed on a crystalline silicon surface. Using this potential Watanabe *et. al*. constructed oxide films by layer-by-layer insertion of oxygen atoms and found structural features that agree with the experimental results [14].

7.3 Simulations of Bare Silicon surfaces

In this section, we present simulation results of sliding contact between bare silicon surfaces using the SW potential.

7.3.1 Surface Reconstruction

When silicon is cleaved, the atoms in the exposed surfaces rearrange to minimize their surface energies. Silicon atoms on the (001) surface dimerize. It has been known that the Stillinger-Weber model can reproduce this process [16], and the more complex surface reconstructions in (111) direction with modified parameters [17]. Our friction simulation is done using a silicon (001) surface, so we began by simulating the reconstruction of the surface. The results are shown in Fig. 7.4. The surface atoms are colored differently for better visualization. In the friction simulation, dimerized surfaces are used.

7.3.2 Friction Simulation

The sliding simulations between two flat silicon surfaces dimerized in (001) direction were performed with cylindrical tips. The surfaces consist of only silicon atoms. The purpose of the simulations is to measure the frictional force of the bare silicon surfaces and to model the effect of the relative orientation between the dimerized surfaces. We used four differently oriented tips with a fixed substrate (0^o, 30^o, 60^o, 90^o)□. The models with 0^o and 30^o orientation are shown in Fig. 7.5. During the simulation we maintained a normal force = 8.3 nN, a sliding velocity = 38.5 m/sec, and temperatures = 25K and 250K. The lateral forces as the functions of time are shown in Fig. 7.6. Many silicon atoms which comprised the tip were lost during the sliding (wear) as shown in Fig. 7.5. Significant wear was observed in all the orientations although the relative number of the lost particles depends on the orientation. Moreover, the magnitude of lateral force is larger than the applied normal force (see Fig. 7.6). The magnitude of the static friction (the value at the initial onset of sliding) depends on the orientation, but subsequent overall lateral forces show little dependence on orientation and temperature. Both the very high friction coefficient and the large amount of wear can be explained by the significant adhesion between the bare silicon surfaces. Even when we apply an upward load to reduce the adhesion, the same phenomena appears, and eventually a necking instability causes the tip to separate from the substrate when the upward load exceeds a critical value (see Fig. 7.7).

The high friction shown in bare silicon contacts arises because the silicon atoms at the interface have interaction energies of the same order of magnitude as the silicon atoms in the bulk so that they resist the shearing force like a bulk solid. The actual AFM experiments that have been performed do not have bare surfaces due to the natural occurrence of native oxide layers [4], and the surfaces of MEMS/NEMS devices are also naturally oxidized.

7.4 Simulations of Oxidized Silicon Surfaces

7.4.1 Silicon Oxidation

Oxidation of silicon surfaces has been widely investigated mainly in connection with the interface properties governing the performance of metal-oxide-semiconductor (MOS) devices [18]. Oxide films have amorphous structures and have been constructed through various methods in order to reproduce realistic Si/SiO_2 interface structures [19-21].

In this study, we used a procedure proposed by Dalla Torre *et. al*. [22]. They inserted oxygen atoms into silicon-silicon bonds, but the film grows not by diffusion of oxygen atoms, but by the continuing insertion of oxygen atoms into the silicon-silicon bonds inside the film. They used the Watanabe potential [14] to oxidize both flat and rounded silicon surfaces. It turned out that with this method we could easily control the defects both at the interface and inside the film. The detailed procedure for the flat surface involves attaching some oxygen atoms onto dangling bonds of the silicon atoms at the top surface. These sites are then used as nuclei for further oxidization. Next silicon atoms with at least one oxygen atom and at most three oxygen atoms are chosen. Atoms with higher vertical position are preferred. Once a silicon atom is chosen, a new oxygen atom is inserted into the longest Si-Si bond. The new position of the inserted oxygen is chosen so as to have the same equilibrium length from both silicon atoms.

However, because only the equilibrium length for the pair interaction is considered, there can be an excessive force exerted by the three body terms resulting in a thermal energy peak after the insertion of each oxygen atom. The kinetic energies of individual atoms are monitored and rescaled when they exceed a critical value. The procedure for the spherical surface is the same as that for flat surface except that insertion points with larger radii from the center are preferred. The simulation results are shown in Fig. 7.8 and Fig. 7.9.

7.4.2 Sliding Simulation: Comparison of bare silicon surfaces and oxidized surfaces

We prepared three different models to determine what role silicon oxide plays on friction as seen in Fig. 7.10; (a) Bare silicon surfaces (# of atoms = 11,645) (b) A bare silicon tip and an oxidized substrate (# of atoms = 14,645) (c) An oxidized tip and an oxidized substrate (# of atoms = 20,518). Before oxidation, the tip radius is 5.2 nm and the substrate size is 9.22 nm × 9.22 nm with 12 silicon layers. The simulation cell has periodic boundary conditions in the [110] and [-110] directions. The bottom layer of the substrate is fixed. The particle interactions are modeled by the WA potential, and the Nose-Hoover chain thermostat is used [23].

Fig. 7.11 shows the adhesion energy of the models, which is defined as the interaction energy between the atoms in the tip and the atoms in the substrate. The reduction of the adhesion energy of the oxidized surfaces can be explained by the existence of repulsive O-O bonds and multiple contacts at the interface.

For the sliding simulations, we examined four different normal forces (8.3, 16.6, 24.9, 33.2 nN), one sliding velocity (27.3 m/sec), and one temperature (250K). During the sliding of the bare silicon model wear was evident as lost particles, but no lost particles were observed during simulations of the oxidized models.

Fig. 7.12 shows the lateral force as a function of tip position. In the bare silicon surfaces apparent stick-slip motion and high friction is observed. With the oxidized surfaces stick-slip is less evident and friction is the lowest among the models. Low friction in the oxidized model arises from the same origins as the absence of adhesion discussed above: the repulsive O-O bonds and atomic scale roughness combine to greatly reduce attractive interactions between the surfaces. Fig. 7.13 shows the relation between the lateral force and the applied normal force. In our simulation regime the lateral force is linearly proportional to the normal force, reminiscent of Amontons law. In our graph, if we extend the linear fitting curve to intersect the vertical axis, i.e. zero applied normal force, we can see that the friction does not converge to zero. The coefficient of friction of oxidized silicon surfaces (~0.15) calculated from the slope is in the range of experimental results [4].

One of the major differences of these simulations from real experiments is the magnitude of the sliding velocity. As seen in Chap. I, while the AFM experiments use sliding velocities of nm/sec to μm/sec, the current simulation velocity is 27.3 m/sec.

7.5 Sliding Simulation with hyperdynamics

7.5.1 Simulation

Simulations of an oxidized tip on an oxidized substrate were next performed using hyperdynamics to achieve slower sliding speeds. Fig. 7.14 shows the simulation system and its dimensions. Both the substrate and the tip have oxide layers grown into the silicon crystalline structure as described above. The substrate consists of the total 9,591 atoms and the tip has the total 5,162 atoms. The tip is joined to the substrate in the [001] direction by applying a normal force of 8.3 nN. The atoms on the bottom layer of the substrate are fixed to prevent a rigid-body translation in the vertical direction, and the system is subject to the periodic boundary condition in the horizontal directions. The relative motion of the atoms on the top layer of the tip is also fixed, but they can move like a rigid body, and they are pulled by a spring of $k = 7.91$ N/m. The atomic interactions are modeled by the Watanabe potential [14], and the Nose-Hoover chain thermostat is used [23].

For the hyperdynamics simulation, we used the bond-boost method discussed in Chap. IV [24]. The bond-boost method detects transitions by monitoring the bond length changes from reference lengths. Each bond has individual bias potentials multiplied by an envelope function which is a function of the maximum bond length change. As the most elongated bond length approach a pre-determined limit, the total bias potential vanishes.

We simulated at temperatures of 100 K and 300 K and at various sliding velocities ranging from m/sec to nm/sec.

7.5.2 Results

From the initial configuration we randomized the initial velocities in order to sample 20 different instantiations and observe the first peak in the stick-slip motion. The lateral force was averaged from the maximum force for each measured transition.

Fig. 7.15 shows the frictional force data at two different temperatures as functions of sliding velocity. The most consistent result of our simulation is that the logarithmic dependence of frictional force on sliding velocity was reproduced in this amorphous silica model as in the 2-D and 3-D L-J commensurate surfaces, as seen in the intermediate velocity range. Plateau regions were observed at high velocity, which can be expected from a modified Tomlinson model with vanishing barrier energy ΔE of the form $\lambda (F_C - F)^{3/2}$ [25]. The values of transition velocity at which frictional force converges to a constant value showed dependence on temperature as well as the magnitude of critical force. The theory expects the transition velocity to depend on both temperature and curvature near critical force, but we would need more data to parameterize the variables in the theory.

Another surprising result of the simulation is a plateau region at lower velocity (300 K), which indicates a deviation from the modified Tomlinson model. Thus, below sliding velocities of 10 μm/sec, the high temperature (300 K) results show that the lateral force is independent of the sliding velocity while at the low temperature (100 K), the lateral force is logarithmically proportional to the sliding velocity. This result is consistent with the experimental result [4].

7.5.3 Discussion

In this section, we discuss the possible physical origins of the above observations. First, Fig. 7.15 shows a difference in critical forces at different temperatures, which may suggest a change in effective potential energy at the interface by temperature. Thus, we can hypothesize that the increase in frictional force at decreasing temperature, observed in recent AFM experiments [4], may be due to variation in potential energy felt by the tip as well as different thermal activation rates by temperature.

Moreover, Evstigneev *et. al.* experimentally reported deviation from the modified Tomlinson model at lower velocities and discussed possible explanations [5]. Our MD simulation results provide an opportunity to confirm their hypotheses and observe the detailed atomic process during the sliding.

In the Tomlinson model, stick-slip behavior is the result of transitions between energetic minima over barriers the heights of which depend on the current driving force. The Tomlinson model assumes unidirectional transitions. However, real systems have multiple transition modes whose barrier heights may change differently as the applied force changes, and transitions through different mechanisms may change the velocity and temperature dependence of the frictional force. Among several possibilities suggested by Evstigneev *et al.* [5], we observed multiple bonds forming at the interface in our model and a bond breaking and reformation before the slip phase. This causes the tip to move backward slightly and in turn increases the lateral force (Fig. 7.16). This bond breaking occurred more frequently at lower sliding velocity because of the longer waiting time, and may explain the plateau at lower sliding velocity. That is to say, the increase of the lateral force due to the bond breaking may compensate for the decrease in the lateral force as velocity decreases. This phenomenon did not happen in the lower temperature simulations. One possibility is that at lower temperatures the potential energy is altered making such transition modes less probable.

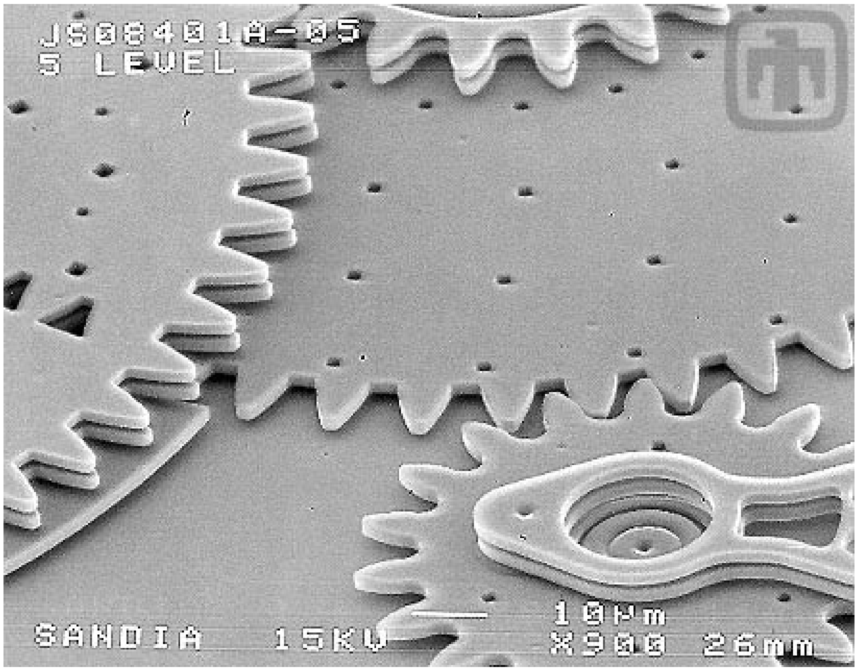

Figure 7.1 Pinion gear used in a micro engine (Courtesy of Sandia National Laboratories, SUMMiTTM Technologies, www.mems.sandia.gov).

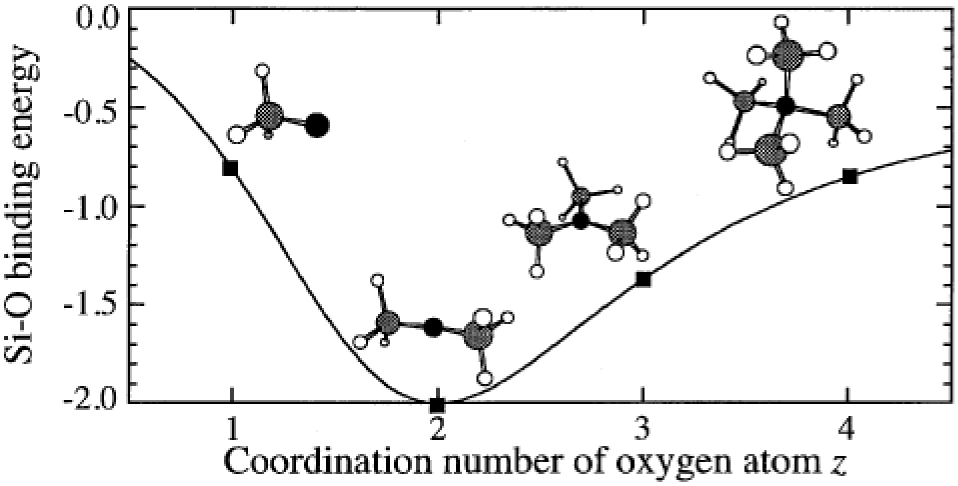

Figure 7.2 Total Si-O bond energies of various clusters with different coordination number (solid curve for –z g(z)) [14].

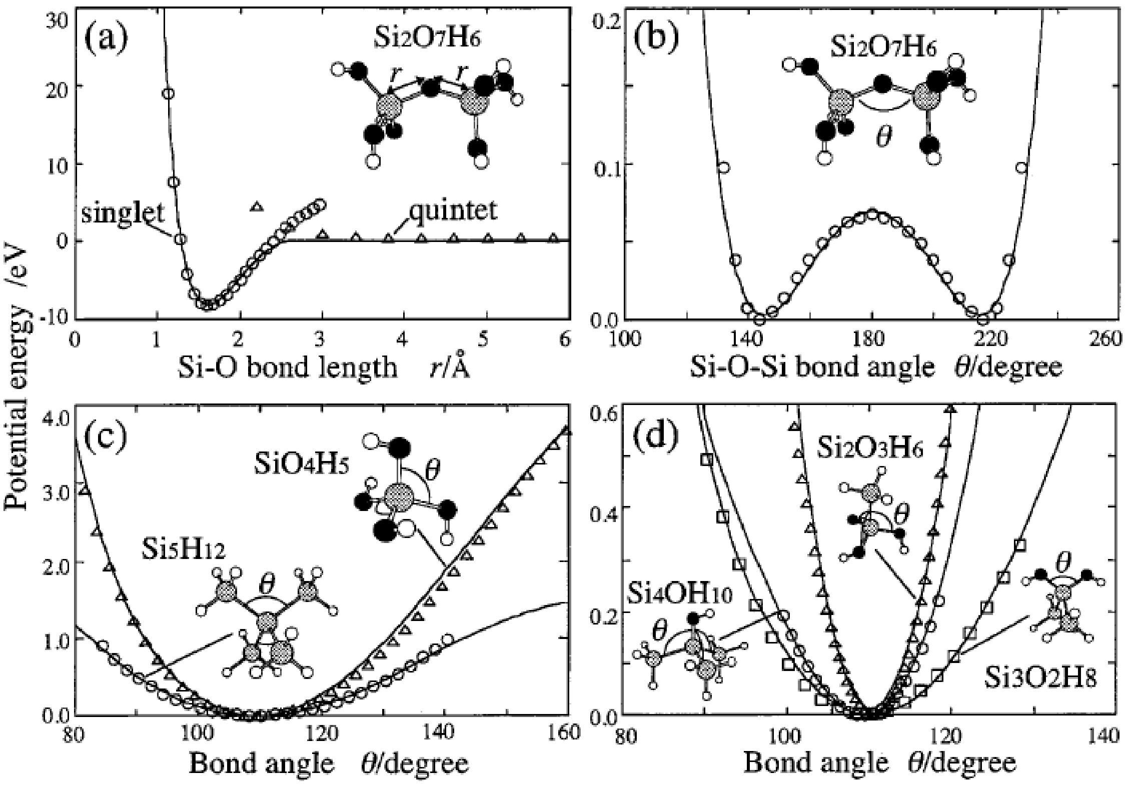

Figure 7.3 Potential energy of various silica clusters calculated from Hartree-Fock molecular orbital theory [14].

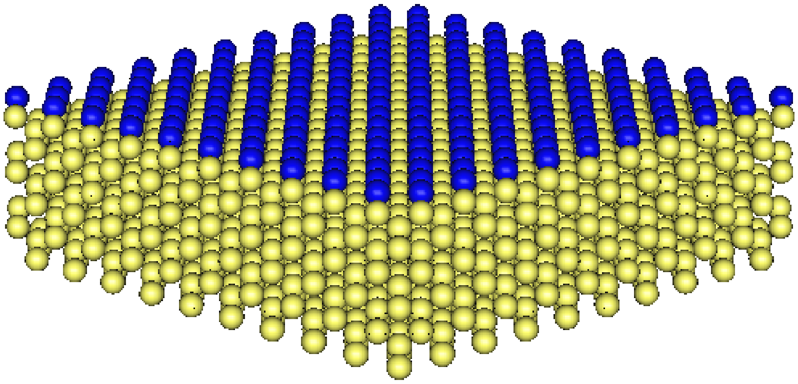

(a) Before the reconstruction

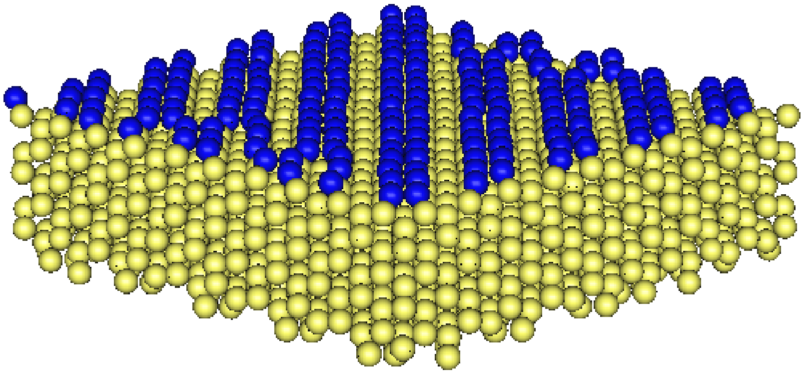

(b) After the reconstruction

Figure 7.4 Surface reconstruction of silicon (001) surface (Temperature = 250 K).

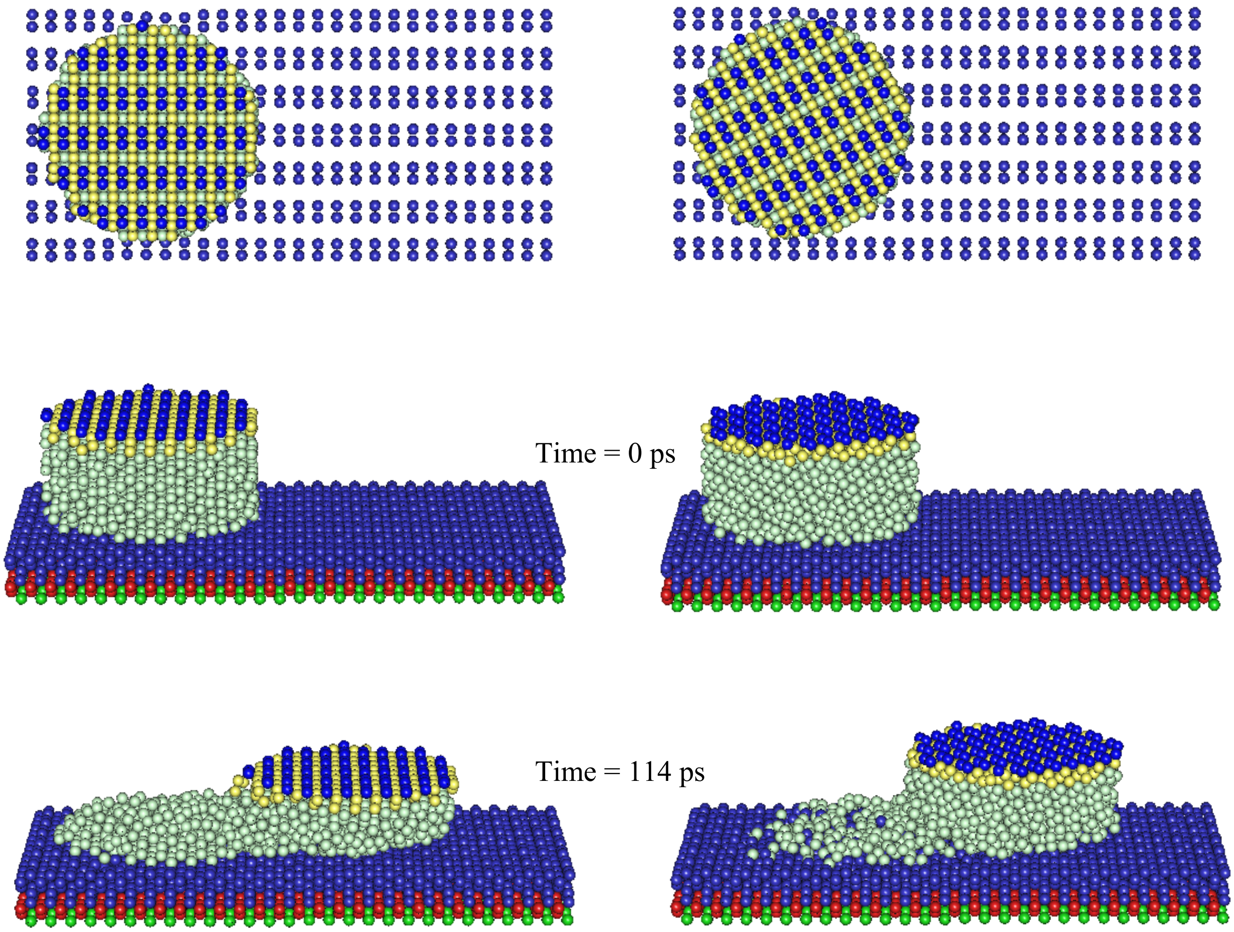

(a) 0^{o} orientation

(b) 30^{o} orientation

Figure 7.5 Friction simulation with variously orientated cylindrical tip. (a) 0^{o} orientation. (b) 30^{o} orientation.

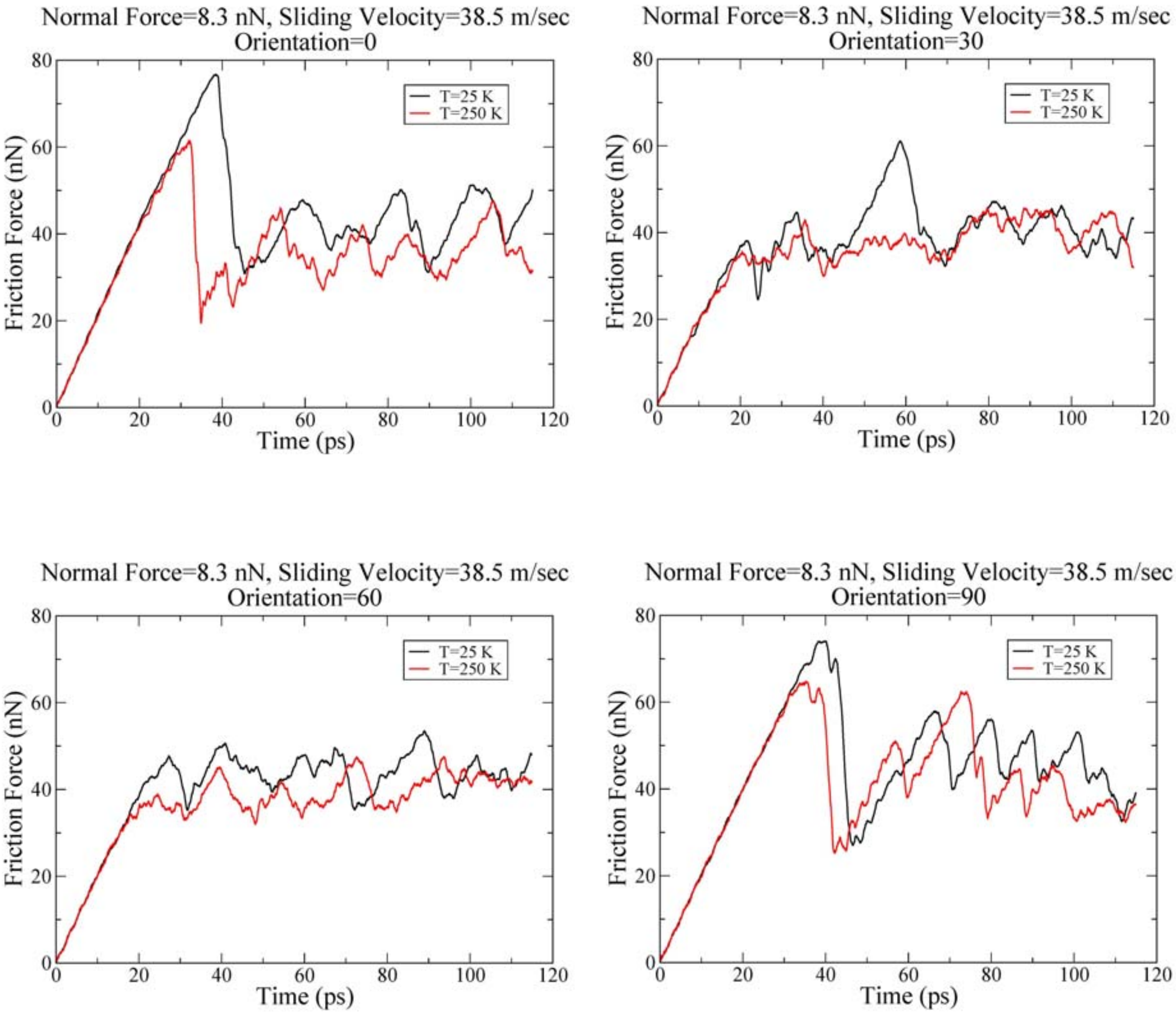

Figure 7.6 Lateral force as a function of time.

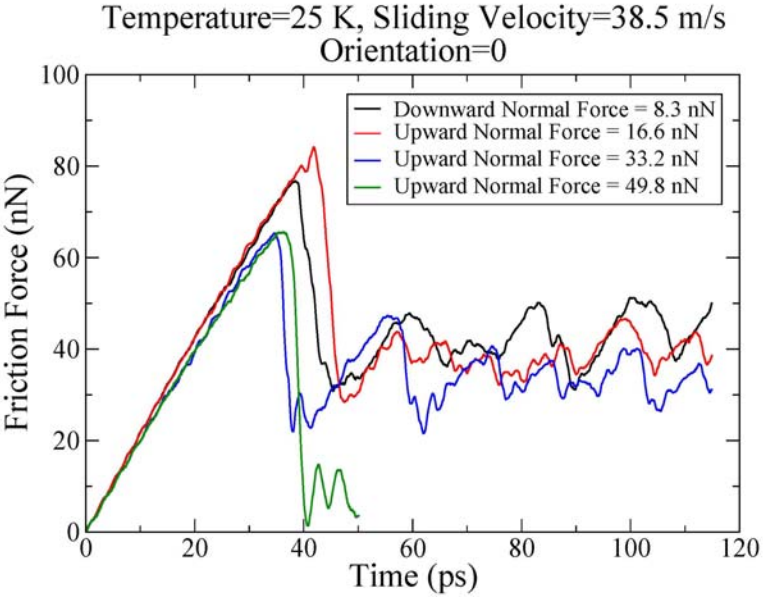

Upward Normal Force = 49.8 nN

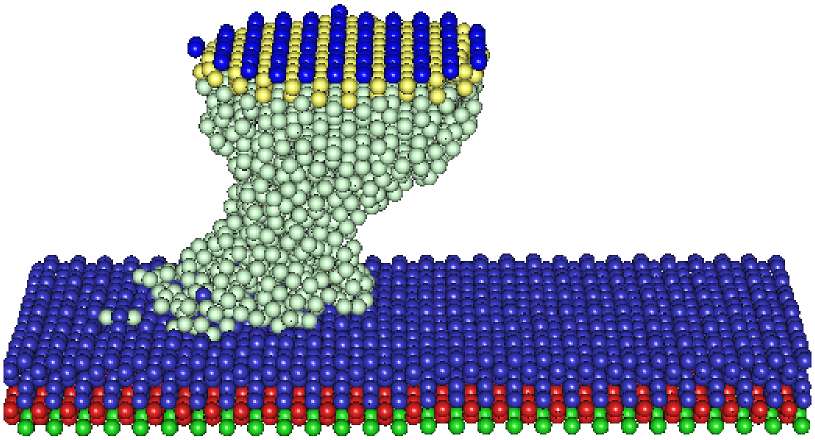

Figure 7.7 Simulation with the normal force applied upward.

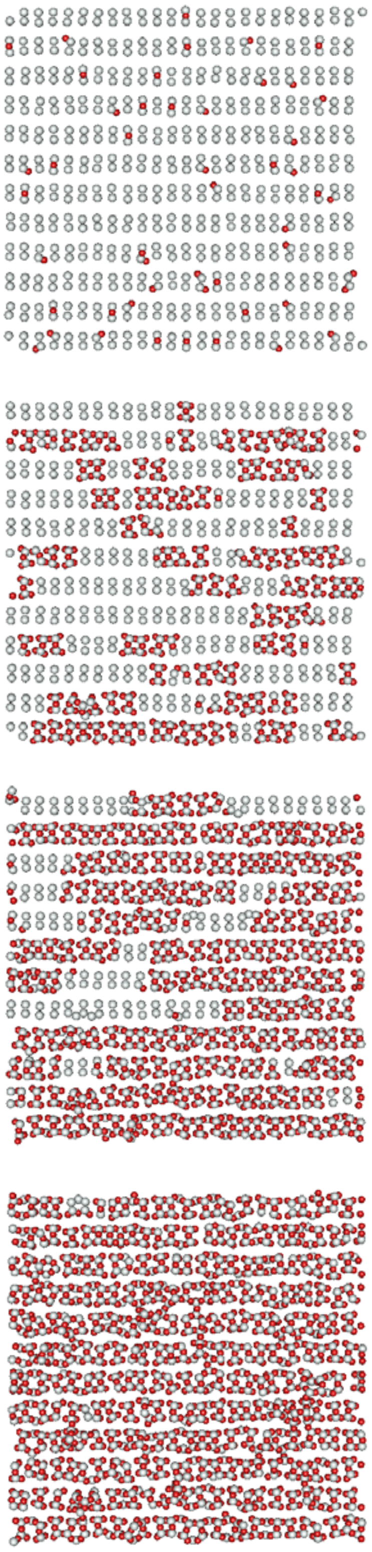

Figure 7.8 Oxidation of flat silicon surface.

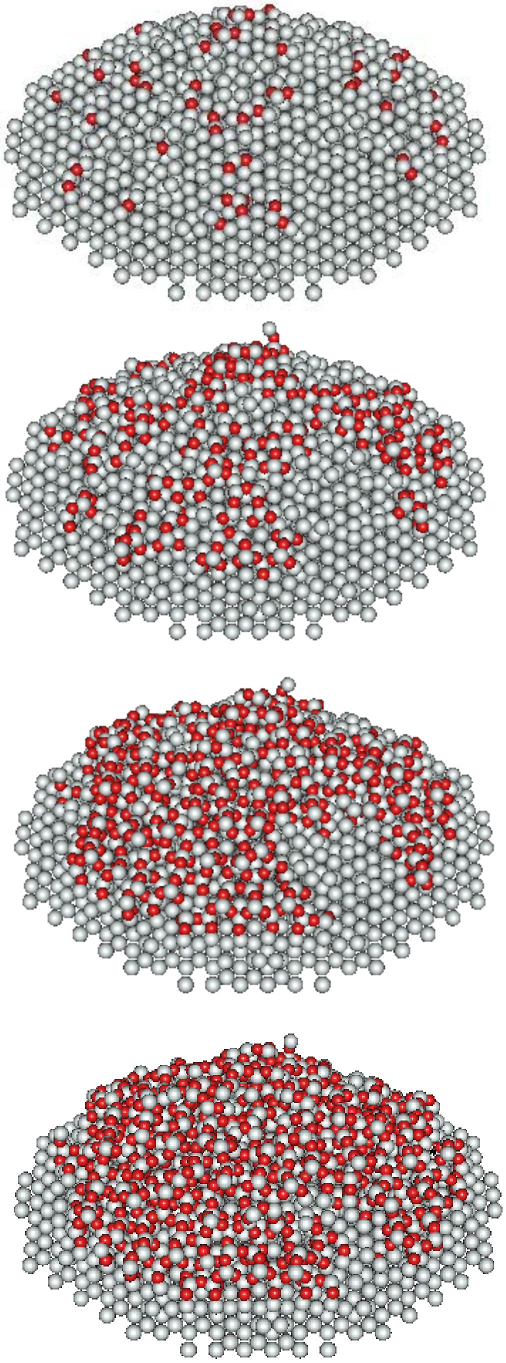

Figure 7.9 Oxidation of spherical silicon surface.

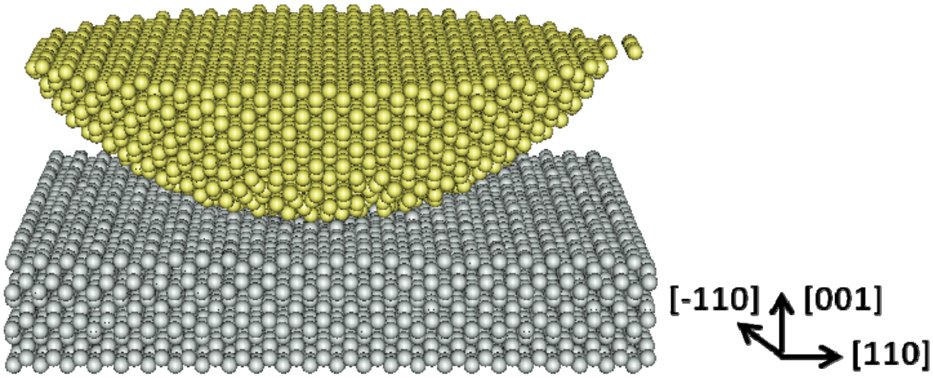

(a) Bare silicon tip and substrate

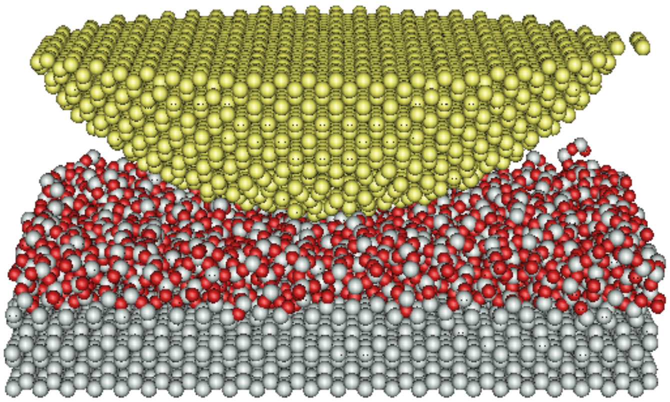

(b) Only substrate oxidized

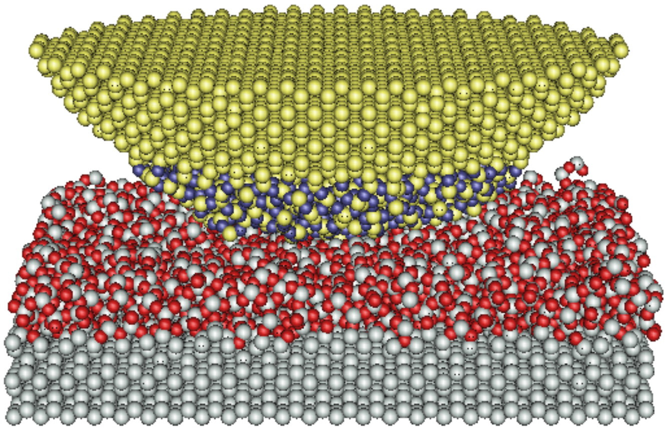

(c) Tip and substrate oxidized

Figure 7.10 Sliding models with round tips. (a) Bare silicon tip and substrate. (b) Only substrate oxidized. (c) Tip and substrate oxidized.

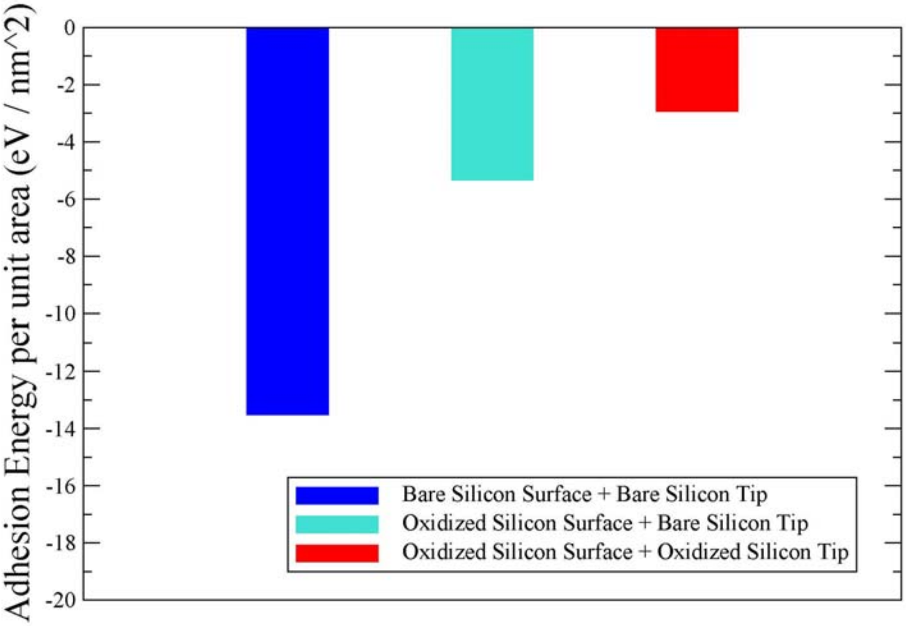

Figure 7.11 Adhesion energy.

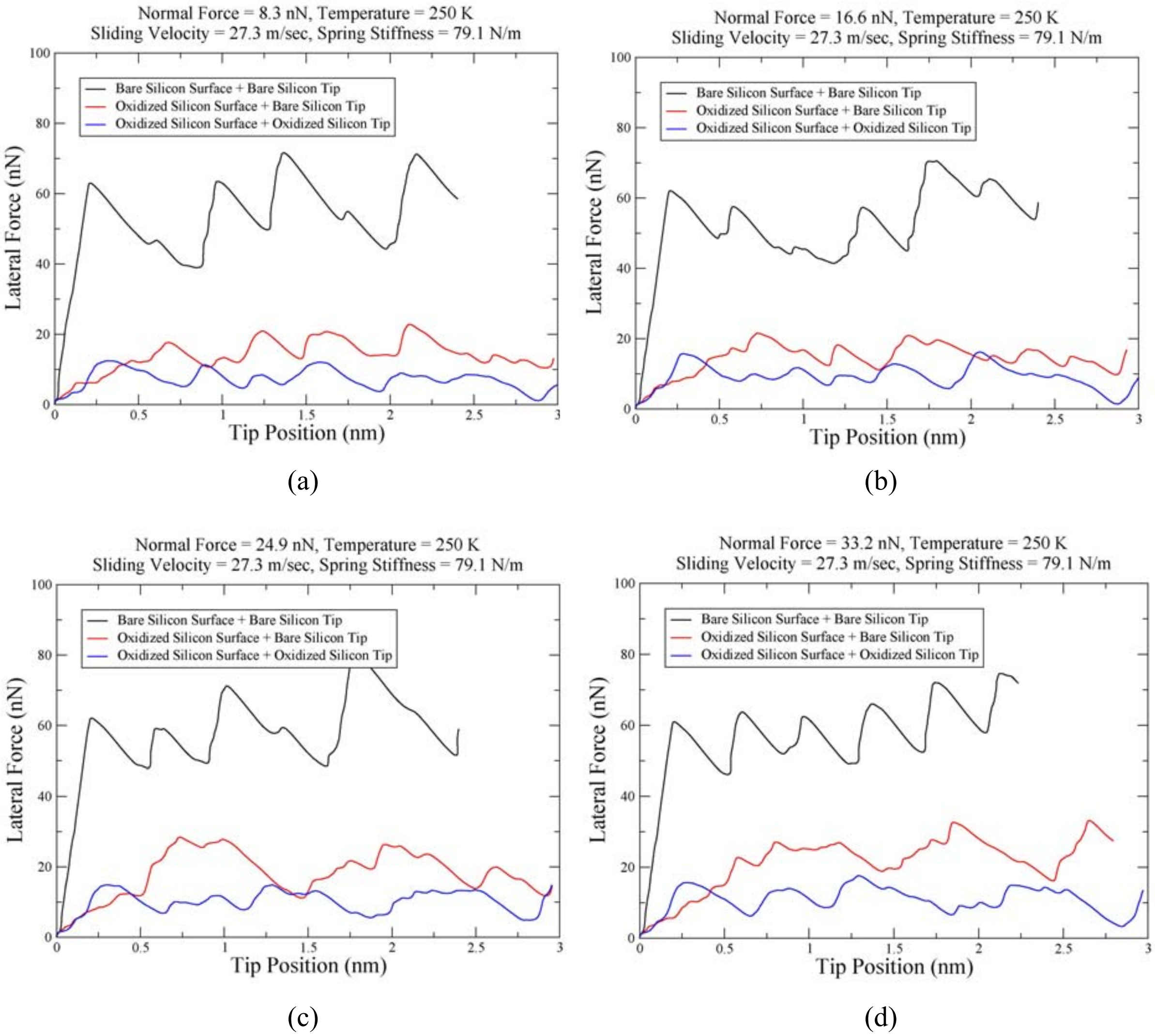

Normal Force = 8.3 nN, Temperature = 250 K
Sliding Velocity = 27.3 m/sec, Spring Stiffness = 79.1 N/m

(a)

Normal Force = 16.6 nN, Temperature = 250 K
Sliding Velocity = 27.3 m/sec, Spring Stiffness = 79.1 N/m

(b)

Normal Force = 24.9 nN, Temperature = 250 K
Sliding Velocity = 27.3 m/sec, Spring Stiffness = 79.1 N/m

(c)

Normal Force = 33.2 nN, Temperature = 250 K
Sliding Velocity = 27.3 m/sec, Spring Stiffness = 79.1 N/m

(d)

Figure 7.12 Lateral forces as functions of tip position at various normal loads.
(a) 8.3 nN. (b) 16.6 nN. (c) 24.9 nN. (d) 33.2 nN.

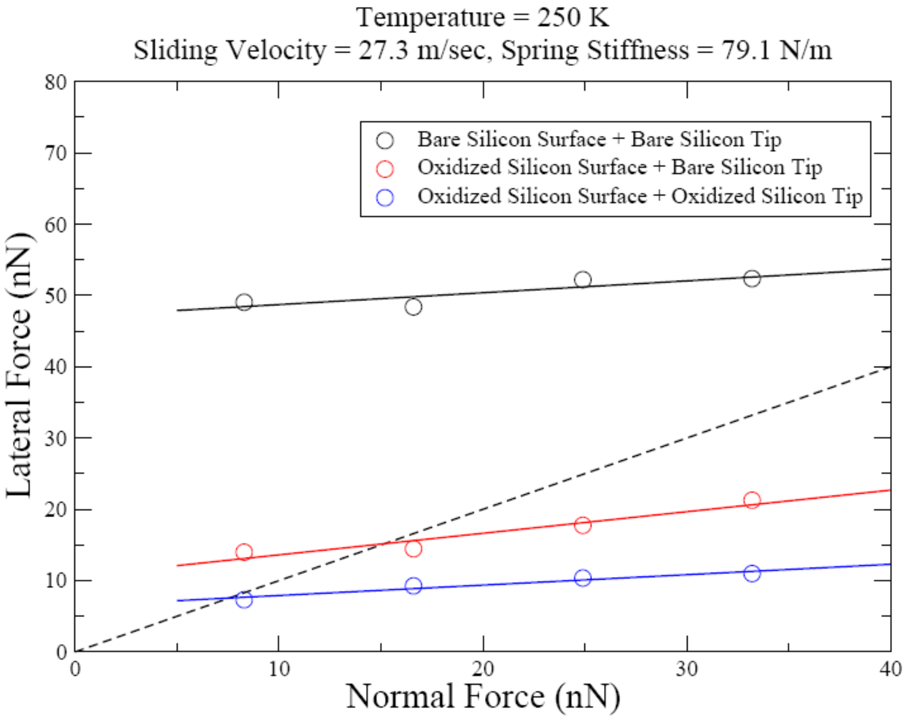

Figure 7.13 Lateral forces as functions of normal loads. Each slope corresponds to the coefficient of friction.

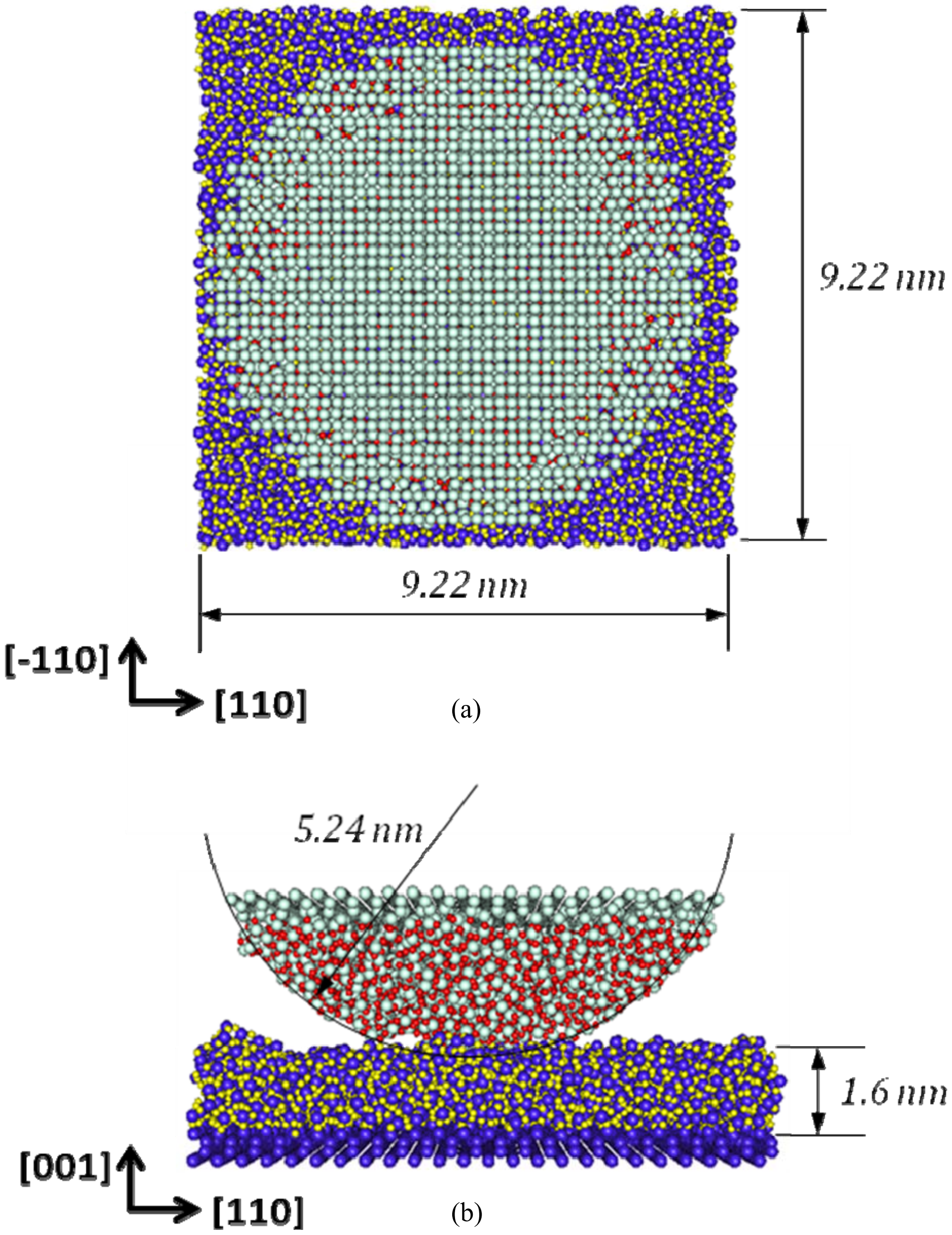

Figure 7.14 Simulation models. Red and yellow atoms are oxygen, and gray and blue atoms are silicon. (a) Top view (b) Front view.

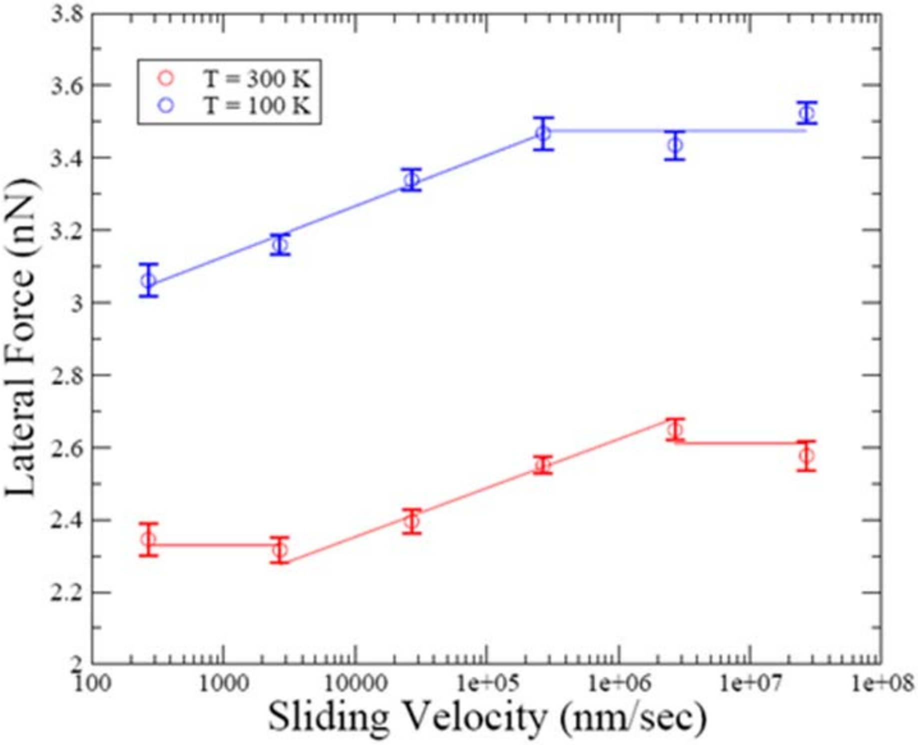

Figure 7.15 Frictional force data as a function of sliding velocity obtained from the simulations with the model shown in Fig.7.14. The error bars show the standard error.

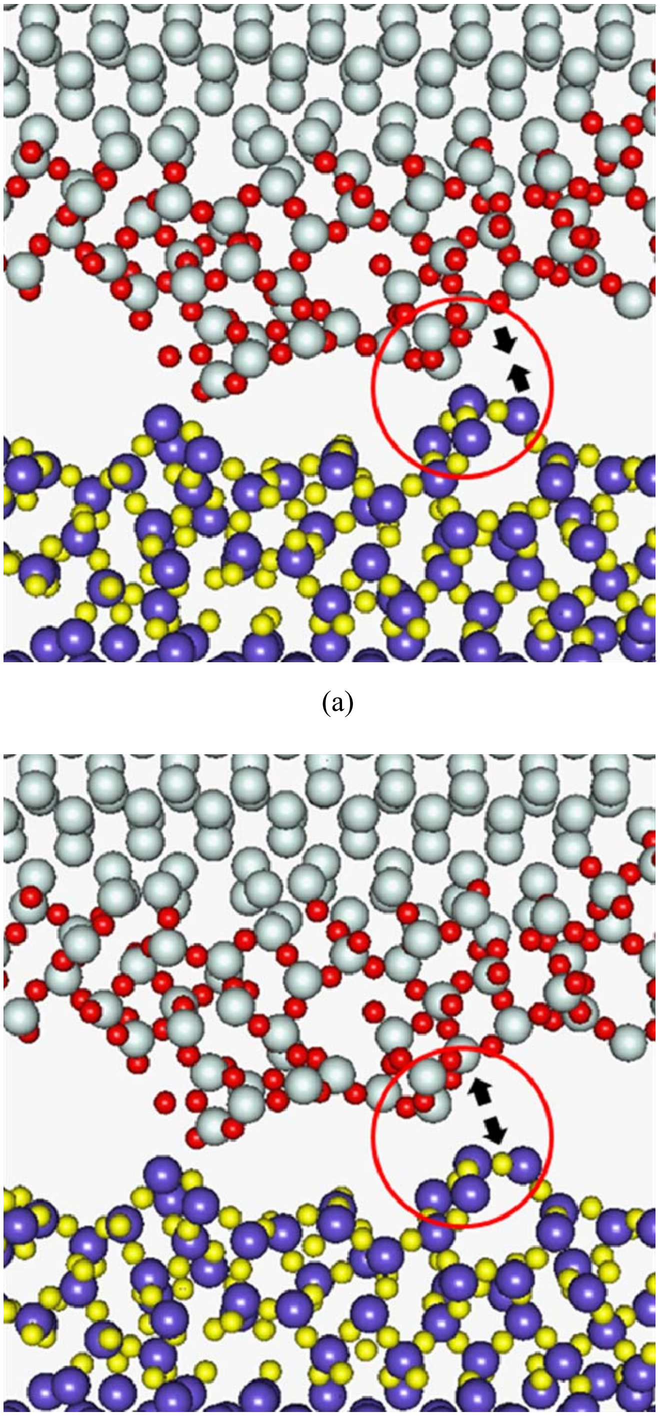

(a)

(b)

Figure 7.16 Closer view at the interface. Two contact regions are seen. Inside the red circle, (a) the bond forms and (b) it breaks.

References

[1] *http://en.wikipedia.org/wiki/Silicon*

[2] M. Mehregany, and C. A. Zorman, “Surface Micromachining: A Brief Introduction”, MRS Bull., 26, 289 (2001).

[3] M. P. de Boer, and T, M. Mayer, “*Tribology of MEMS*”, MRS Bull., 26, 302 (2001).

[4] A. Schirmeisen, L. Jansen, H. Hölscher, and H. Fuchs, “*Temperature Dependence of Point Contact Friction on Silicon*”, Appl. Phys. Lett., 88, 123108 (2006).

[5] M. Evstigneev, A. Schirmeisen, L. Jansen, H. Fuchs, and P. Reimann, “*Force Dependence of Transition Rates in Atomic Friction*”, Phys. Rev. Lett., 97, 240601 (2006).

[6] F. H. Stillinger and T. A. Weber, “*Computer Simulation of Local Order in Condensed Phases of Silicon*”, Phys. Rev. B, 31, 5262 (1985).

[7] J. Tersoff, “*New Empirical Model for the Structural Properties of Silicon*”, Phys. Rev. Lett., 56, 632 (1986).

[8] M. Z. Bazant, E. Kaxiras, and J. F. Justo, “*Environment-Dependent Interatomic Potential for Bulk Silicon*”, Phys. Rev. B, 56, 8542 (1997).

[9] S. Tsuneyuki, M. Tsukada, H. Aoki, and Y. Matsui, “*First-Principles Interatomic Potential of Silica Applied to Molecular Dynamics*”, Phys. Rev. Lett., 61, 869 (1988).

[10] B. W. H. van Beest, G. J. Kramer, and R. A. van Santen, “*Force Fields for Silicas andAluminophates Based on Ab Initio Calculations*”, Phys. Rev. Lett., 64, 1955 (1990).

[11] B. P. Feuston, and S. H. Garofalini, “*Empirical Three-Body Potential for Vitreous Silica*”, J. Chem. Phys., 89, 5818 (1988).

[12] P. Vashishta, R. K. Kalia, J. P. Rino, and I. Ebbsjö, “*Interaction Potential for* SiO_2*: A Molecular-Dynamics Study of Structural Correlations*”, Phys. Rev. B, 41, 12197 (1990).

[13] L. Huang, and J. Kieffer, “*Molecular Dynamics Study of Cristobalite Silica Using a Charge Transfer Three-Body Potential: Phase Transformation and Structural Disorder*”, J. Chem. Phys., 118, 1487 (2003).

[14] T. Watanabe, H. Fujiwara, H. Noguchi, T. Hoshino, and I. Ohdomari, "*Novel Interatomic Potential Energy Function for Si, O Mixed Systems*", Jpn. J. Appl. Phys., 38, L366 (1999).

[15] M. P. Allen and D. J. Tildesley, *Computer Simulation of Liquids* (1987).

[16] J. Lampinen, R. M. Nieminen, and K. Kaski, "*Molecular Dynamics Simulation of the Structure and Melting Transition of the Si(001)*", Surf. Sci., 200, 101 (1988).

[17] P. C. L. Stephenson, M. W. Radny, and P. V. Smith, "*A Modified Stillinger-Weber Potential for Modelling Silicon Surfaces*", Surf. Sci., 366, 177 (1996).

[18] M. Schaible, "*Empirical Molecular Dynamics Modeling of Silicon and Silicon Dioxide: A Review*", Crit. Rev. Solid State., 24, 265 (1999).

[19] A. Pasquarello, M. S. Hybertsen, and R. Car, "*Interface Structure between Silicon and its Oxide by First-Principles Molecular Dynamics*", Nature, 396, 58 (1998).

[20] A. Bongiorno and A. Pasquarello, "*Validity of the Bond-Energy Picture for the Energetics at Si-SiO_2 Interfaces*", Phys. Rev. B, 62, R16326 (2000).

[21] Y. Tu and J. Tersoff, "*Structure and Energetics of the Si-SiO_2 Interface*", Phys. Rev. Lett., 84, 4393 (2000).

[22] J. Dalla Torre, J.-L. Bocquet, Y. Limoge, J.-P. Crocombette, E. Adam, G. Martin, T. Baron, P. Rivallin, and P. Mur, "*Study of Self-Limiting Oxidation of Silicon Nanoclusters by Atomic Simulations*", J. Appl. Phys., 92, 1084 (2002).

[23] G. J. Martyna, M. L. Klein, and M. Tuckerman, "*Nose-Hoover Chains: The Canonical Ensemble via Continuous Dynamics*", J. Chem. Phys., 97, 2635 (1992).

[24] R. A. Miron and K. A. Fichthorn, "*Accelerated Molecular Dynamics with the Bond-Boost Method*", J. Chem. Phys., 119, 6210 (2003).

[25] E. Riedo, E. Gnecco, R. Bennewitz, E. Meyer, and H. Brune, "*Interaction Potential and Hopping Dynamics Governing Sliding Friction*", Phys. Rev. Lett., 91, 084502 (2003).

CHAPTER VIII

Conclusions

In this dissertation we have developed various efficient methods to perform molecular dynamics simulation of a sliding system modeling the AFM experiment on a longer time scale. These methodologies include the parallel method and the hyperdynamics method. Hyperdynamics has been intensively studied and several critical issues including the accurate calculation of the boost factor have been discussed in detail. Furthermore, for efficient hyperdynamics simulations, we constructed bias potentials using local variables such as the slope and the curvature along the direction connecting a position and the minimum, and the distance of a position from the local minimum in configuration space. Moreover, we introduced the stepped sliding to apply the hyperdynamics scheme to a sliding system. These methods have been further improved with the aid of a parallel algorithm.

These methodologies were tested with simple 2-dimensional and 3-dimenstional AFM models in Chap. V by systematically applying the procedures in succession. The validity of the methodologies is well verified with the simulation results of these models. The stepped sliding serves as a reasonable approximation for continuous sliding, and the simulation results using the other methods both the parallel methodology and hyperdynamics showed close agreements with the simulation results of the conventional method. Moreover, both 2-dimensional and 3-dimensional simulations showed that the average of the lateral forces at the transitions have the logarithmic dependence on the sliding velocity. 2-D simulation at three temperature points showed the lateral force linearly decreases as the temperature increases.

Chap. VI detailed the frictional behaviors of incommensurate surfaces. While ultralow friction forces have been observed between incommensurate surfaces in nano scale experiments, an analysis based on the one-dimensional Frenkel-Kontorova-Tomlinson model and a study using MD simulations have pointed out, incommensurate surfaces can show large static friction if the atoms of one surface are weakly bound when compared to the interaction between the surfaces. Moreover, an experimental study observed a transition from the superlubricity regime (zero friction force) to the stick-slip regime (high friction force) by increasing the applied normal load. MD simulations performed with a 3-dimensional system modeling an AFM experiment regarding incommensurate surfaces observed that superlubricity breaks down with softer tips and at higher normal loads. The softer tips experienced the emergence of several metastable states, which makes the frictional behaviors more complicated.

In Chap. VII, the frictional simulation results of amorphous silica surfaces have been presented. Sliding simulations of bare silicon surfaces revealed very high adhesion and static friction. By introducing oxide layers the reduction of frictional force and the transition from the apparent stick-slip regime to the smooth sliding regime have been observed. Moreover, hyperdynamics simulations with an oxidized silicon tip and a substrate using the bond-boost method achieved sliding velocities in the range of real experimental values. An analysis of the effects of temperature and sliding velocity on friction has provided evidence for a systematic deviation from the modified Tomlinson model and the existence of multiple transition mechanisms. Among several possibilities, we observed multiple bonds forming at the interface in our model and a bond breaking and reformation before the slip phase.

Finally, some remarks about new applications of our methodologies and several useful improvements are worth mentioning. In this research, we applied the hyperdynamics methodology and the parallel algorithm to AFM systems. We modeled frictional sliding of silicon surfaces with oxide layers because in most cases real silicon surfaces have native oxides. For more realistic modeling of AFM experiments, there are several additional considerations. Although many AFM experiments have been performed in UHV, there is a chance that molecules, particularly hydrocarbons, adsorb onto surfaces depending on temperature. For this reasons, the temperature dependence on friction force observed in the experiments may not reveal the characteristics of the materials of a tip and a substrate, but the characteristics of the adsorbed molecules. It is also generally known that after scanning a surface, an AFM tip becomes blunt due to wear. New AFM models should address these issues. Furthermore, many efforts have been made to improve triobological properties of MEMS. These include introducing self-assembled monolayers (SAMs) to passivate silicon surfaces [1]. Moreover, a recent experiment showed that exciting the mechanical resonance of the system normal to the contact plane significantly reduces the measured friction force [2]. These novel systems will be interesting new applications of our methods.

Furthermore the methodologies we have developed have the potential applications beyond the sliding system because many interesting MD systems with time-varying external parameters suffer from the same time scaling problem. For example, in nano indentation simulations, simulations of indenters involve indentation rates much faster than found in real experiments. Moreover, there are systems that experience infrequent transitions with time-invariant potential energies such as the diffusion of dopants in silicon. We are optimistic that the new methods developed in this work can be applied to those problems.

Construction of a bias potential for systems with barriers on multiple time scales, as observed in the simulations with incommensurate surfaces, remains one of the largest remaining challenges. This must include a method for distinguishing between significant barriers that separate states during important kinetic processes and the internal transitions within energy basins. Additionally a scheme determining all the parameters of a bias potential on the fly without performing any pre-simulations is desirable, especially for systems with irregular wells this would represent a major breakthrough in accelerated simulation techniques.

References

[1] U. Srinivasan, M. R. Houston, R. T. Howe, and R. Maboudian, "*Alkyltrichlorosilane-based Self-Assembled Monolayer Films for Stiction Reduction in Silicon Micromachines*", J. Microelectromech. Syst., 7, 252 (1998).

[2] A. Socoliuc, E. Gnecco, S, Mainer, O. Pfeiffer, A. Baratoff, R. Bennewitz, and E. Meyer, "*Atomic-Scale Control of Friction by Actuation of Nanometer-Sized Contacts*", Science, 313, 207 (2006).